Technische Universität München
TUM School of Engineering and Design

Development of a Simulation Tool to Investigate the Neutron Oscillation Induced by the Fluid & Structure Vibration in a 3x3 Fuel Assembly Matrix

Zhuoqi Du

Vollständiger Abdruck der von der TUM School of Engineering and Design der Technischen Universität München zur Erlangung eines

Doktors der Ingenieurwissenschaften (Dr.-Ing.)

genehmigten Dissertation.

Vorsitz: Prof. Dr. Rudolf Neu

Prüfende der Dissertation:

1. Prof. Rafael Macián-Juan, Ph.D.
2. Prof. Dr.-Ing. César Queral

Die Dissertation wurde am 11.10.2023 bei der Technischen Universität München eingereicht und durch die TUM School of Engineering and Design am 27.06.2024 angenommen.

Acknowledgment

Much appreciation to

all people in my life

for your support, company on

the brightest day

and

the darkest night.

This project is fully funded by the German Federal Ministry for Economic Affairs and Energy (BWMi) under Project NEOSSIM (Project Nr. 1501514).

Abstract

Neutron noise has been observed in the in-core or ex-core neutron detectors during normal operations. The amplitude of these fluctuations in PWRs typically can range between 2% and 10% of the steady-state signal - depending on the reactor design, on the type of the fuel assemblies, on the core loading pattern and on the burn-up state, etc. In the classical coupling models, the modern 1D thermal-hydraulics code, such as TRACE, ATHLET, SUBCHANFLOW, is coupled with various neutronic solvers to perform both steady-state and transient calculations. However due to the limitation of their solvers, these coupling models lack the capability of handling intra-fuel assembly disturbances, such as asymmetric power distribution, flow distribution, flow mixing, cross-flow, and so on.

In order to have a better insight of the neutron noise, a CFD based 3D thermal-hydraulic solver (ANSYS-CFX) is coupled with a 3D diffusion equation solver (PARCS) to perform both steady-state and transient calculations over a set of models with different scales. The setups of the TH model, the neutronic model as well as the coupling procedure are explained in details. Oscillating inlet boundary conditions (moderator temperature, moderator velocity) are applied in the transient calculations to induce moderator temperature oscillations which results in relative power fraction oscillations in the neutronics calculation. Based on the mesh deformation method, the fuel rod oscillation cases are also investigated to have an overview of the structure vibration induced neutron oscillation.

The investigations on cases with oscillating moderator temperature and oscillating moderator velocity show a very good consistency with other neutron noise analysis. A 180°phase difference can be observed in the neutron signals between the top and the bottom half of the fuel assembly. On the other hand, the moderator temperature seems limited influenced by the fuel rod oscillation to cause noticeable neutron oscillations. The reasons and the limitations are specifically discussed in this dissertation. Taking the advantage of the CFD-neutronic coupled model, the in project NEOSSIM developed model can offer various possibilities to have high fidelity simulations to estimate possible effects which can cause neutron oscillation before any experiment is done and this model can also help to validate new methods for neutron noise simulation.

Contents

List of Figures

List of Tables

List of Acronyms

ADF assembly discontinuity factor

ANM analytic nodal method

APSD auto-power spectral density

BOC beginning of cycle

BOR boron concentration

BU burn-up

CDF corner discontinuity factor

CFD computational fluid dynamics

CMFD coarse mesh finite difference

DCO density of the coolant

DF discontinuity factor

DFR dual fluid reactor

DNBR departure of nucleate boiling ratio

DNS direct numerical simulation

EOC end of cycle

FA fuel assembly

FDM Finite difference method

FFT fast Fourier transformation

FMFD fine mesh finite difference

FSI fluid-structure interaction

FTC fuel temperature coefficient

FVM finite volume method

HFIR high flux isotope reactor

KWU Kraftwerk Union AG

LES large eddy simulation

LFNS low frequency neutron noise

LRZ Leibniz-Rechenzentrum

MMS memory management system

MSR molten salt reactor

MTC moderator temperature coefficient

NEM nodal expansion method

NRC nuclear regulatory commission

ORR Oak Ridge research reactor

PARCS Purdue advanced reactor core simulator

PPF pin power fraction

RANS Reynolds-averaged Navier-Stokes

RHS right hand side

RPF relative power fraction

RPV reactor pressure vessel

S3K SIMULATE 3K

SG steam generator

SPND self powered neutron detector

SST shear stress transport

TFU fuel temperature

TMO moderator temperature

TH thermal hydraulics

TRACE TRAC/RELAP Advanced Computational Engine

TWALL temperature of the cladding surface

UDF user defined fortran

XS cross section

Chapter 1

Introduction

1.1 Neutron Noise: facts and possible reasons

During the normal operation of a nuclear reactor, the neutron flux is continuously monitored in order to obtain the real-time power of some FAs as well as the averaged power of the core quadrants. The electric signal from the detectors, which is converted later on to neutron flux, however shows an oscillating behavior. These neutron flux fluctuations are known as the neutron noise.

The data received from the neutron detectors reflects the neutron flux development in time domain. By analyzing this data one can see the power change during time (see Fig. 1.1) and calculate the amplitude of the power oscillation. This signal is also fed in the reactor protection system in order to prevent any unwanted power spike. The other way to analyze this data is to convert it to the frequency domain involving a fast Fourier transformation (FFT) algorithm (see Fig. 1.1). The outcome of this conversion is the so-called APSD plot which describes the power as a function of frequency. Most of the power is deposited in the low frequency range and the peaks shown in the APSD plot correspond to different characteristics of the nuclear system. For example, the internal structures are under fluctuating pressure

and drag forces which results in the excitement of natural vibration modes of the internal structures and an oscillation of the neutron detector signals. Any mechanical abnormalities or failures of the internal structures due to the flow-induced vibration will result in a shift of the frequency peaks [DK90]. Therefore the APSD plot is of great interest in neutron noise analysis.

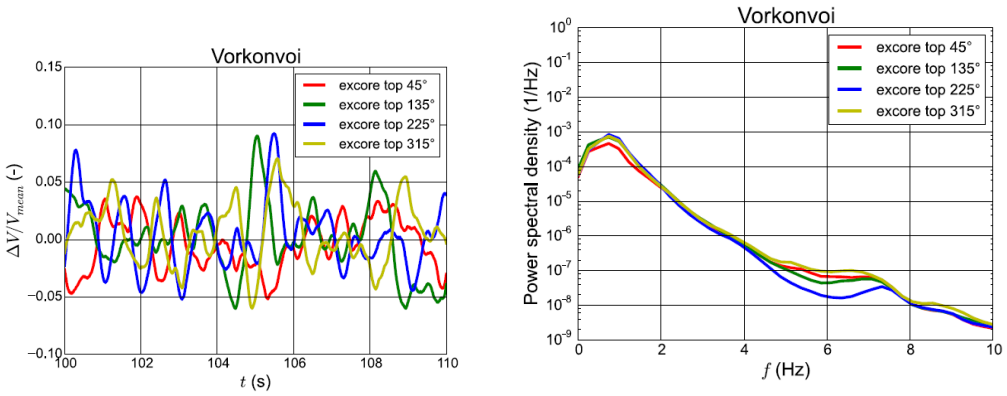

Figure 1.1: Example of neutron detector signal in time domain (left) and in frequency domain (right) [BHK16]

Neutron noise can come up with various reasons. On one hand, nuclear reaction in nuclear reactors has a stochastic behavior. When encountering a target nucleus, neutrons can have reactions like fission, scattering, absorption, etc. The probability of each reaction is strongly related to the microscopic cross sections (σ) of the target nucleus depending on the incident neutron energy as well as the energy level of the target nucleus energy. This phenomenon occurs not only in fission chain reaction but also in neutron detection. This effect is considerably large when dealing with zero power reactor noise [PD10b]. On the other hand, macroscopic cross sections (Σ) can be strongly influenced by geometry changes or by temperature field changes, which results in the change of the power distribution. Besides, the distance between the neutron source and the neutron detector also plays an important role when analyzing the ex-core detector signals. In early literature [SMLS85], by analyzing the neutron noise signal of Sequoyah-1 reactor several causes associated with the frequency range have already been pointed

out (shown in Tab. 1.1). In year 1948 research [WS48] was conducted to

Frequency range (Hz)	Possible noise sources	Type of motion
0.01-1	Fuel motion, temperature noise, feedback effects	Unknown
1-2	Unknown	Pendular
2-5	Fuel assembly vibration first mode	Pendular
5-10	Core support barrel motion beam mode and second mode of fuel assembly	Pendular
10-13	Thermal shield	Shell
13-18	Pressure vessel	Pendular
18-22	Pressure vessel	Shell
22-28	Unknown	In-phase
28-35	Unknown	Pendular
35-40	Core support barrel shell mode	Shell

Table 1.1: Frequency ranges studied at Sequoyah-1 and possible noise sources [SMLS85].

investigate how the neutron flux reacted with a periodic oscillating neutron absorber in a chain-reacting pile. Research [Rob67] studied the reactivity fluctuation induced by changing inlet boundary conditions and the vibration of the rods in small research reactors (the Oak Ridge research reactor (ORR) and the high flux isotope reactor (HFIR)) using a one-group diffusion equation and point kinetic model. Given a relatively small reactor core and low power the results from this research led to the conclusion that the main driving functions are the vibrations of the control rods and fuel elements induced by fluctuations in the coolant velocity. Then researches focused on theoretical investigation of the local and local components of the neutron-noise field in a larger system ([BKK77, PT80]) with a one-/two-dimensional model. Methods were developed to determine and monitor the moderator temperature coefficient (MTC) based on the noise analysis [THW91, LR99, DPA$^+$03]. The space dependence of the neutron noise was investigated showing different behaviors of the point kinetic component and the space dependent component induced by propagating perturbations [PD10a]. In the more

recent researches, dedicated numerical investigations were carried out in order to simulate the neutron noise with a stochastic perturbation model ([BHK16, CDB+17, BMO17, RSKB18, AP18, TCM+19]).

1.2 A quick summary of neutron noise in German nuclear reactors

German PWRs were designed and built by Kraftwerk Union AG (KWU) in two product lines: Vor-Konvoi and Konvoi. Both of them are similar in lots of aspects: 4-loop primary coolant cycle, active zone with a height of 390cm, a total number of 193 FAs and a similar average power density [SKSB15]. The main differences between these two designs are: in the Vor-Konvoi design the FA has a 16x16 layout whereas in the Konvoi design a 18x18 layout, pre-heater in the steam generator (SG) in the Vor-Konvoi design and in the Konvoi design there is a perforated cylinder in the lower plenum while in the Vor-Konvoi design a simple hexagonal support structure (shown in Fig. 1.2).

The measurement system is furtherly divided into two parts: 6 axial self powered neutron detectors (SPNDs) located in each of 8 radial positions inside the reactor pressure vessel (RPV), 2 axial ionization chambers located in each of 4 radial positions in the biological shield of the reactor [SKSB15]. The in-core detectors measure the thermal neutron flux coming directly from the neighboring fuel pins since the diffusion length is about several centimeters. The ex-core detectors on the other hand measure the fast neutron flux from the periphery FAs since the thermal neutrons are mostly either absorbed or scattered by the reflector. Besides, the in-core detectors measure the localized power of some FAs while the ex-core detectors indicate the power of each reactor quadrants.

An example of APSD of an ex-core neutron detector is shown in Fig. 1.3. It is observed that the APSD is continuous in frequency domain with some distinct peaks which can be explained by the flow-induced vibration of the

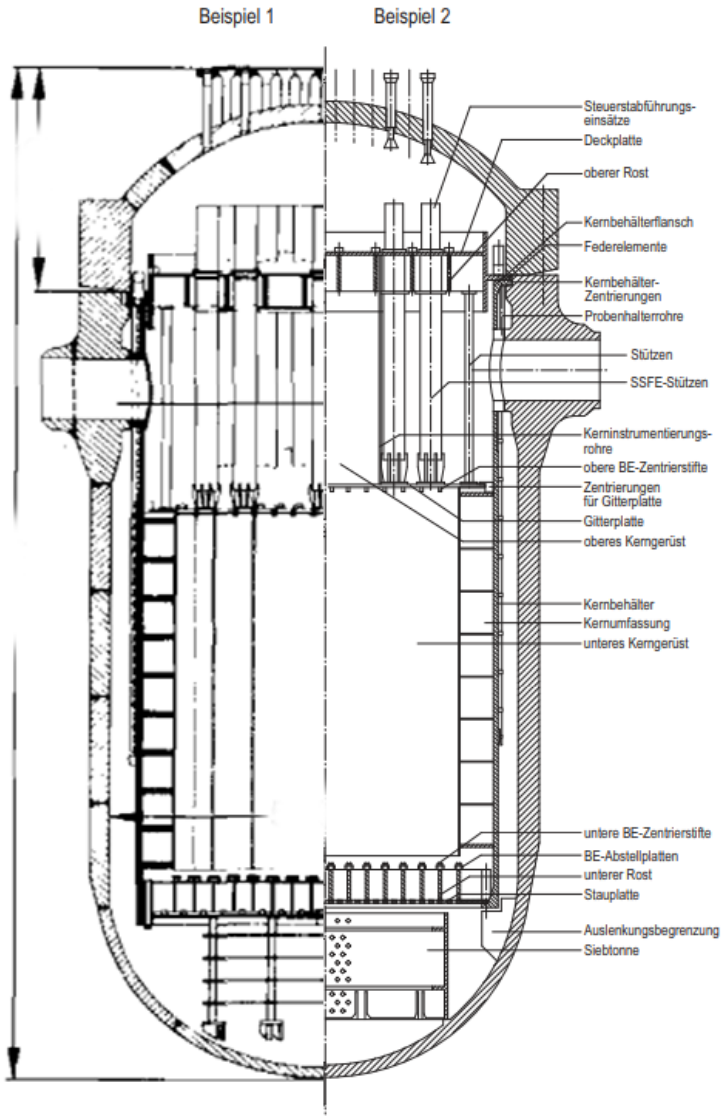

Figure 1.2: Reactor pressure vessel in Vor-Konvoi design (left) [GRS90] and Konvoi design (right) [KTA17]

internal structures(core barrel, different eigenmodes of FA, etc.). Besides, a rapid decrease is also observed in the range of 0.5 to 10 Hz which is known as the low frequency neutron noise (LFNS) and LFNS contributes about 95% of the energy [SKSB15]. It is also pointed out that APSD follows a $1/\omega^2$ behavior (with ω being the perturbation frequency) and Studsvik's SIMULATE 3K (S3K) calculation also shows a good agreement with this

behavior [SKSB15].

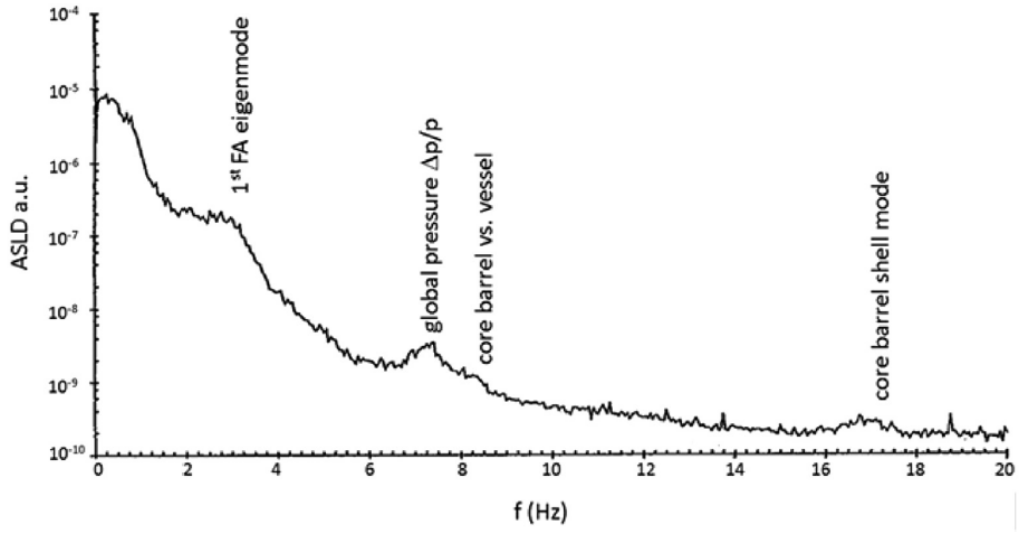

Figure 1.3: Example of the APSD (ASLD in German) of a neutron detector with indication of oscillation modes [SKSB15].

In Fig. 1.4 and 1.5 the coherence and the phase angle of the ex-core detectors are evaluated both for the Vor-Konvoi design and the Konvoi design. In the Vor-Konvoi data, the coherence of two neighboring detectors as well as two opposite located detectors reaches maximum at 1 Hz. The phase angle is almost 0° for two neighboring detectors and 180° for two opposite located detectors. However in the Konvoi data, both the coherence and the phase angle behave differently as in the Vor-Konvoi data. The coherence is small in the range of 0-5 Hz for both neighboring detectors as well as the opposite detector. The phase angle on the other hand, oscillates between -45° and 270°.

Another characteristics of the neutron noise is that the amplitude of neutron noise at BOC is smaller than that at EOC. This phenomenon indicates that the amplitude of neutron noise increases when the average burn-up (BU) of the core increases within the same cycle. Fig. 1.6 shows a brief history of the neutron noise amplitude in a Vor-Konvoi design reactor. It must be mentioned that the neutron noise amplitude doesn't have a direct

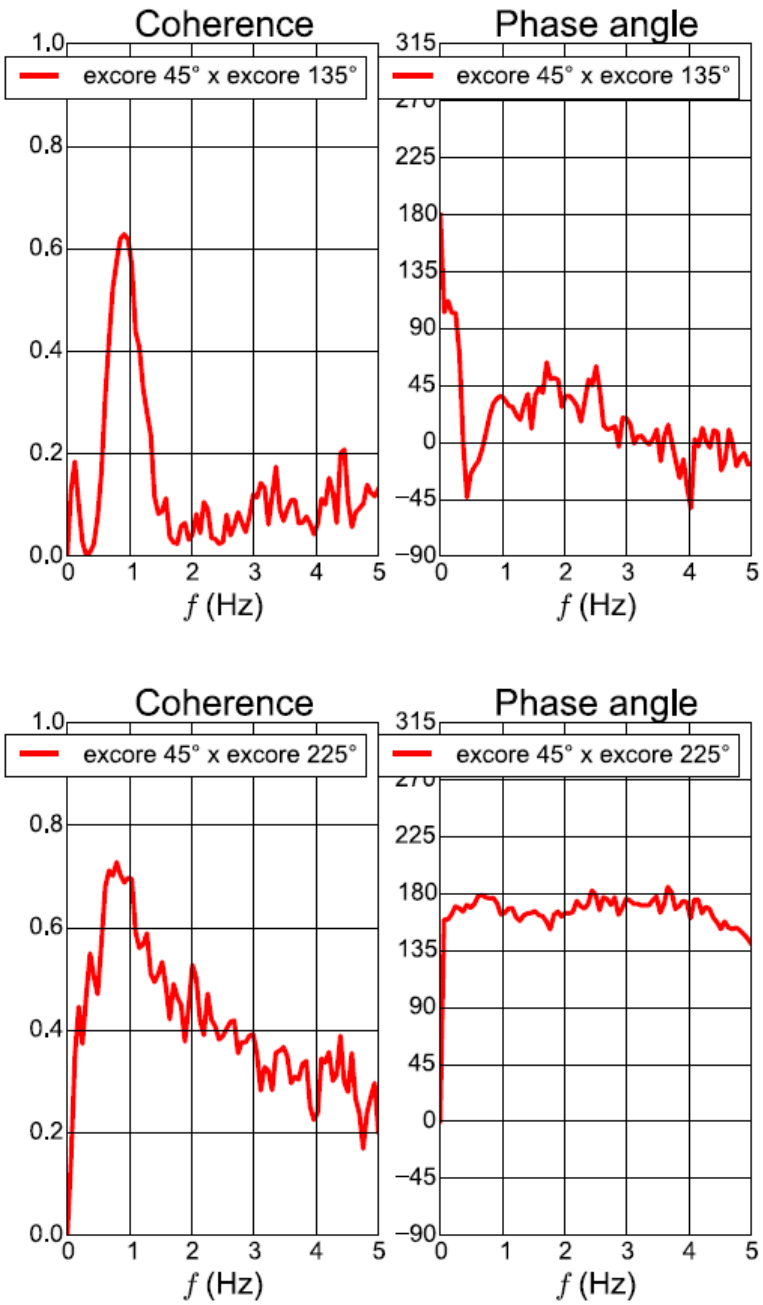

Figure 1.4: Example of the coherence and phase angle of two neighboring ex-core detectors (top) and of two opposite ex-core detectors (bottom) in a Vor-Konvoi reactor [BHK16].

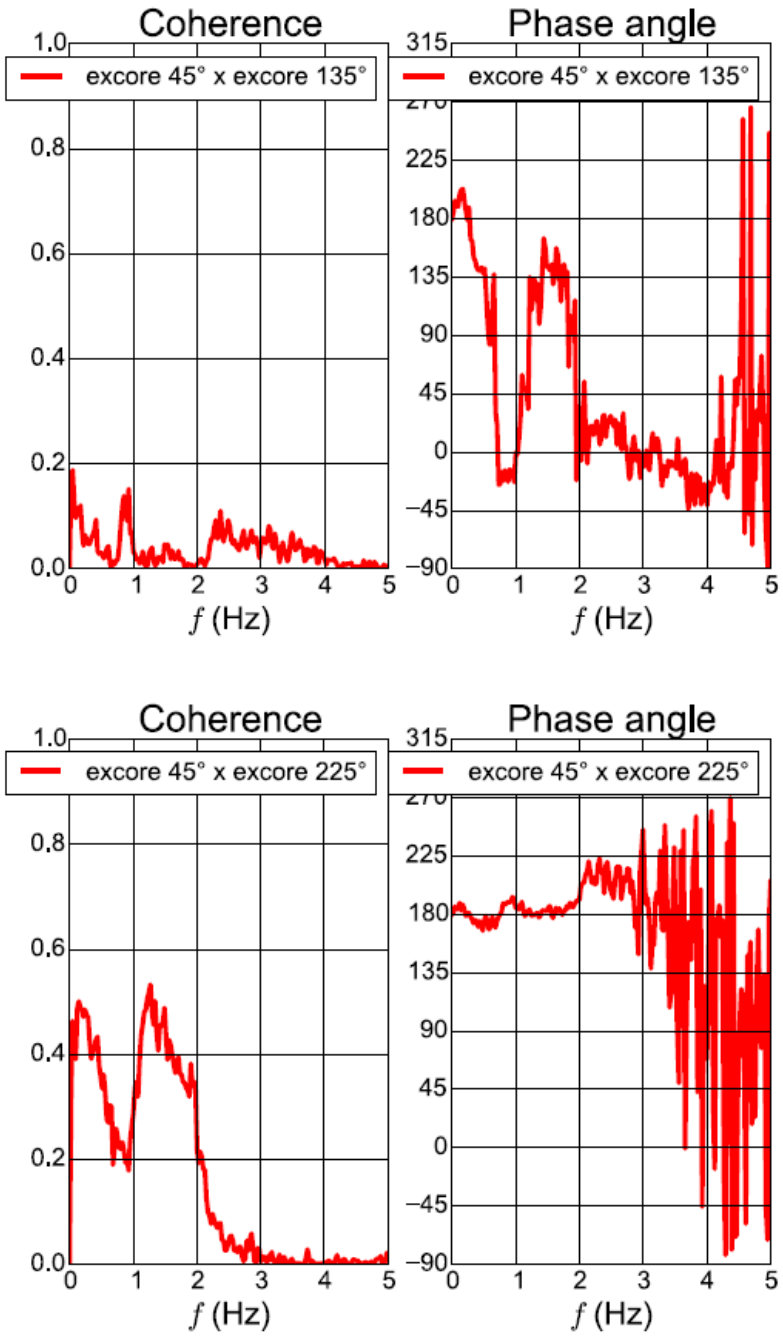

Figure 1.5: Example of the coherence and phase angle of two neighboring ex-core detectors (top) and of two opposite ex-core detectors (bottom) in a Konvoi reactor [BHK16].

relationship with the average BU of the core when comparing two different cycles. Besides, it is also noticed in Fig. 1.6 that the neutron noise behavior changes unexpected from cycle N-10 (unexpected increase and decrease of the neutron noise amplitude) and literature [SKSB15] has summarized several possible causes:

- the change in MTC due to a change in fuel enrichment,
- the change in reactor power due to power updates,
- the use of MOX fuel, and
- the loading pattern.

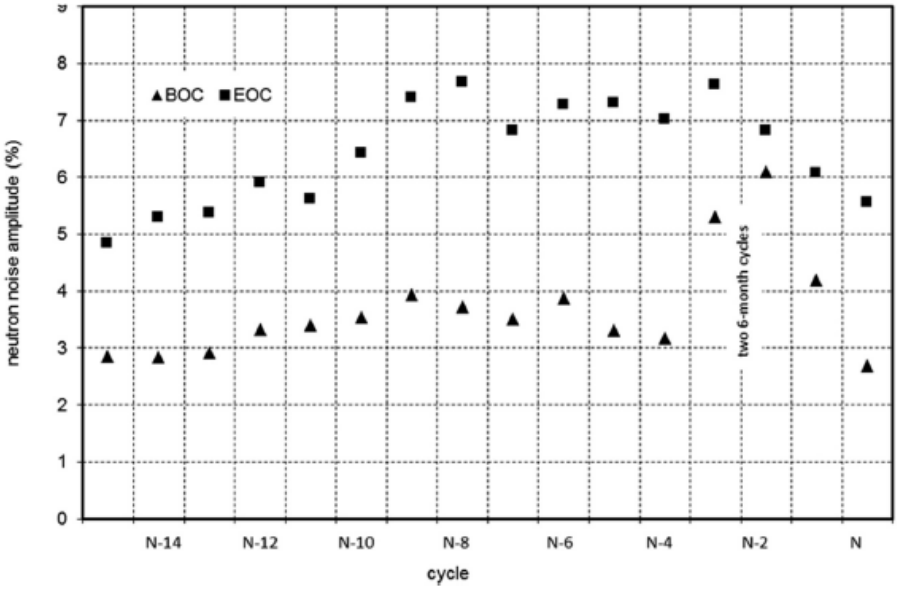

Figure 1.6: History of the neutron noise amplitude at BOC and EOC of a Vor-Konvoi reactor [SKSB15].

1.3 Motivation and objectives of this work

In the classical thermal hydraulics (TH) and neutronics coupled simulations [XDW+09, Glü07, TEIJ11, MMNM+11, LAC+16, HBD+17, RSKB18], the TH part is mostly simulated by solving 1-D two-fluid equations. With these

tools the moderator is assumed to flow straight up through axial core channels without mixing with neighboring fuel assembly channels. This rigid upward-flow model has to be distinguished from models in which the moderator can flow between subchannels inside a fuel assembly. The latter type of simulation is important to correctly describe the steady-state subchannel temperature rise and the associated departure of nucleate boiling ratio (DNBR). Another issue with these tools is lack of capability of simulating cases with changing flow areas (as in fuel assembly bow cases) and not to mention the fluid-structure interaction (FSI) simulations.

In order to have a better insight of the neutron noise a fluid dynamic and neutronics coupled code needs to be built to perform multi-physics calculations at the level of the fuel rods inside a fuel assembly. For this purpose a computational fluid dynamics (CFD) code is chosen since it can both simulate the flow area changes and can be connected to other structure codes to conduct FSI calculations. Although CFD calculations can deliver a more precise and more detailed results compared to normal 1D TH code, more computational resources are needed for CFD calculations. A full core CFD calculation still seems not possible without millions of computation hours and it would require the full computation resources of a supercomputer (like in Leibniz-Rechenzentrum (LRZ)) at a research facility.

Therefore the objective of this work is to establish a reliable coupling regime between a 3-D CFD model and a 3-D neutronics solver for a 3x3 FA matrix. The neutronic power feedback has been studied on a fuel assembly level by applying different boundary conditions: inlet temperature, inlet velocity, fuel assembly bow.

1.4 Softwares involved in this work

1.4.1 A brief overview of the CFD theory

CFD is widely used in simulating fluid flow (single & two phase flow) problems involving fluid-solid interaction, heat transfer, combustion, and so on. Most of the CFD tools (including CFX) apply the finite volume method (FVM) as the solution methods, in which the region is divided into small control volumes and all the parameters inside this control volume (pressure, temperature, velocity, density, viscosity and so on) are put into the discretization process to solve the Navier-Stoke equation. The governing equations in CFD calculations are:

- conservation of mass: continuity equation,
- conservation of momentum: momentum equation of Newton's second law, and
- conservation of energy: first law of thermodynamics or energy equation.

The continuity equation is written as follows:

$$\frac{D\rho}{Dt} + \rho\frac{\partial U_i}{\partial x_i} = 0 \tag{1.1}$$

If the fluid is an incompressible flow which means the density is not influenced by pressure, then Eq. 1.1 is further simplified as:

$$\frac{\partial U_i}{\partial x_i} = 0 \tag{1.2}$$

The momentum equation:

$$\overbrace{\rho\frac{\partial U_j}{\partial t}}^{I} + \overbrace{\rho U_i\frac{\partial U_j}{\partial x_i}}^{II} = -\overbrace{\frac{\partial P}{\partial x_j}}^{III} - \overbrace{\frac{\partial \tau_{ij}}{\partial x_i}}^{IV} + \overbrace{\rho g_j}^{V} \tag{1.3}$$

where term I is the local change with time, II is the momentum convection term, III is the surface force term, term IV describes the molecular-dependent momentum exchange with τ being the stress tensor and term V is the gravitational term. For an incompressible flow Eq. 1.3 can be simplified as:

$$\rho\frac{\partial U_j}{\partial t} + \rho U_i\frac{\partial U_j}{\partial x_i} = -\frac{\partial P}{\partial x_j} - \mu\frac{\partial^2 U_j}{\partial x_i^2} + \rho g_j \tag{1.4}$$

And the total energy equation is written as follows [ANS19]:

$$\overbrace{\rho c_\mu \frac{\partial T}{\partial t}}^{I} + \overbrace{\rho c_\mu U_i \frac{\partial T}{\partial x_i}}^{II} = -\overbrace{P\frac{\partial U_i}{\partial x_i}}^{III} + \overbrace{\lambda\frac{\partial^2 T}{\partial x_i^2}}^{IV} - \overbrace{\tau_{ij}\frac{\partial U_j}{\partial x_i}}^{V} \tag{1.5}$$

in which term I is the local energy change with time, term II is the convection term, term III is the pressure work, term IV describes the heat flux and term V contains the information of the irreversible transfer of mechanical energy into heat.

Depending on the treatment of the turbulence, the common computational models are the Reynolds-averaged Navier-Stokes (RANS), the direct numerical simulation (DNS), the large eddy simulation (LES) and so on. The RANS equations are solved while introducing a set of new stresses (Reynolds stresses) which requires a turbulence model such as k-ϵ model or k-ω model to close the system. The drawback of using RANS is that it can only simulate steady vortex since the solution is time-averaged and simulations including vortex of different sizes and scales should be solved with the LES or the DNS model. But the computational cost is much higher and larger volumes of data are generated for the LES and DNS models. Based on the computational power and the model used in this work, the RANS simulation method is chosen.

The turbulence models used in CFD calculations are normally k-ϵ, the k-ω family and the k-ω based shear stress transport (SST) models. k denotes

kinetic energy, ϵ is the rate of dissipation of turbulence kinetic energy and ω is the the specific frequency of dissipation of kinetic energy. The k-ϵ model has advantages of robustness and low memory requirements. It can predict very well for the high Reynolds numbers while lacking accuracy facing large pressure gradient and strong streamline curvature. The k-ω model is more favorable for wall-bounded boundary layer or low Reynolds number flows. The drawbacks of k-ω model is that it requires a higher mesh resolution near the wall and is not as robust as the k-ϵ model. The k-ω based SST model is a combination of both above mentioned models and is suitable for both handling wall boundary problems (low Reynolds number flow) and high Reynolds number flow (same as the k-ϵ model).

In case of dealing with the wall boundaries the near-wall modeling theory should be mentioned. The near wall region can be divided into different sub-layers, the laminar sub-layer, the buffer layer and the logarithmic layer (shown in Fig. 1.7). In the laminar layer,which is the closest sub-layer to the no-slip wall, the viscosity of the flow has the dominant effect on momentum and heat transfer. The flow in this region is almost laminar-like. In the logarithmic layer, which lies further away from the wall, the turbulence takes the dominant role in the mixing process. In between locates the so-called buffer layer in which the viscosity and turbulence play an equal role in the flow. The thickness of these sub-layers depends on the material property and flow velocity. A dimensionless parameter y^+ is introduced to interpret the ratio between turbulent and laminar influences in a cell. The definition of y^+ is as follows:

$$y^+ = \frac{yu_\tau}{\nu} \tag{1.6}$$

$$u_\tau = \sqrt{\frac{\tau_w}{\rho}} \tag{1.7}$$

$$\tau_w = \rho\nu(\frac{d < U >}{dy})\Big|_{y=0} \tag{1.8}$$

where u_τ is the friction velocity, y is the absolute distance from the wall, ν is the kinematic viscosity, τ_w is the wall shear stress and ρ is the density of the fluid.

In the k-ω simulation the mesh cells closest to the wall should be within the range of viscous sub-layer to obtain an accurate result. The typical y^+ values (shown in Fig. 1.7) for each layers are: the viscous sub-layer ($y^+ < 5$), the buffer layer ($5 < y^+ < 30$) and the logarithmic area ($y^+ > 30$). In general, one should reduce the y^+ value down to around 1 to obtain a better result which will increase the mesh rapidly. One also has to consider keeping the aspect ratio (the ratio of the length of longest side to the shortest side in one cell) low so that the round off error has a reasonable value, which results in a further increment of the mesh cell number. On the other hand, one can also use k-ϵ model with $y^+ > 30$ and apply the wall function to predict the flow behavior for the region with $y^+ < 30$. ANSYS CFX offers scalable wall functions together with the $k-\epsilon$ model which shows a good agreement with the $k-\omega$ model if the simulation doesn't include any layer separation. Result is shown in section 2.2.

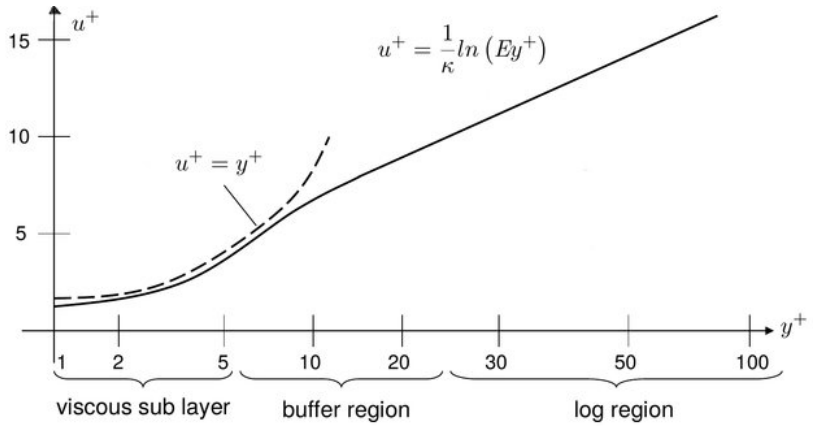

Figure 1.7: Velocity profile and sub-layers in the near wall modeling [Ber16].

As mentioned before, ANSYS CFX is chosen for conducting the TH part of calculation in this work based on its wide applicability, large extensibility and solver robustness.

1.4.2 One dimensional TH code TRACE

The TH code, TRAC/RELAP Advanced Computational Engine (TRACE) which is developed by the U. S. nuclear regulatory commission (NRC), is widely used in system safety analysis, such as large/small break LOCAs and system transients in light water reactors [XDW+09, HBD+17]. By adding new material component and point kinetics model, TRACE is also able to simulate limited transient scenarios of the molten salt reactor (MSR) and the dual fluid reactor (DFR) designs [He16]. Finite difference method (FDM) is applied in TRACE to solve the partial differential equations for heat transfer and two phase flow. TRACE uses components to model the nuclear system which differ themselves between various types, such as the hydraulic components, control components and so on. Some components can be further discretized as cells for which TRACE calculates the nodal averaged value of the parameters. In this work, the TRACE simulation is used for validation of the CFX subchannel model and the fuel temperature (TFU) solver.

1.4.3 3D kinetics code PARCS

The Purdue advanced reactor core simulator (PARCS) is a 3D reactor core simulator which is able to solve the steady-state as well as the transient, multi-group diffusion equation and low order transport equation (SP3). The general form of the steady-state diffusion equation is written in Eq. 1.10 [DXS12]. PARCS is released by U.S. NRC and can be coupled to other NRC TH codes like TRACE and RELAP5 [XDW+09, HBD+17, EH15, MMNM+11]. Furthermore, with integrated internal TH solver PARCS is also able to perform stand-alone calculation with temperature feedback. The major functions of PARCS are eigenvalue calculations, transient (kinetics) calculation, Xenon transient calculations, decay heat calculation, pin-power reconstruction calculations and depletion calculations. Based on the card input system, PARCS utilizes the maximized default input parameters so that the user only needs to give a minimized input data.

According to different discretization schemes, the solver can be divided into two groups: the coarse mesh finite difference (CMFD) kernel and the fine mesh finite difference (FMFD) kernel [DXS17]. In the CMFD method the mesh size is typically the size of a fuel assembly. A more accurate solution can be achieved using a higher order nodal method to update the neutron current at the interface between two fuel assemblies. Two standard nodal methods offered by PARCS are the nodal expansion method (NEM) and the analytic nodal method (ANM). The NEM method is widely used in many nuclear codes because of its robustness and speed. However, in some cases it can be less accurate [DXS17]. On the other hand, the ANM method is more accurate but less stable when the k_{inf} is closed to entity than the NEM solver. As a solution, PARCS offers a so-called hybrid ANM/NEM solver which benefits from both the robustness of the NEM solver and the accuracy of the ANM solver. By using the hybrid solver PARCS automatically switch to NEM solver when the following criteria is satisfied [DXS17]:

$$\delta = \left| \frac{k_{\text{inf}}}{k_{eff}} - 1 \right| < \epsilon \tag{1.9}$$

where ϵ is defined by the user describing the difference between k_{inf} and k_{eff}.

$$\nabla \cdot D_g \nabla \phi_g + \Sigma_{tg} \phi_g = \sum_{g'=1}^{G} \Sigma_{sgg'} \phi_{g'} + \frac{\chi_g}{k} \sum_{g'=1}^{G} \nu_{g'} \Sigma_{fg'} \phi_{g'} \tag{1.10}$$

where g denotes the neutron group (fast or thermal group in the classic two-group separation), D is the diffusion coefficient which is inversely proportional to the mean free length, ϕ is the neutron flux, Σ_t is the total macroscopic cross section, $\Sigma_{sgg'}$ is the group-to-group scattering cross section, χ is the fission neutrons yield, k is the multiplication factor, ν is the average number of neutrons created per fission and Σ_f is the macroscopic fission cross section.

Another spatial discretization option in PARCS is to use the FMFD kernel for which the size of the mesh is typically the size of a fuel pin. This kernel is

more favorable when transport effects are important (e.g. MOX fuel analysis) which is more accurately solved by using the SP3 transport equations.

1.4.4 3D Monte Carlo code SERPENT

The traditional core physics analysis relies on a multi-stage calculation routine. First, cross section libraries are calculated by some lattice code like HELIOS or CASMO [RSL06] with respect to different state points (temperature, boron concentration, history, control rod insertion, burnups etc.). The spatial homogenized macroscopic cross section data is then used by the core simulator (such as PARCS and SIMULATE) to solve the multi-group diffusion equation or reduced-order transport equation. This method benefits from its low computational usage and the result is reliable while having simplified the transport physics to some degrees in both stages. Another option is to use a Monte Carlo code which can model more complicated geometries and neutron interactions ar the microscopic level without these simplifications. Even though Monte Carlo simulations give a more accurate result, its biggest drawback, the enormous computation cost makes this method still not as practical as the traditional way. On the other hand, Monte Carlo codes are more preferable for the following simulations: unconventional fuel assembly geometry which is beyond the normal lattice code, to capture both axial and radial heterogeneous effect because its intrinsic 3D transport simulation, and for validation process.

SERPENT is a 3D continuous energy Monte Carlo particle transport code which is developed by VTT Technical Research Center of Finland. It has been widely used in critical safety analysis, radiation shielding, dose rate calculation and burn-up calculation. Group constant generation is one of the initial applications of SERPENT code which has been implemented in various research and validation processes. Researches [RSG$^+$14, SGR$^+$15, RSH$^+$17] have shown that the SERPENT generated group constants can be well implemented in PARCS simulating small research reactors with good agree-

ment with 3D Monte Carlo simulations like MCNP and SERPENT. Other researches [FL11, FL12] point out that the difficulty of generating group constants is the critical spectrum calculation because the fission source term has to be scaled after each iteration which has an impact in the flux spectrum and later on in the homogenized group constants. Deterministic codes use leakage corrections to achieve the criticality. The B1 approximation, which is widely applied by deterministic lattice codes, is also implemented in SERPENT to deliver a more reliable result. Improvements have been shown by comparing the macroscopic cross sections between HELIOS and SERPENT (with infinite spectrum and with B1 leakage correction method) calculations [FL11]. Another article [HVFP13] compares the SERPENT and CASMO5M results. Despite of a good agreement of the k-inf factor and the cross sections, large difference lies in diffusion coefficient (with B1 correction around 5% in the fast neutron group).

Chapter 2

Description of the TH models

2.1 Model setup

2.1.1 The CFX model setup

The CFX model setup follows the classic route: mesh generation, preprocessing with CFX-PRE, simulation with CFX-Solver and post-processing with CFX-Post. Before each step is explained, some parameters are listed in Tab. 2.1.

The very basic unit for this work is a single fuel rod subchannel. Since solid domain movement cannot be modeled with CFX, only fluid domain is built. The mesh can be further reduced to a quarter single fuel rod channel when symmetric boundary condition is applied. Fig. 2.1 shows a quarter subchannel mesh with an increasing mesh densities towards the cladding surface. By extruding the plane mesh in axial direction, a 3D mesh is obtained. The subchannel model is used for mesh density investigation as well as for the validation of the TFU solver(explained in 4.3). The FA model is then just a duplication of the subchannel model in radial direction (shown in Fig. 2.2 with 20 guide tubes located in different positions). In the single fuel assembly model, heat flux is applied on the fuel rod cladding surface which

FA design	16x16
Height [m]	3.9
FA pitch length [m]	0.23
Fuel rod pitch length [m]	0.014375
Fuel pellet outer radius [m]	0.004555
Cladding inner radius [m]	0.00465
Cladding outer radius [m]	0.005375
Guide tube inner radius [m]	0.0062
Guide tube outer radius [m]	0.0069
Power per FA [MW]	20
Power density [W/m^3]	3.33E8
Reference pressure [bar]	158
Inlet moderator velocity [m/s]	4.6
Inlet moderator temperature [℃]	290

Table 2.1: Parameters of the TH-model under steady state condition.

is a function of the axial height (more details are explained in section 4.4). Radially the heat flux is the same at the same height. The inlet boundary is set at the bottom (with adjustable inlet temperature and velocity) and the outlet boundary is set at the top (with 0 pressure difference to the reference pressure). The model defines the fluid domain which is based on high-temperature and high-pressure light water. The thermophysical property of water is drawn continuously from the IAPWS 97 database which is integrated inside the CFX solver.

2.1.2 The TRACE model setup

In Fig. 2.3 a simple TRACE subchannel model is shown. Each block stands for a different component for which specific parameters need to be entered. Component 20 and 30 are the break and fill components which define the outlet and the inlet boundary condition respectively. Component 40 is the heat structure component which is connected on one side to the power unit and on the other side to the subchannel. Detailed materials as well as the dimensions are defined in the heat structure component in order to obtain the radial temperature distribution. Component 10 specifies a pipe which

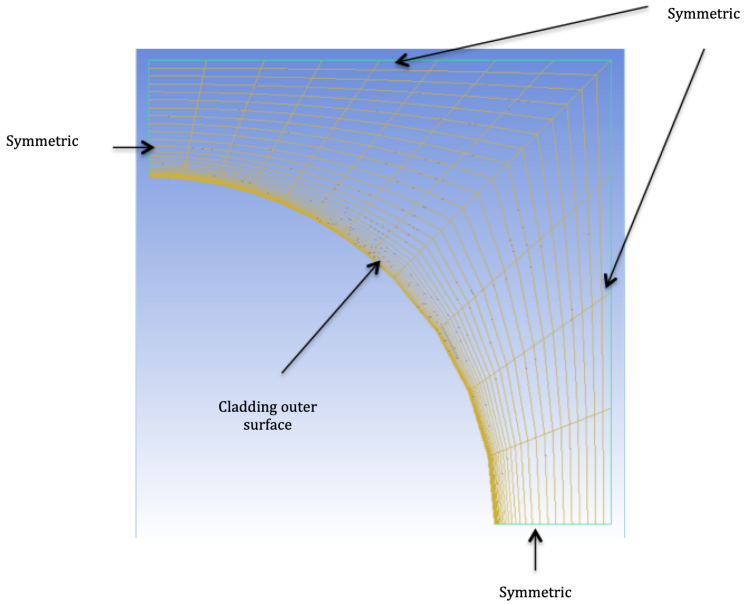

Figure 2.1: An example of the mesh of a quarter single fuel rod channel.

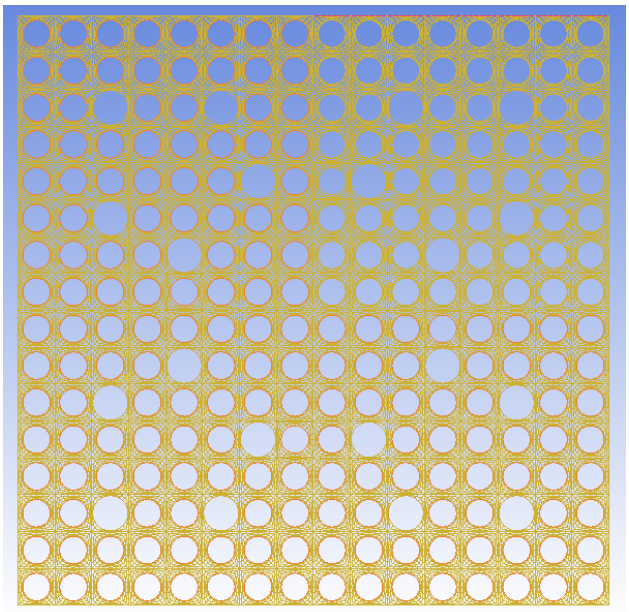

Figure 2.2: An example of the single FA mesh.

models the fluid flow in the subchannel. The parameters of the TRACE subchannel model are shown in Tab. 2.2.

Hydraulic diameter [m]	0.0137247
Flow area [m^2]	1.159E-4
Reference power [W]	8.4745E4
Inlet temperature [K]	563.15
Inlet velocity [m/s]	4.6
Reference pressure [bar]	158
Number of fuel pellet nodes	10
Number of gap gas nodes	1
Number of cladding nodes	5

Table 2.2: Parameters used in the TRACE model.

Since the fluid, heat transfer as well as the kinetics equations give an average estimation over each cell in TRACE, the model apparently needs to have a fine discretization to obtain a more accurate result. In this work the TRACE model is built axially with 10 nodes and 30 nodes seperately and the outcoming influence is analyzed by comparing TRACE results and CFX results (illustrated in Sec. 2.2).

2.2 Comparison of the CFX subchannel model and the TRACE subchannel model

In general, the more mesh cells in the CFX model, the more accurate result can be achieved from the CFD calculation. On the other hand, the computational cost in terms of the calculation time and the memory allocation is much higher with more mesh cells which might make the calculation unattainable without a super computer. From the solver's point of view, one can use the standard k-ϵ method to have faster convergence and more robustness. One can also choose SST method to have a better near-wall simulation. In this part simulations are done using different mesh densities and solvers in the CFX subchannel model to illustrate the influence of the mesh density and solver choice on the results. The results of the CFX subchannel model are also compared with that of the best-estimate code TRACE .

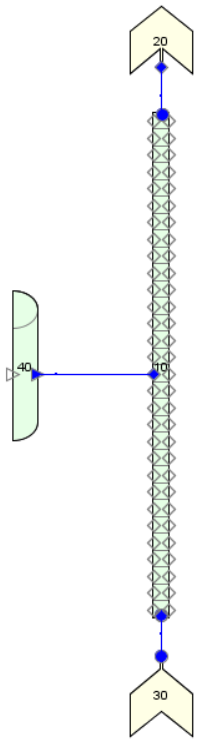

Figure 2.3: TRACE subchannel model.

CFX subchannel model: The basic setup has already been explained in Sec. 2.1.1 and in tab. 2.1. The meshes used for the CFX calculation are generated with ICEM software in a form of hexahedron cells. This cell form benefits from a higher accuracy compared to other kinds of cells (tetrahedron, triangular prism and so on). The parameters, which are changed in this part, are illustrated in Fig. 2.4. Four mesh cases are set up and the mesh parameters are listed in Tab. 2.3. The top view of four meshes is shown in Fig. 2.5 (case 3 and case 4 only differ in the width of the first near wall node which can not be seen from this figure). The heat flux added on the cladding surface is 6.4342E5 W/m^2 which corresponds to the reference power set in the TRACE model shown in Tab. 2.2.

TRACE subchannel model: as already mentioned in Sec. 2.1.2 the model is discretized into 10 and 30 axial nodes in the axial direction. Different axial

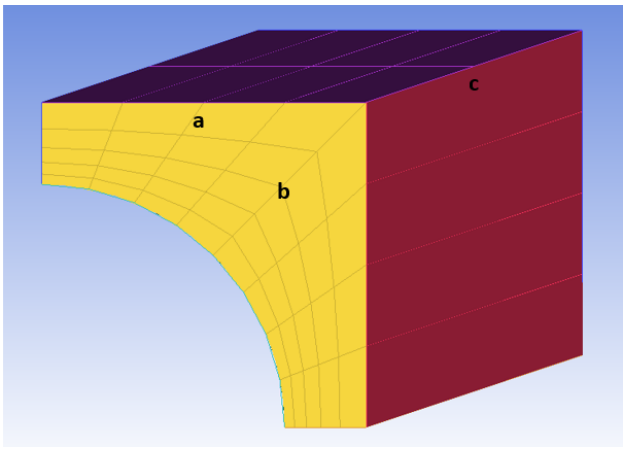

Figure 2.4: Mesh parameters with a being the number of the nodes along the side, b being the number of nodes along the diagonal line and c being the number of nodes along the axial direction.

	case 1	case 2	case 3	case 4
a	5	4	9	9
b	13	6	30	30
c	121	61	241	241
First cell width near wall [mm]	0.01	0.125	0.01	0.005
Mesh cell number	11520	1800	11360	11360

Table 2.3: Mesh parameter settings.

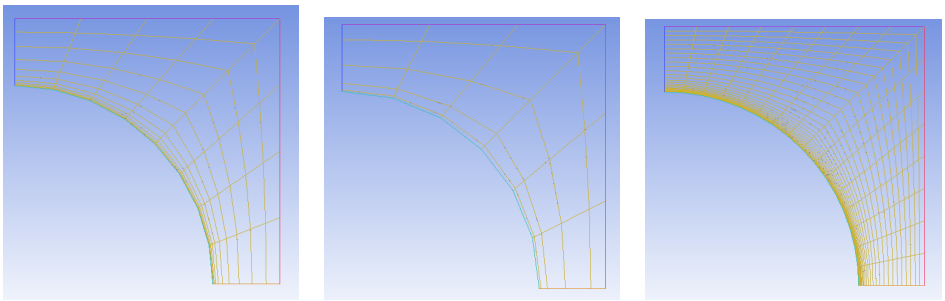

(a) Case 1 (b) Case 2 (c) Case 3 and 4

Figure 2.5: Top view of the meshes used in this part.

discretizations bring a significant difference in the result which is explained as follows.

Fig. 2.6 and 2.7 show the nodal moderator temperature and the nodal

cladding surface temperature of CFX simulation and TRACE simulation in the 10-node case. It is seen that the nodal averaged moderator temperature doesn't change noticeably by increasing the mesh density and TRACE overpredicts moderator temperature (TMO) by 2K in the 10-node case. On the other hand the nodal cladding surface temperature changes with different solvers and meshes. When using the k-ϵ solver, the mesh density doesn't play a big role on getting the accurate cladding surface temperature since wall-function is applied in k-ϵ solver and it can tolerate coarse meshes. The result can differ a lot when using the SST solver. It is observed that using a coarse mesh (case 2) the SST simulation further underpredict the nodal cladding surface temperature while using a finer mesh the SST simulation results are more closer to the TRACE result compared to the k-ϵ solver.

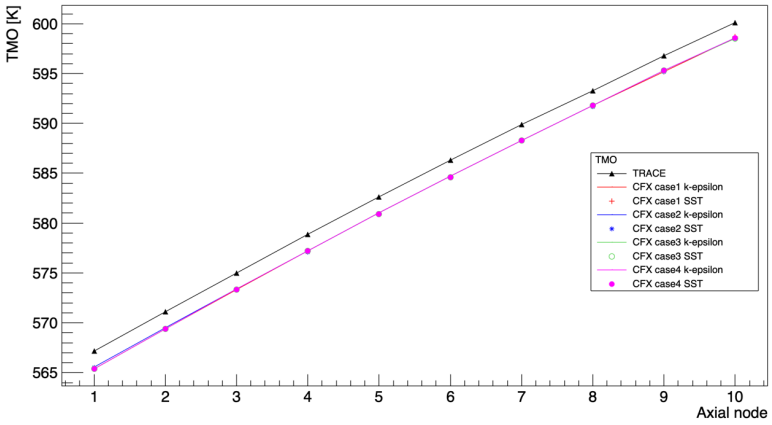

Figure 2.6: The moderator temperature in each axial node in the 10-node discretization case.

Fig. 2.8 and 2.9 show the nodal moderator temperature and the nodal cladding surface temperature of CFX simulation and TRACE simulation in the 30-node case. Same as the 10-node case the mesh density doesn't have a noticeable influence on the nodal moderator temperature. The results from CFX simulation agrees well with the TRACE simulation (difference smaller than 0.3K). On the other hand the k-ϵ solver continuously underpredicts the cladding surface temperature by 3-5K while the SST solver does yield a bet-

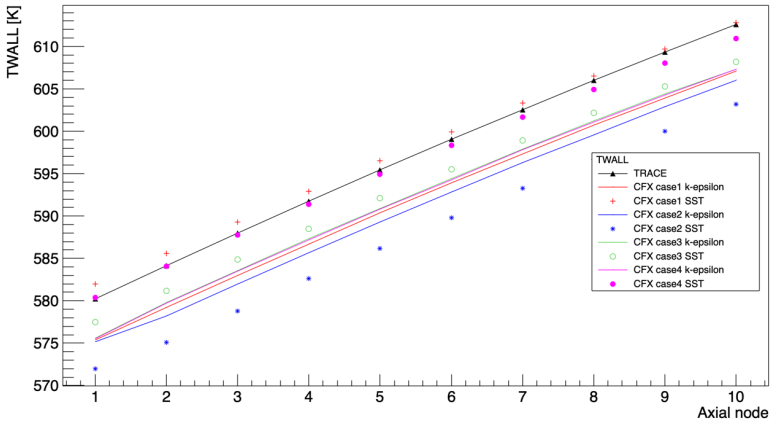

Figure 2.7: The cladding surface temperature in each axial node in the 10-node discretization case.

ter result with a finer mesh especially with a low y^+ value (case 4 y^+ =2.8). Same as the 10-node case, the SST solver delivers a less accurate result compared to the k-ϵ solver using a coarse mesh (case 2).

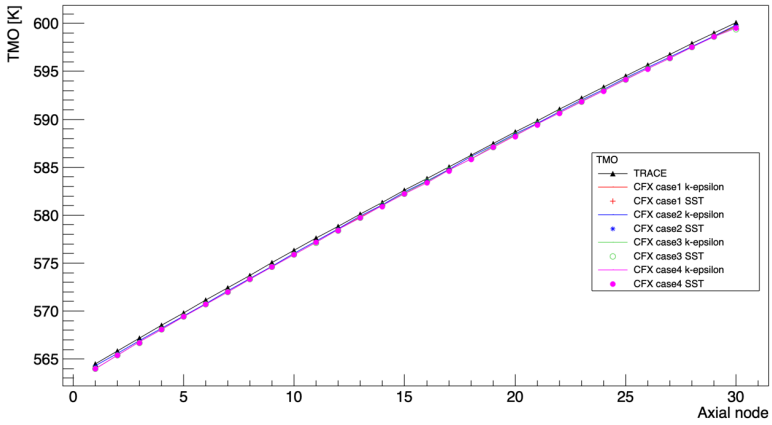

Figure 2.8: The moderator temperature in each axial node in the 30-node discretization case.

From the results shown above it is seen that in order to obtain a better result one should use a mesh with low y^+ value and SST solver. On the other hand, applying these two criteria does require higher computational

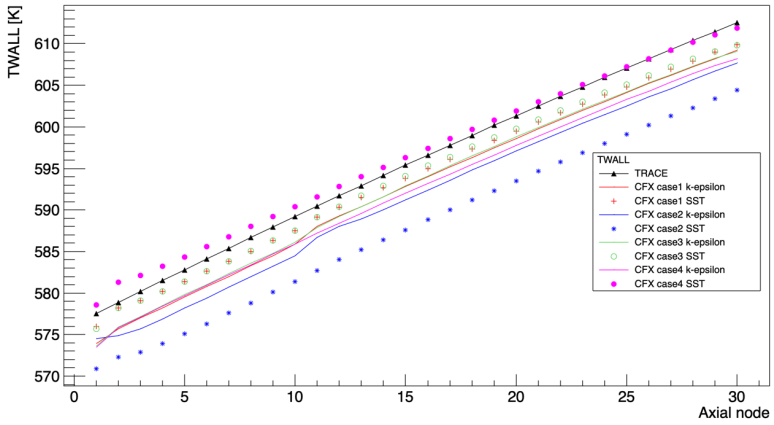

Figure 2.9: The cladding surface temperature in each axial node in the 30-node discretization case.

power. When the model is further extended to the fuel assembly model or the 3x3 FA matrix, the requirement of memory increases dramatically. The memory allocation investigation based on the mesh cell number is illustrated in Fig. 2.10. Based on the cluster setup where the calculations are carried out, the memory allocation should not exceed 64GB. In the end, compromise has to be made for the CFD part (the mesh in case 2 and k-ϵ are chosen) in order to make the coupling simulation achievable.

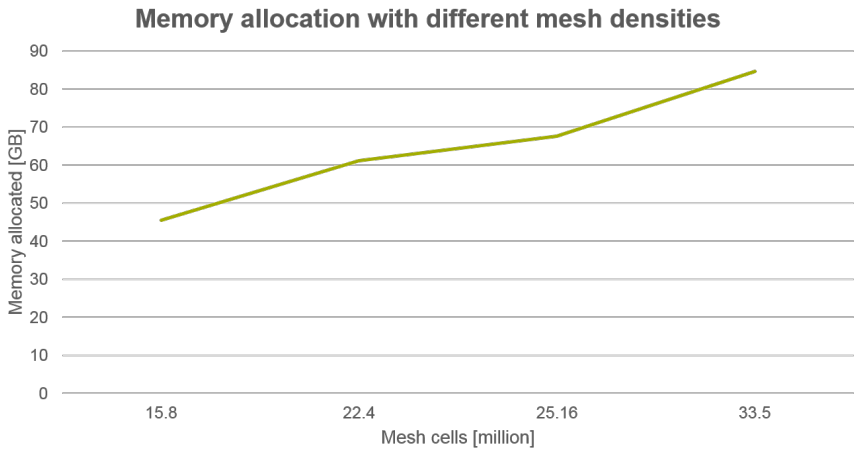

Figure 2.10: Memory allocation with different meshes.

2.3 Development of the 3x3 FA CFX model

In a more complex model like the 3x3 FA model (shown in Fig. 2.11), the model itself is built by a duplication of the single fuel assembly model. Different names are given for each mesh domain so that during the coupling procedure temperature feedback can be easily and precisely extracted from the CFX model. In total 270 domains are defined for the 3x3 FA model. Symmetric boundary condition is used on the periphery faces and interfaces have to be built between neighboring FAs to enable the cross flow and heat transfer. Heat flux is applied on the fuel rod cladding surface which can also vary between different fuel assemblies or even within the same fuel assembly (this requires the value from the pin power fraction calculation). Each fuel assembly has its own inlet and outlet boundary condition to apply local disturbances on different fuel assemblies. The center fuel assembly are set to be a deformable domain so that the fuel rods in the center fuel assembly can move in different directions according to the user input.

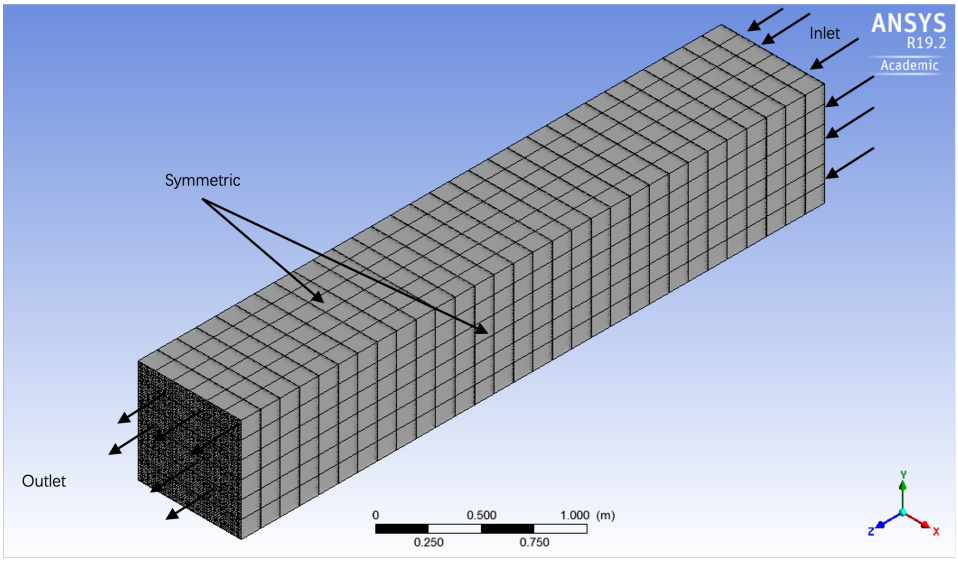

Figure 2.11: 3x3 FA model in CFX-PRE with inlet boundary, outlet boundary and symmetric boundary labeled.

As already illustrated in Sec. 2.2 the mesh is further reduced for the 3x3 FA

matrix because of the limited computation capacity.

2.4 Summary

In this section, a brief introduction of CFD calculation is shown. Different turbulence models are introduced and discussed.

As the next step, the CFX subchannel model is cross-validated through comparing the moderator temperature and the cladding surface temperature with the best-estimate code TRACE. In this step different axial discretizations, mesh densities as well as the solving methods (k-ϵ and SST methods) are investigated for CFX model. In the 10-axial-node investigations the results show an unsatisfying disagreement in moderator temperature and cladding wall temperature while in the 30-axial-node investigations, the nodal averaged moderator temperature agrees well in both models. On the other hand, using SST method on a finer mesh does give a better estimation of the cladding wall temperature and the advantage of using SST method applies only for the meshes with a small y^+ value. Otherwise the discrepancy grows larger. Instead, one can use the k-ϵ method which is less y^+ dependent but with a disagreement of the cladding wall temperature of around 3-5K.

For the subchannel model one can use a finer mesh with a relatively small y^+ value and the advantages of more accurate simulation with SST method can be taken. However, when the model expands to the single fuel assembly model or even to the 3x3 fuel assembly model, which naturally leads to a higher number of wall modeling and consequently a higher memory requirement, one has to take the computation cost into account. The memory usage is investigated on different number of mesh cells. Based on the current computation capacity, the modeling strategy (the mesh density and the solver method) is fixed for latter models.

Chapter 3

Description of the neutronic model

3.1 The PARCS model

In this work, PARCS focuses on calculating the RPF value of each node and of each fuel assembly. The model contains 32 nodes in the axial direction including 30 nodes of the active fuel zone and 2 reflector nodes on the top and bottom. In the radial direction the model has a 3x3 FA configuration without side or corner reflector nodes. Fig. 3.1 illustrates the FA configuration in the radial and the axial view. The boundary condition is set to be "0 incoming current" in the axial direction. In the radial direction the boundary condition can differ from "reflective" or with specific "Albedo factors" depending on the scenarios (Albedo factor describes the ratio of the incoming current and the outcoming current). In order to obtain a non-uniform power distribution, two types of FAs are used. Detailed information of the FA composition is explained in Sec. 3.2.

There are several ways of specifying the cross section data for PARCS calculation. One can specify the multi-group group constants of each node which includes the macroscopic transport cross section Σ_{tr}, the macroscopic absorp-

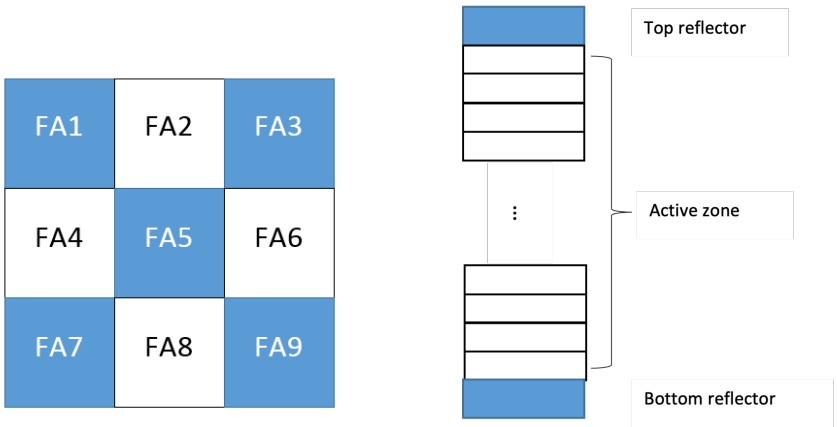

(a) (b)

Figure 3.1: The FA configuration in radial (a) and axial (b) view. a) A chessboard configuration is used in order to obtain a non-uniform power distribution in the radial direction. Two types of FAs are applied and the color indicates where each type of FA is located. b) Just a single fuel assembly model in the axial view is illustrated here.

tion cross section Σ_{ab}, the nu-fission cross section $\nu\Sigma_{fiss}$, the kappa-fission cross section $\kappa\Sigma_{fiss}$ and the down-scattering cross section Σ_s. The temperature dependence, the boron concentration dependence as well as the control rod insertion dependence are shown in Eq. 4.1. One can specify the cross section change per each parameter and PARCS is able to perform criticality or boron concentration search calculation together with internal or external TH feedback. The other way to insert the cross section data is to apply the depletion "DEPL" block and the burnup dependent macroscopic cross sections are read from the so-called PMAXS file which can be converted from other cross section file of CASMO, HELIOS or SCALE by code GENPMAX. Additional 3D TH parameter and boron concentration parameter can be read from a ASCII file following a specific format. In this work the first method is used to input the cross section data since the PMAX file cannot handle the discontinuity factor (DF) (the assembly discontinuity factor (ADF) and the corner discontinuity factor (CDF)) changes and FA bow cases while the cross section data is more free to modify using the first method.

3.2 The SERPENT model

The SERPENT model consists of two parts: the single fuel assembly part for group constants generation and the 3x3 fuel assembly part for validation. In order to have a heterogeneous configuration in the 3x3 FA matrix, two types of fuel assembly are used. Both types of fuel assembly consist of 256 rods in total, 236 of which are fuel rods and the rest is the guide tube containing only moderator. What differs in these two types of fuel assemblies is that one fuel assembly contains 8 fuel rods with gadolinium while the other one contains only uranium fuel rods. The U-rod has a 3.95 w% enrichment of U-5 while the Gd-rod has a 2.3 w% enrichment of U-5 and 7 w% of Gd_2O_3. Fig. 3.2 shows the configurations of the U-FA and of the Gd-FA. The Gd-rods are located close to the guide tubes where the neutron flux is supposed to be high. Natural gadolinium has more than ten thousands times higher thermal neutron capture cross section than U-238 (especially Gd-155 around 60700 barn and Gd-157 around 254000 barn compared to U-238 around 2.683 barn). Therefore introducing gadolinium will suppress the reactivity of the fuel assembly and the relative power fraction of the Gd-FA is lower than the U-FA.

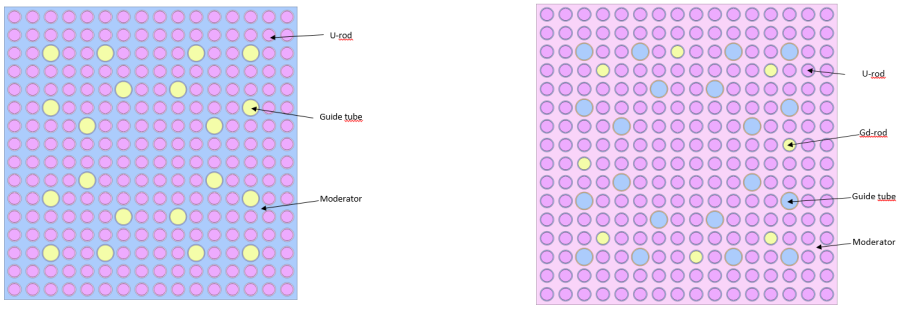

(a) (b)

Figure 3.2: The configurations of the U-FA (a) and of the Gd-FA (b).

Before introducing SERPENT input setups, one thing which needs to be mentioned is that in CASMO5 calculations the thermal expansion option is by default turned on. In order to compare the results from both SERPENT

and CASMO5, a separated calculation script is written according to the CASMO subroutine [Stu11] to include the thermal expansion effect. The material composition is given in SERPENT as number density which is taken from the CASMO output file. As the number density defined in Eq. 3.1 is only proportional to the material density, it can be solved with Eq. 3.2.

$$n = \frac{\rho w N_A}{M} \tag{3.1}$$

$$n = n_{ref} \frac{\rho}{\rho_{ref}} \tag{3.2}$$

where w is the weight percentage of each nuclide, N_A is the Avogadro constant which equals to 6.022E23 mol^{-1}, M is the molar mass of that nuclide and ref denotes the reference state point.

The cross section library used in SERPENT is the ENDF/B-VII.0 library which is the same as in CASMO5. The libraries are offered with temperatures at 300K, 600, 900, 1200, 1500 and 1800K. A Doppler-broadening preprocessor routine is built in SERPENT resulting in a more accurate simulation of the nuclear reactions at temperatures other than the standard library temperatures.

Part of this work focuses on generating two-group (thermal group and fast group) group constants with SERPENT. The energy groups are separated at 0.625 eV. The B1 fundamental mode is turn on with 236 energy groups, the same as in SCALE. The boundary condition is set to be reflective in x-, y- and z-direction. Another set of critical parameters are the number of neutrons per generation, the number of the inactive cycles and the number of the active cycles. In each iteration, the fission source is assumed to emit a specific number of neutrons which is the first parameter. Each neutron might encounter different neutron reactions and the location where the fission reaction takes place will be recorded for the next iteration. If the number of fissioned neutrons is smaller than that of the neutron source, which means that the multiplication factor is smaller than 1, the neutron source for the

next generation is then up-scaled back to this number. The inactive cycle are non-recorded cycles during which the fission source is supposed to converge. The active cycles are recorded cycles during which the results are collected. Both the number of neutrons per generation and the number of inactive cycles influence the fission source convergence. The more neutrons per generation, the faster the convergence is reached. The more inactive cycles, the more confident the convergence is reached. The number of active cycles is more related to the statistical error. The more active cycles, the smaller the statistical error is. On one hand, one need to give a reasonable set of these parameters to ensure that the convergence is reached and the statistical error is small enough. On the other hand, when the number gets larger, the need of memory as well as the computation time will also increase accordingly.

The cross sections generated by SERPENT are extracted and written in a separated file which can be treated as a cross section data bank. This data bank is read in every iteration and according to the state point the group constants, which are needed for the PARCS calculation, are generated through an interpolation subroutine embedded in the PARCFX coupling model. The evaluation of the SERPENT cross sections is illustrated in the next section.

3.2.1 The evaluation of the SERPENT results

As already mentioned in Sec. 3.2 the biggest challenge of using Monte Carlo code to generate homogenized group constants lies on the diffusion coefficient. In this part the SERPENT group constants are evaluated and compared with CASMO group constants with respect to different state points. Each group constant which is needed in the PARCS calculation and its corresponding card name in SERPENT output file are listed in Tab. 3.1.

In Tab. 3.2 the comparison between SERPENT calculation and CASMO calculation is shown for the reference case (with TMO=583.15K, TFU=873.15K, BOR=500ppm). In general the SERPENT generated group constants agree

Macroscopic group constants	SERPENT card name
Transport Σ_{tr}	INF_TRANSPXS
Absorption Σ_{ab}	INF_ABS
Nu-Fission $\nu\Sigma_f$	INF_NSF
Kappa-Fission $\kappa\Sigma f$	INF_KAPPA INF_FISS
Scattering Σ_s	INF_S0
ADF	DF_SURF_DF
CDF	DF_CORN_DF

Table 3.1: Group constant names and the corresponding SERPENT card name.

well with the CASMO result except for the diffusion coefficient with a maximal discrepancy of 7.77% in the B1 fundamental mode. SERPENT overestimates the fast group diffusion coefficient by c.a. 6% and underestimate the diffusion coefficient by maximal 2.3% using the infinite medium mode. Similar behavior can also be found in the previous research [HVFP13]. It should be mentioned that in the default mode of CASMO calculation the fundamental mode is turned off [Stu11] which can explain to some extent the SERPENT result using infinite medium is much closer to the CASMO result than the SERPENT result using B1 fundamental mode. Further discussion regarding whether to use infinite medium group constants or group constants with B1 fundamental mode will not be repeated. For the following investigations the infinite medium group constants are used based on the good agreement of k-inf factor with CASMO result.

Fig. 3.3-3.12 illustrate how the group constants change with respect to moderator temperature, fuel temperature and boron concentration. In general, the group constants change linearly with boron concentration and the square root of fuel temperature. On the other hand the group constants change nonlinearly with moderator temperature. In classic neutronics code the group constants should have a linear dependency on moderator temperature and nonlinear dependency on moderator density (shown in Eq. 4.1). In this work, the moderator density change is already included when defining a new moderator temperature case and therefore its effect is superpositioned con-

U-FA	CASMO	SERPENT-inf	Diff.	SERPENT-B1	Diff.
k-inf	1.33166	1.33179	13 pcm	1.32323	843 pcm
D-1	1.4447	1.53251	6.078%	1.3944	-3.482%
D-2	0.398	0.38865	-2.349%	0.420795	5.727%
Ab-1	0.0096694	0.00969779	0.294%	0.00933275	-3.482%
Ab-2	0.092562	0.092854	0.315%	0.0927237	0.175%
NuF-1	0.007563	0.00753	-0.391%	0.00734131	-2.931%
NuF-2	0.1536	0.1541	0.329%	0.153885	0.186%
DS	0.016209	0.0165571	2.638%	0.0153691	-5.182%

Gd-FA	CASMO	SERPENT-inf	Diff.	SERPENT-B1	Diff.
k-inf	1.23006	1.2293	-76 pcm	1.22469	537 pcm
D-1	1.4452	1.53306	6.08%	1.40162	-3.02%
D-2	0.39029	0.386748	-0.91%	0.420612	7.77%
Ab-1	0.0097936	0.00981732	0.24%	0.00955253	-2.46%
Ab-2	0.098819	0.09919250	0.38%	0.09909970	0.28%
NuF-1	0.00747110	0.00744408	-0.36%	0.0073803	-2.18%
NuF-2	0.14962	0.150034	0.28%	0.14989	0.18%
DS	0.01611	0.016454	2.14%	0.0156107	-3.10%

Table 3.2: Comparison of the group constants from SERPENT result and CASMO result of U-FA and Gd-FA. The abbreviations on the left column have the following meanings: k-inf for the multiplication factor with infinite medium, D for diffusion coefficient, Ab for the macroscopic absorption cross section, NuF for the nu-fission and DS means the macroscopic down-scattering cross section.

sequently. When looking at the group constants separately the moderator temperature has a dominant effect on the transport cross section and it decreases when the moderator temperature increases. Similar tendency can also be seen in all other group constants. As for the absorption cross section, it increases with increasing fuel temperature due to the Doppler effect in the fast group and decreases with an increasing fuel temperature in the thermal group. Besides the absorption cross section increases dramatically with an increasing boron concentration since boron-10 has a large neutron absorption cross section. In both the nu-fission and kappa-fission group constants a negative effect of the fuel temperature and boron concentration can be seen. In the k-inf figure 3.12 it is seen that the moderator temperature coefficient can reach positive region when the boron concentration is above around 1700ppm. When the moderator temperature increases, the moderator density decreases. On one hand, less neutrons will be moderated and therefore it brings a negative effect on the reactivity. On the other hand, less neutrons will be absorbed by boron-10 due to decreasing moderator density which introduce a positive reactivity. When the boron concentration is high enough, the second effect takes the dominant role and results in a positive moderator temperature coefficient (can also be seen in Fig. 3.5 and 3.6). Although the MTC is not a constant value over the moderator temperature range which can also be seen in Fig. 3.12, by rule of thumbs analyzing k-inf at state points with TMOs (563.15K, 583.15K) and TFUs (563.15K, 873.15K) at different boron concentration (BOR)s gives a roughly impression of the magnitude of MTC and the fuel temperature coefficient (FTC). The result can be found in Tab. 3.3. It needs to mention that with different boron concentrations (for example 500ppm and 2400ppm) the neutronic response can behave oppositely to moderator temperature change. A similar behavior can be found for the Gd-FA case in Tab. 3.4

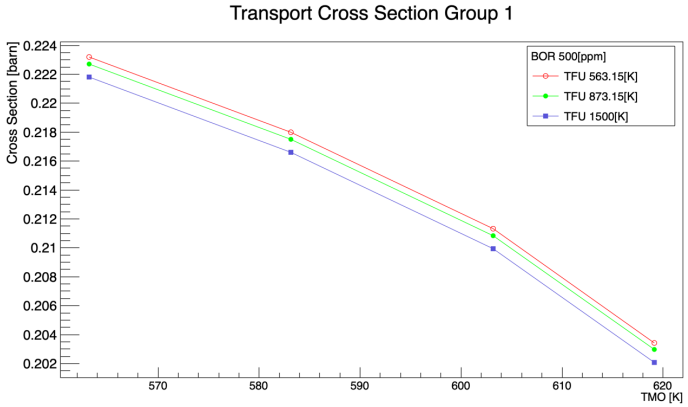

(a)

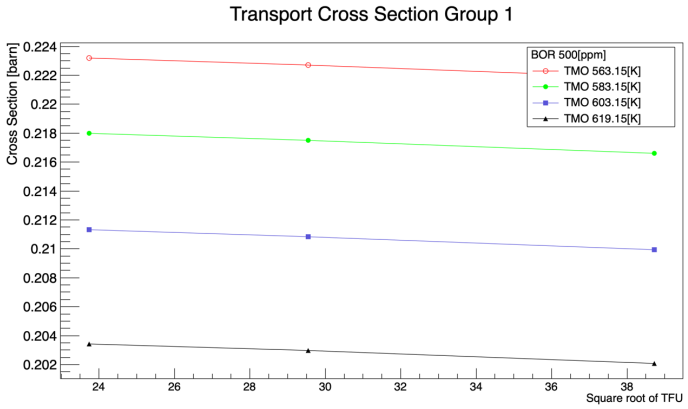

(b)

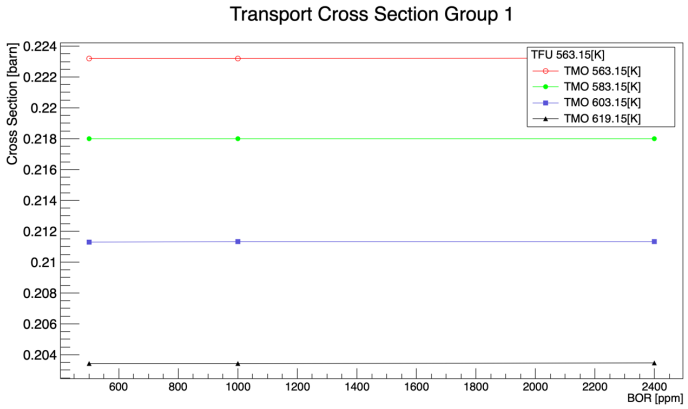

(c)

Figure 3.3: Macroscopic transport cross section group 1 of U-FA with respect to moderator temperature, fuel temperature and boron concentration.

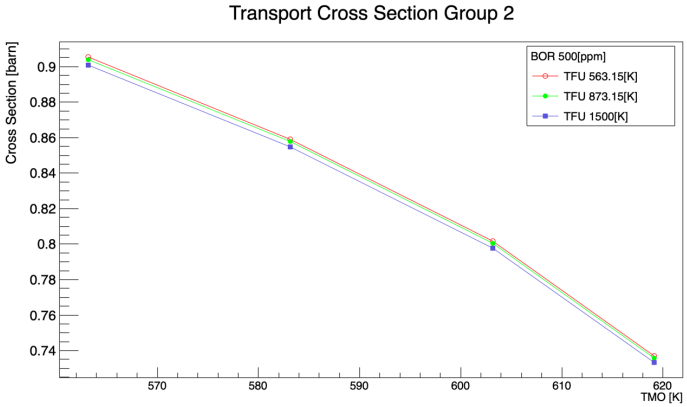

(a)

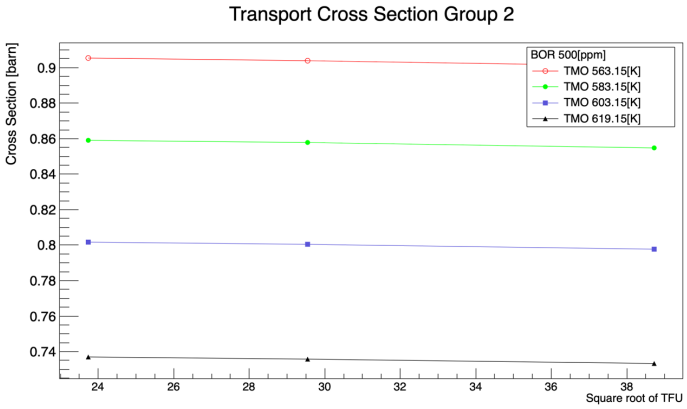

(b)

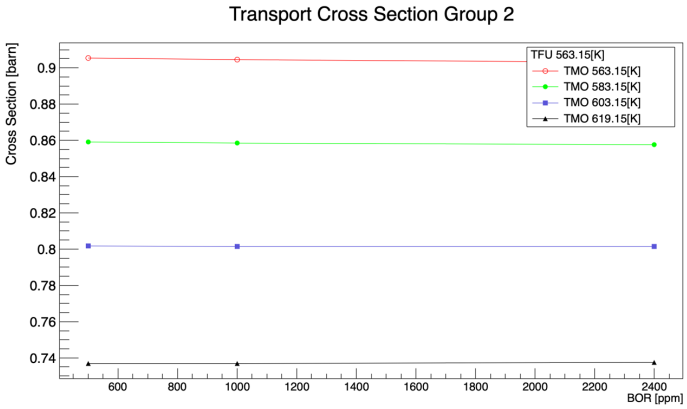

(c)

Figure 3.4: Macroscopic transport cross section group 2 of U-FA with respect to moderator temperature, fuel temperature and boron concentration.

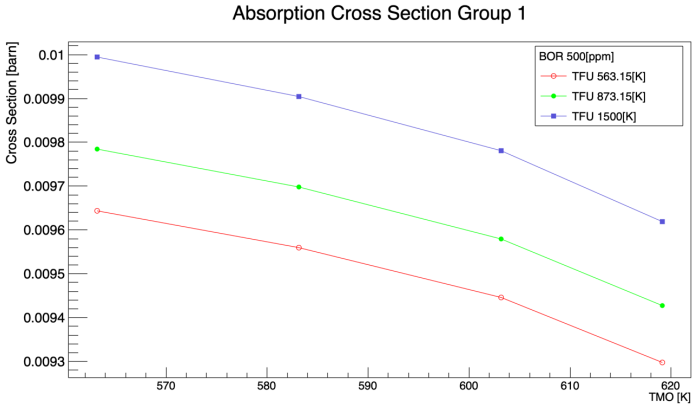

(a)

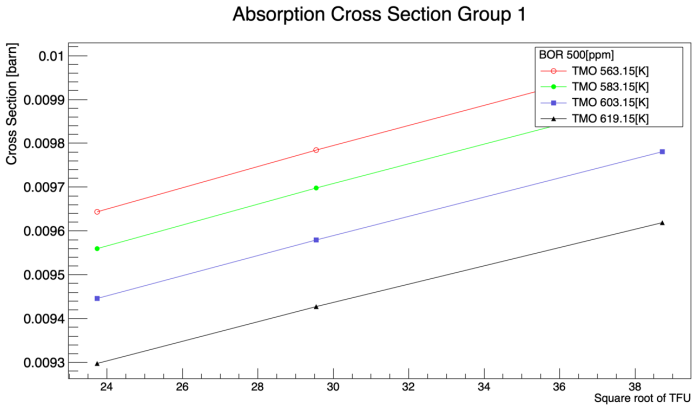

(b)

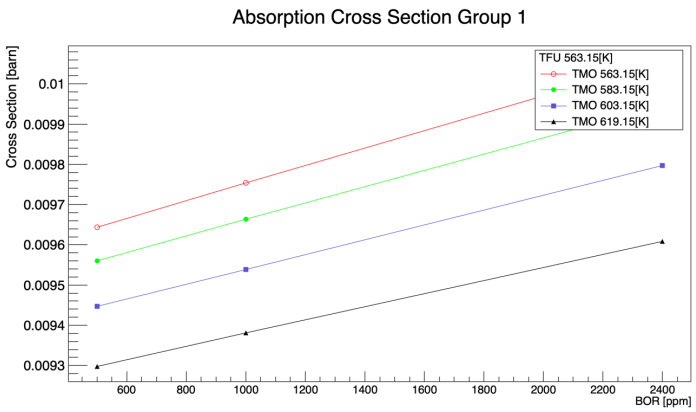

(c)

Figure 3.5: Macroscopic absorption cross section group 1 of U-FA with respect to moderator temperature, fuel temperature and boron concentration.

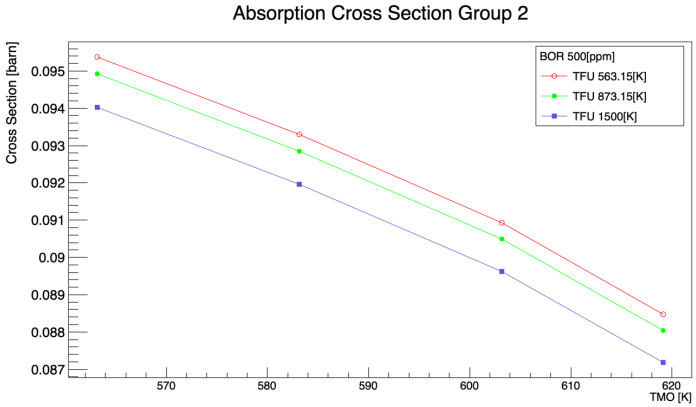

(a)

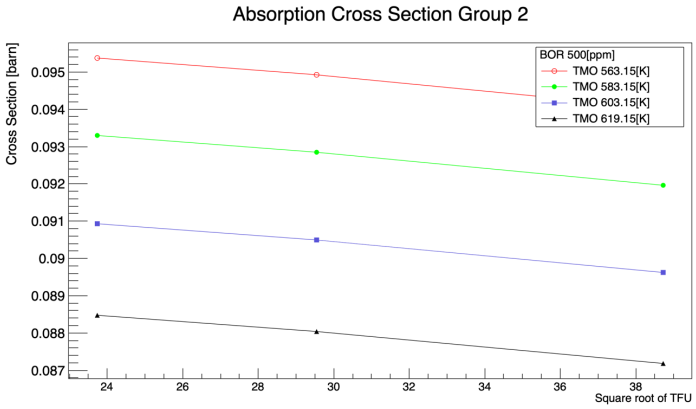

(b)

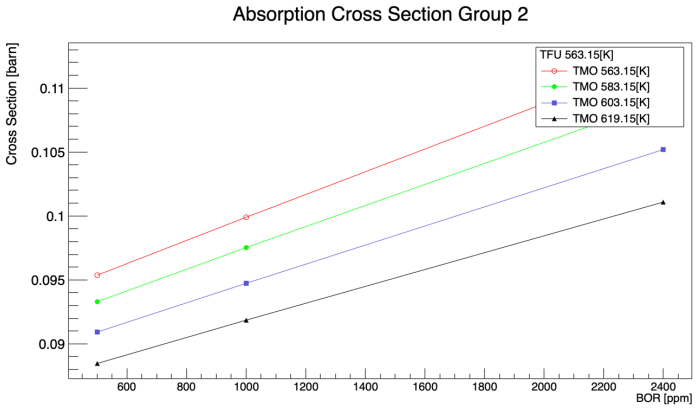

(c)

Figure 3.6: Macroscopic absorption cross section group 2 of U-FA with respect to moderator temperature, fuel temperature and boron concentration.

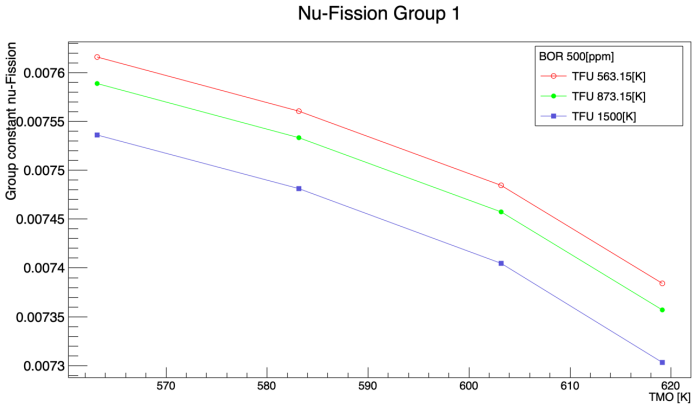

(a)

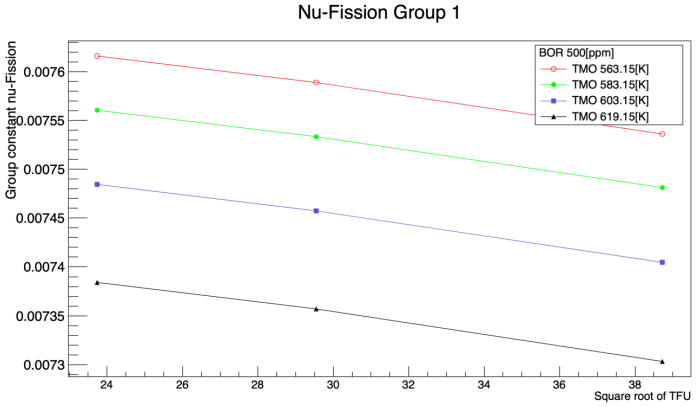

(b)

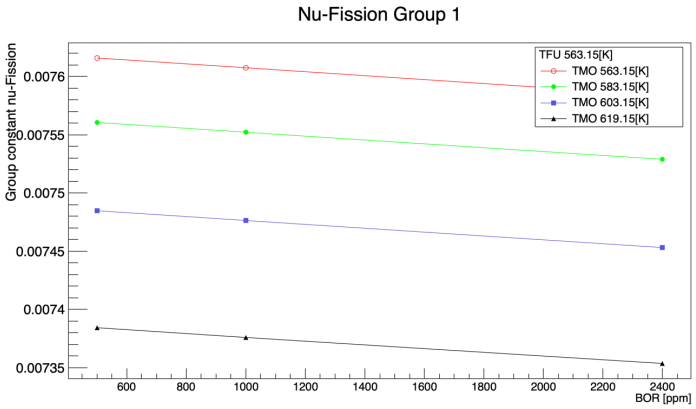

(c)

Figure 3.7: Nu-fission Group 1 of U-FA with respect to moderator temperature, fuel temperature and boron concentration.

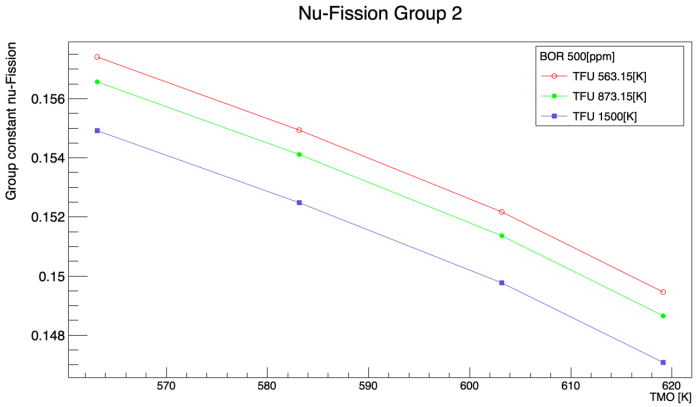

(a)

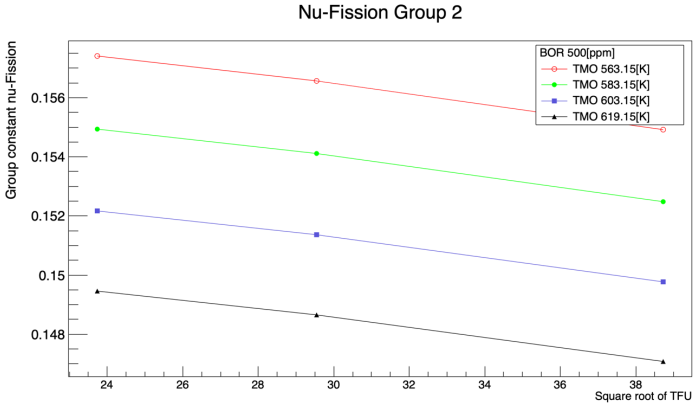

(b)

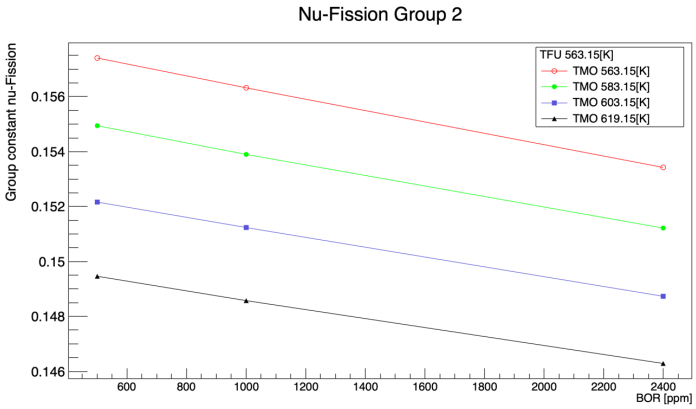

(c)

Figure 3.8: Nu-fission Group 2 of U-FA with respect to moderator temperature, fuel temperature and boron concentration.

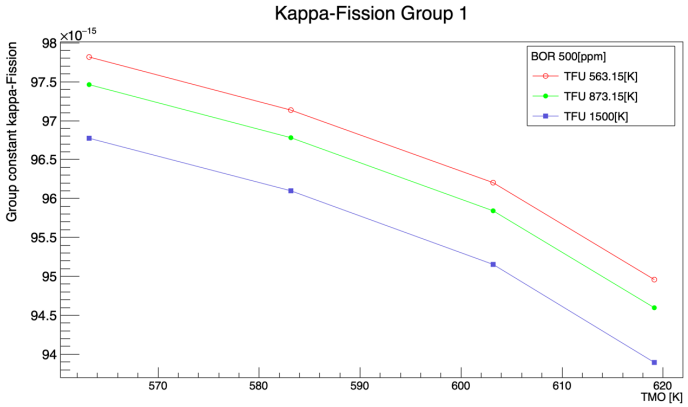

(a)

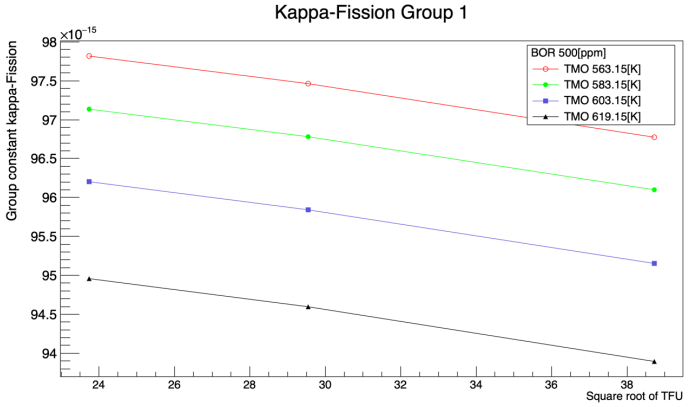

(b)

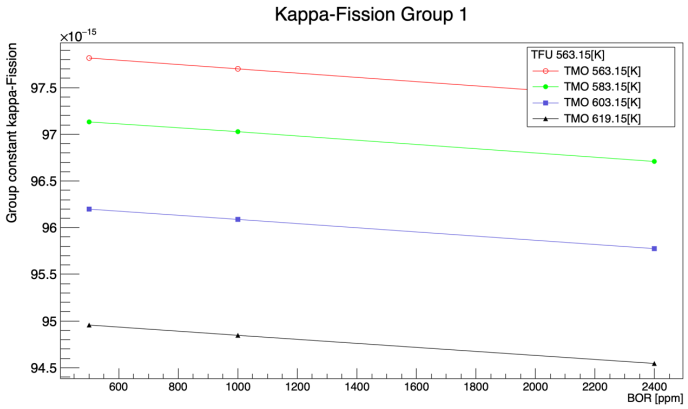

(c)

Figure 3.9: Kappa-fission group 1 of U-FA with respect to moderator temperature, fuel temperature and boron concentration.

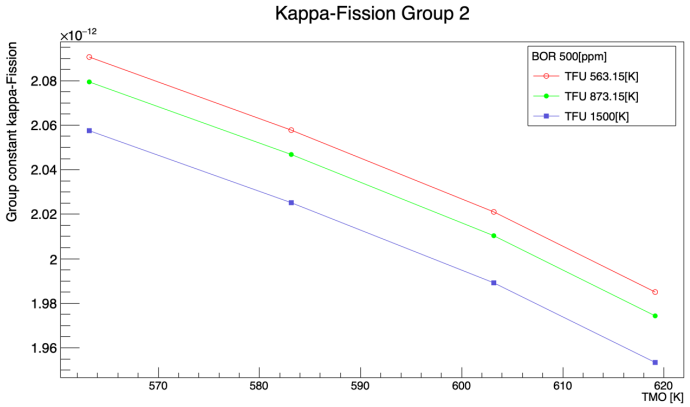

(a)

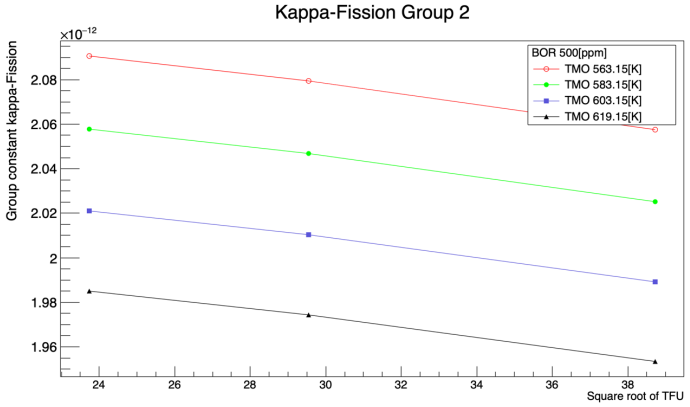

(b)

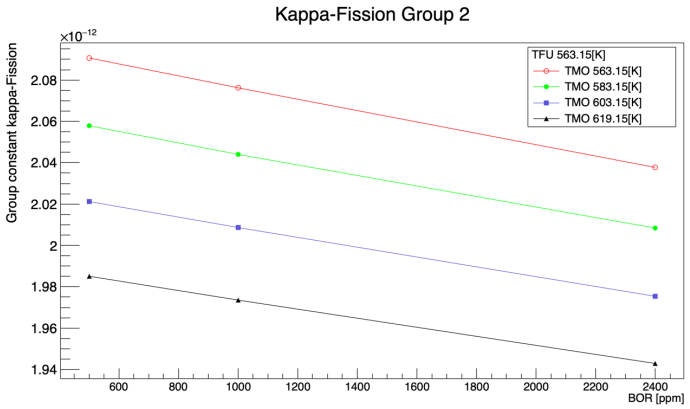

(c)

Figure 3.10: Kappa-fission group 2 of U-FA with respect to moderator temperature, fuel temperature and boron concentration.

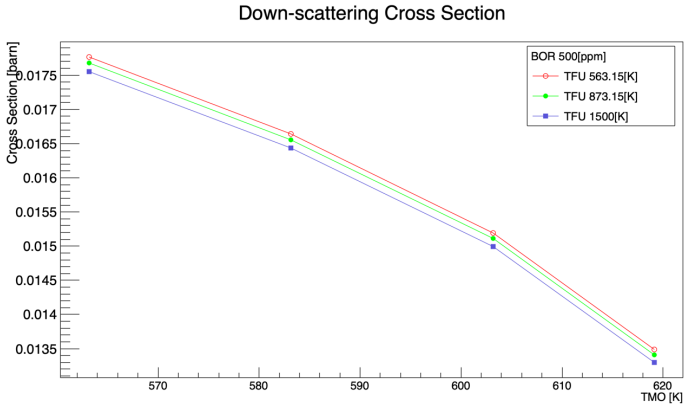

(a)

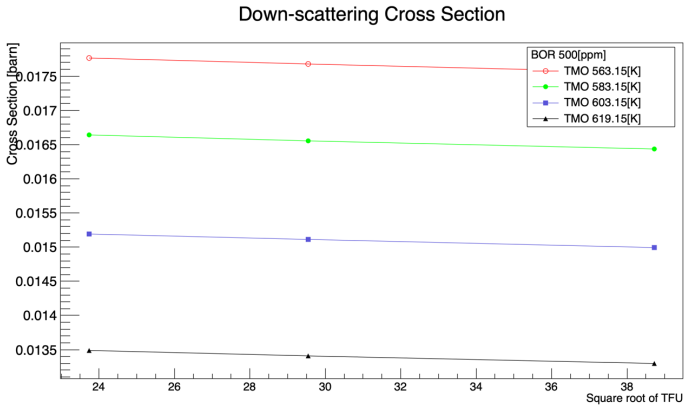

(b)

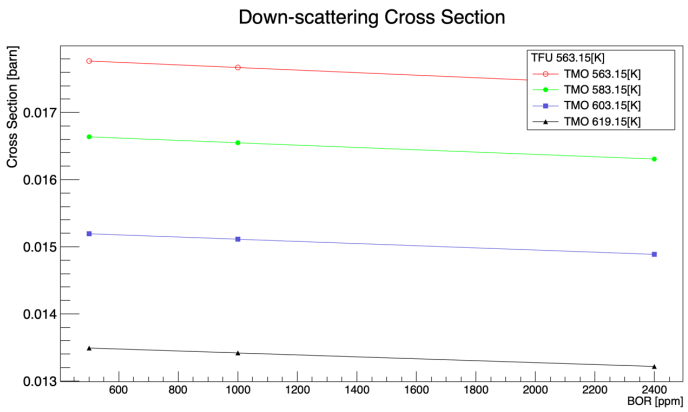

(c)

Figure 3.11: Macroscopic down-scattering cross section of U-FA with respect to moderator temperature, fuel temperature and boron concentration.

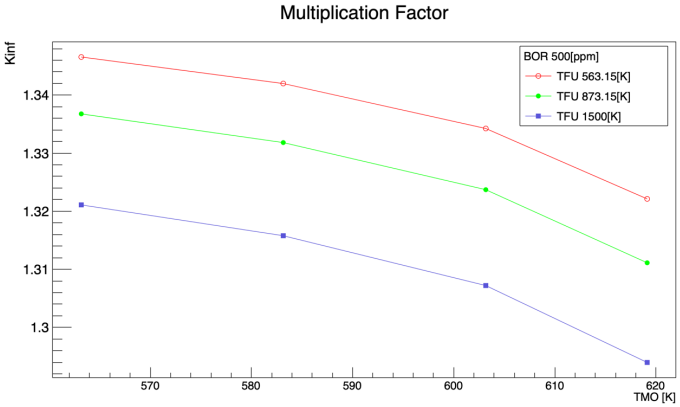

(a)

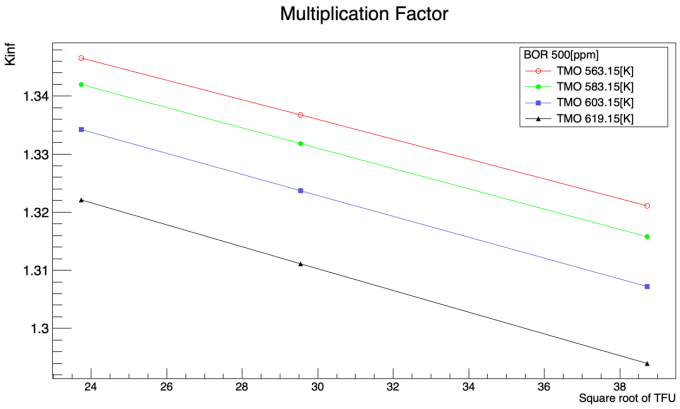

(b)

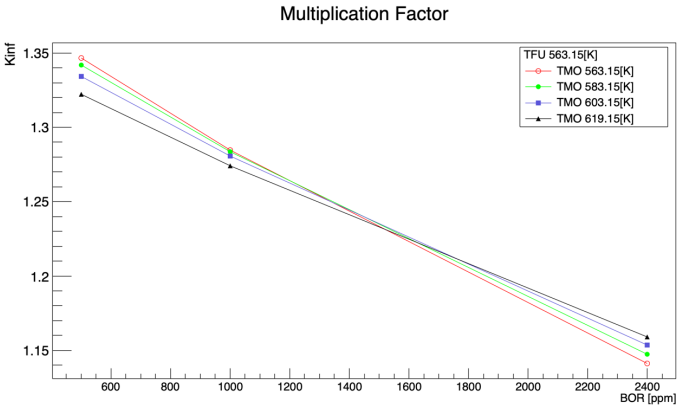

(c)

Figure 3.12: k-inf of U-FA with respect to moderator temperature, fuel temperature and boron concentration.

Boron concentration [ppm]	MTC [pcm/K]	FTC [pcm/K]
500	-13.90	-1.84
1000	-4.22	-1.93
2400	22.61	-2.18

Table 3.3: The moderator temperature coefficient and fuel temperature coefficient with different boron concentrations (U-FA).

Boron concentration [ppm]	MTC [pcm/K]	FTC [pcm/K]
500	-18.28	-2.06
1000	-8.12	-2.19
2400	19.18	-2.45

Table 3.4: The moderator temperature coefficient and fuel temperature coefficient with different boron concentrations (Gd-FA).

3.2.2 Implementation of SERPENT XS in PARCS model

In this section both the CASMO and the SERPENT cross sections are implemented in the PARCS model to have a general overview of the the difference in the outcoming result. Black boundary condition is applied in axial direction and reflective boundary condition is applied in the radial direction. The axial power distribution should have a parabolic shape with its maximum at half height and its minimum at the top and bottom layer. Fig. 3.13 and 3.14 plot the relative difference based on the CASMO result. The result agrees well with a maximal difference below 2% in the single fuel assembly model and 1% in the 3x3 fuel assembly model. On the other hand, Fig. 3.15 shows the radial RPF distribution with the 3x3 FA matrix model and Gd-FA in the center. The radial RPF distribution agrees well between both results with an overestimation of the Gd-FA power of max. 0.46% and a underestimation of the U-FA power of max. 0.55%. As a result, SERPENT XSs can be used for the 3x3 FA model with a negligible difference with the CASMO result.

$$\text{Difference} = \frac{\text{RPFs-RPFc}}{\text{PRFc}} \tag{3.3}$$

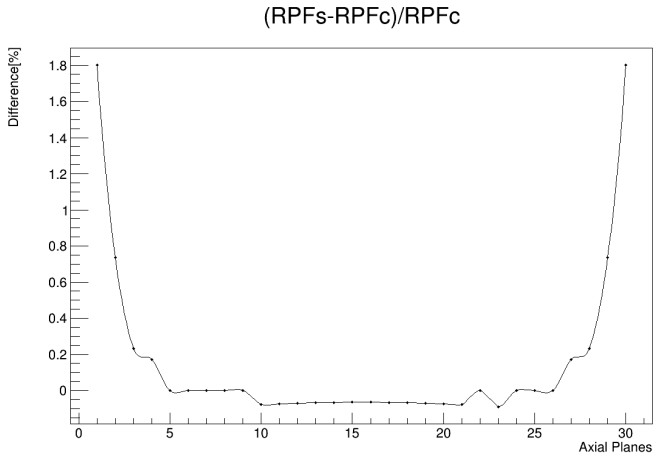

Figure 3.13: Comparison of the axial power distribution using CASMO and SERPENT cross sections with single fuel assembly model.

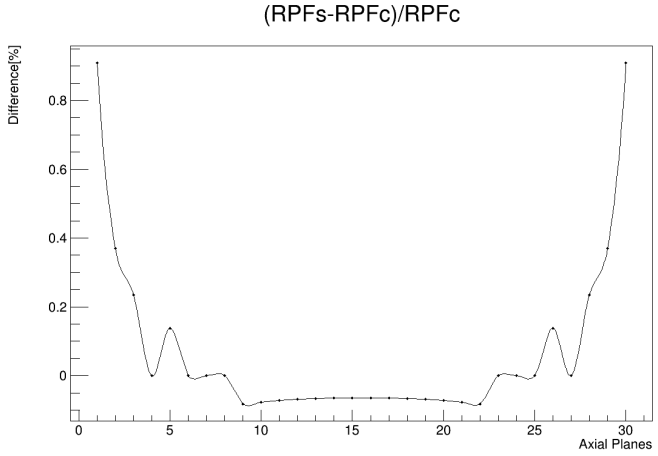

Figure 3.14: Comparison of the axial power distribution using CASMO and SERPENT cross sections with 3x3 fuel assembly matrix model.

3.2.3 Preparation of the pin power factors for the FA bow case with 3x3 FA geometry

The group constants which are shown in the last section 3.2.1 are homogenized over the entire fuel assembly. When the fuel assembly is under the bowing condition which implies that the water gap between two fuel assemblies gets narrower, the group constants should not change much theoreti-

RPFC RPFS DIFF		
0.9298 0.9344 0.46%	1.0770 1.0715 -0.55%	0.9298 0.9344 0.46%
1.0770 1.0715 -0.55%	0.9729 0.9766 0.37%	1.0770 1.0715 -0.55%
0.9298 0.9344 0.46%	1.0770 1.0715 -0.55%	0.9298 0.9344 0.46%

Figure 3.15: Comparison of the radial power distribution using CASMO and SERPENT cross sections with 3x3 fuel assembly matrix model. RPFC stands for the RPF result with CASMO XS and RPFS stands for the RPF result with SERPENT XS.

cally since these values are homogenized over the entire fuel assembly. On the other hand, the ADF and the pin power distribution changes because the fuel to moderator ratio changes on the periphery side which results in a lower or higher moderation effect and a change in the power distribution not only of the fuel pins but also of the fuel assemblies. In Tab. 3.5 the group constants as well as the ADFs are listed for the reference cases (TMO=583.15K, TFU=873.15K, BOR=500ppm) with and without fuel assembly bow. The fuel assembly bow is simply assumed to be the center fuel assembly undergoing a displacement of 2 mm in both x- & y-directions in a 3x3 FA matrix. A graphic illustration is shown in Fig. 3.16. It is seen that under the fuel assembly bow condition the ADFs change to different degrees whereas the group constants stays quite the same. Due to the decreased water gap and moderation effect to the east and north side of the center fuel assembly, the ADFs on these sides increase in the fast group and decrease in the thermal group. The reason that the group constants don't change or don't change much is that the bowed fuel assembly (the fuel pins) is still located in that

	Without bow	With bow
D-1	1.532	1.532
D-2	0.388	0.388
Ab-1	0.00969749	0.00969383
Ab-2	0.00928537	0.0926181
NuF-1	0.00753344	0.00753255
NuF-2	0.154104	0.153615
ADF-E-1 & ADF-N-1	0.990031	1.02952
ADF-E-2 & ADF-N-2	1.0689	0.926528
ADF-W-1 & ADF-S-1	0.990031	1.01034
ADF-W-2 & ADF-S-2	1.0689	1.29312

Table 3.5: Comparison of the group constants and ADFs under the bow condition. E stands for east, N stands for north, W stands for west and S stands for south.

calculation lattice. Once the fuel assembly is bowed inside another fuel assembly lattice (in centimeter range), the conventional diffusion codes might not be suitable here since they are based on the regular space discretization.

In addition to the ADFs, the other factor that the fuel assembly bow can largely influence is the pin power distribution. In Fig. 3.17 and 3.18 the percentage-wise change of pin power fraction is plotted for different state points. It is seen that due to the fuel assembly bow up to 3 rows of the periphery fuel pins are influenced. The most affected rods are then on the upper right and lower left corner. With a displacement of 1mm the maximal change is about 4% whereas this value increases up to 8% when the displacement reaches 2mm. Moreover, by comparing Fig. 3.17 and 3.18 it seems that this pin power fraction (PPF) change doesn't depend on the moderator temperature or the fuel temperature and its dependency on the boron concentration is only limited to a small extent.

Neglecting the temperature and boron concentration influences, the PPF which is applied to the CFX model is then simply generated using the reference state point (TMO 583.15K, TFU 873.15K, BOR 500ppm). Since in Fig. 3.17 and 3.18 the PPF change seems to be roughly linearly correlated to the

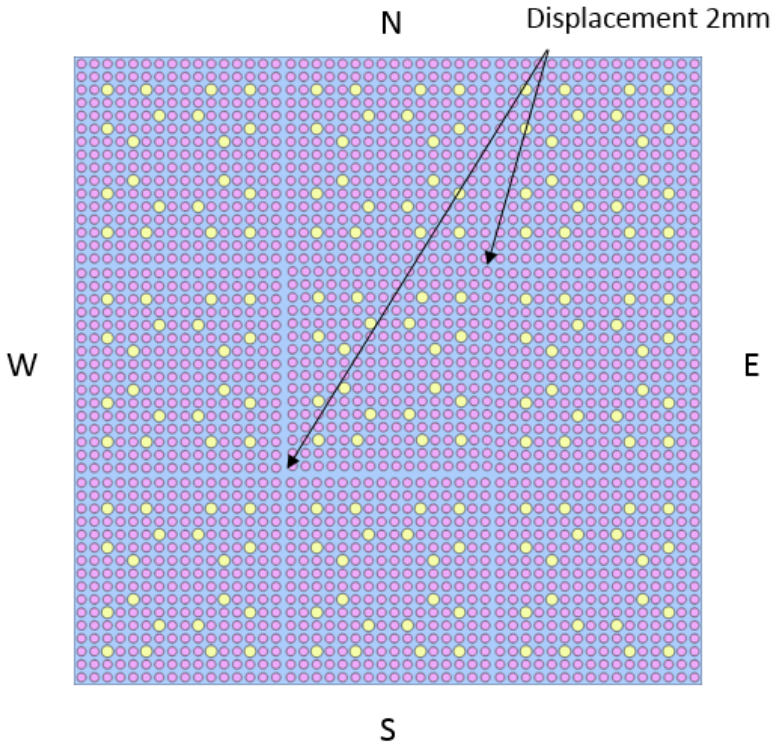

Figure 3.16: Illustration of the fuel assembly bow case in the 3x3 fuel assembly matrix setting.

displacement, a new parameter σ is defined here as in Eq. 3.4 to examine this hypothesis. The more closer the σ value of each fuel pin power to 1 is, the more the hypothesis is valid. Fig. 3.19 gives an impression of the σ value of each fuel pin in the center fuel assembly. The first row of the periphery fuel pins, which are influenced by the FA bow the most, has a σ value between 0.95 to 1.1. The second and the third row of the periphery fuel pins can have higher or lower σ value. But since their PPF changes are smaller compared to the first periphery row, the PPF change can still be considered proportional the the FA displacement. The white color in Fig. 3.19 means the location where the relative power change is zero or relatively negligible ($<$0.3%).

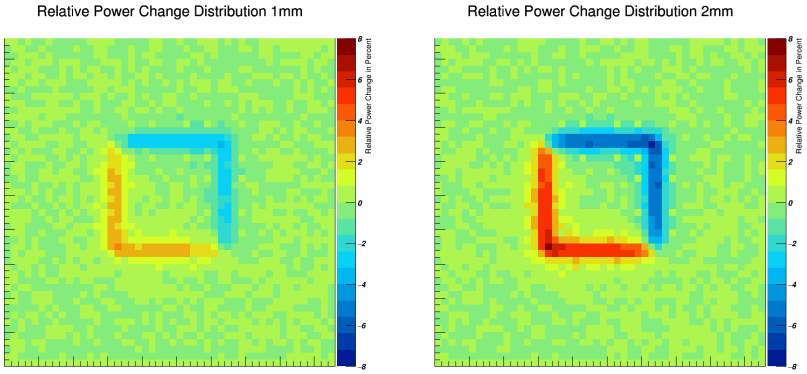

(a) TMO 563.15K, TFU 873.15K, BOR 500ppm

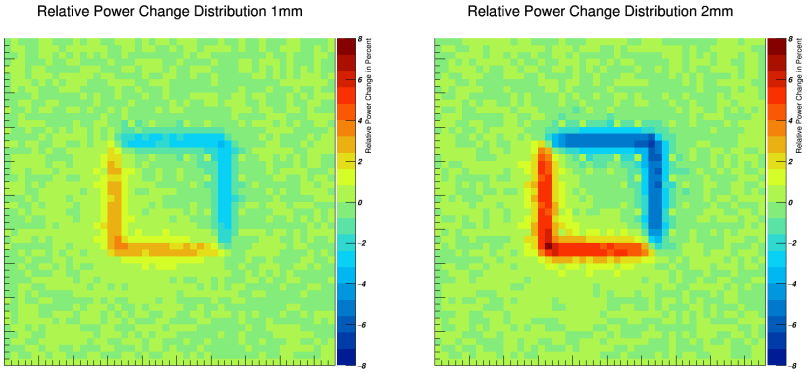

(b) TMO 583.15K, TFU 873.15K, BOR 500ppm

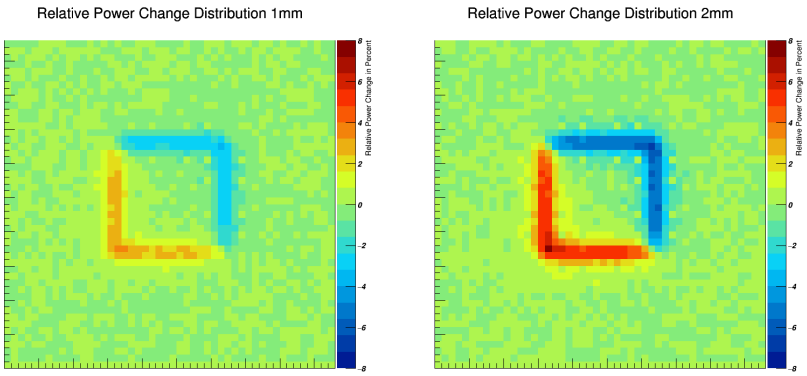

(c) TMO 583.15K, TFU 1500K, BOR 500ppm

Figure 3.17: Pin power fraction change in percentage due to fuel assembly bow with respect to different state points.

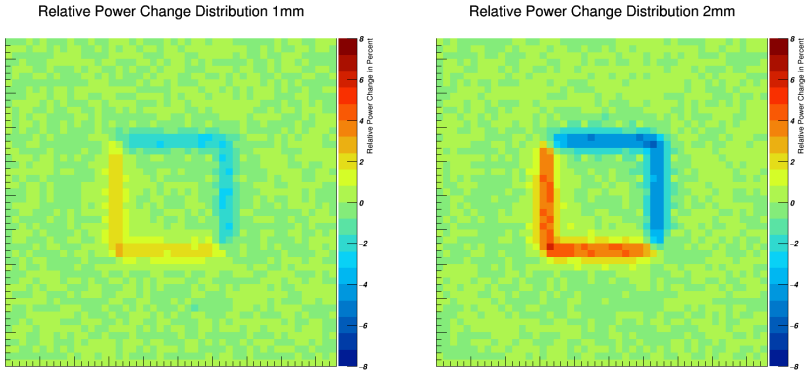

Figure 3.18: Pin power fraction change in percentage due to fuel assembly bow (TMO 583.15K, TFU 873.15K, BOR 2400ppm).

$$\sigma = \frac{\text{Relative power change(2mm)}}{\text{Relative power change(1mm)}} \cdot \frac{\text{1mm}}{\text{2mm}} \tag{3.4}$$

In Fig. 3.20 the relative pin power fraction distribution is shown for the 3x3 FA matrix with the chessboard configuration and Gd-FA in the middle.

3.3 Further cross sections using the lattice code CASMO

In order to investigate the power fraction behavior under different burnups, two cross section libraries (PMAX files) were generated from CASMO calculations using GENPMAX: one normal U-FA with 3.95% U-235 and one MOX-FA with a mixture of U and Pu nuclide vectors. Fig. 3.21 depicts the K_{inf} curve of both FAs with different burnups. Compared to the MOX-FA, U-FA has a higher Kinf within the range of 0-44 MWd/kg which results in a higher reactivity in the U-FA. Tab. 3.6 shows the moderator temperature feedback coefficient and fuel temperature feedback coefficient under the condition of TMO 583.2K, TFU 873.2K and BOR 500ppm for both FAs. It is seen that the MOX fuel assembly has a relative higher MTC (in absolute

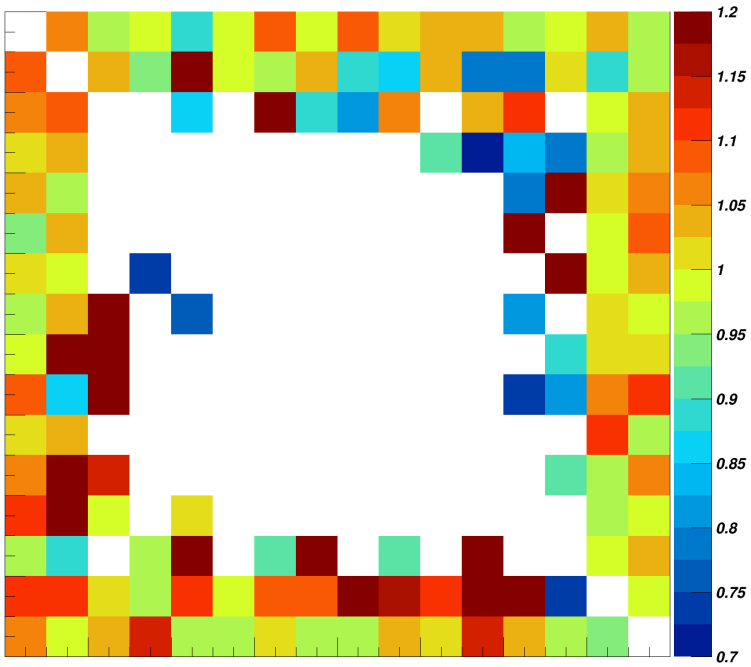

Figure 3.19: The σ value of the middle FA

value) which means the MOX will react stronger to the moderator change.

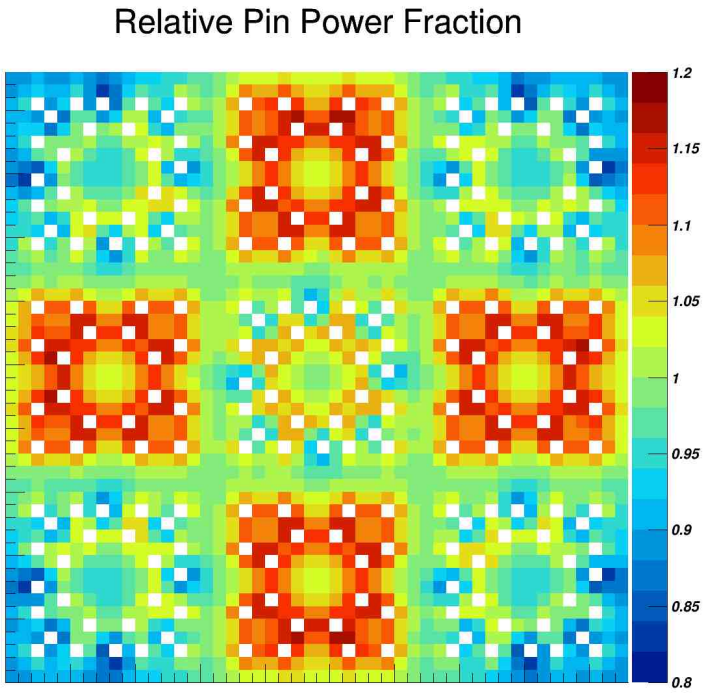

Figure 3.20: Pin power fraction in the 3x3 fuel assembly matrix setting.

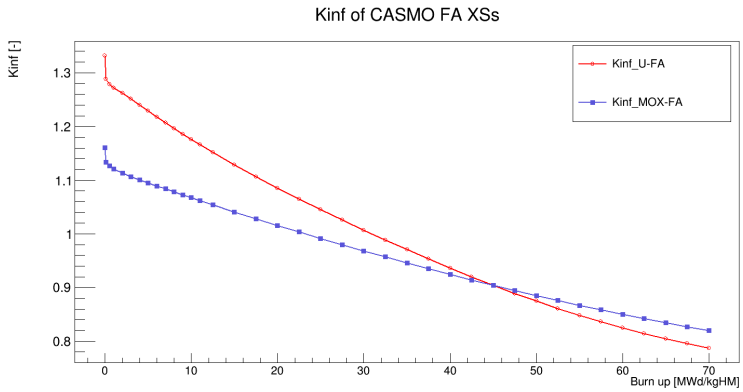

Figure 3.21: The infinite multiplication factor of the U-FA and MOX-FA with respect to burnups

Burnups [MWd/kg]	MTC [pcm/K]	FTC [pcm/K]
U-FA		
0	-13.77	-1.86
10	-18.80	-2.18
30	-25.96	-2.91
MOX-FA		
0	-37.70	-2.95
10	-36.88	-3.07
30	-41.79	-1.57

Table 3.6: The moderator temperature coefficient and fuel temperature coefficient with different Burnups (CASMO XSs).

Chapter 4

Description of the coupling model

4.1 General overview of the coupling procedure

In order to connect the TH CFX model and the neutronics PARCS model a coupling tool is developed. Like the other coupling tools, this coupling tool, which is named PARCFX in this work, is responsible for data extraction, data exchange and data storage. PARCFX is achieved through using the user defined fortran (UDF) model, which is embedded in CFX. The coupling model contains different blocks which are called in different steps in the CFX calculation. More details are explains as follows together with Fig. 4.1.

initial.F:	This block is called during the "User Input" phase which reads the model setting and allocates the data area using the memory management system (MMS) in the CFX-solver.
main.F:	This block is called during the "Start of Coefficient Loop" phase which is the main body of the coupling model. Its functions include extracting the TH data, preparing and initiating the neutronics calculation, feeding the RPF data back to the CFX model.
record.F	This block is called during the "End of Timestep" phase which writes the necessary data into a file which can be post-processed.
heat flux.F	This block is called during the solution phase. In this block the heat flux is read and applied to each fuel pin at different height.

Used for SERPENT XS coupling:

More detailed information about the main.F block is shown in Fig. 4.2. The CFX model has the advantage of having a more discretized structure than the PARCS model in the radial as well as the axial direction. In order to transfer the data to the less discretized neutronics model, the temperatures (the TMO and the temperature of the cladding surface (TWALL)) are averaged over each node in the neutronics model. Additional three modules (the XS-Generator, the TFU-Solver and the Curve-fitting tool in Fig. 4.2) are integrated in this block in order to create the input for the PARCS model and the heat flux data for the CFX model. The XS-Generator generates the cross section data based on the preset BOR, TMO and TFU for all 270 nodes. The TFU-Solver solves the 1-D heat conduction equation based on TWALL and the RPF of each node. And after the neutronics calculation the RPF of each node is put into the Curve-fitting module to obtain a smooth power distribution along the axial direction of each FA. The methodology of each module is explained in more details in the following subsections.

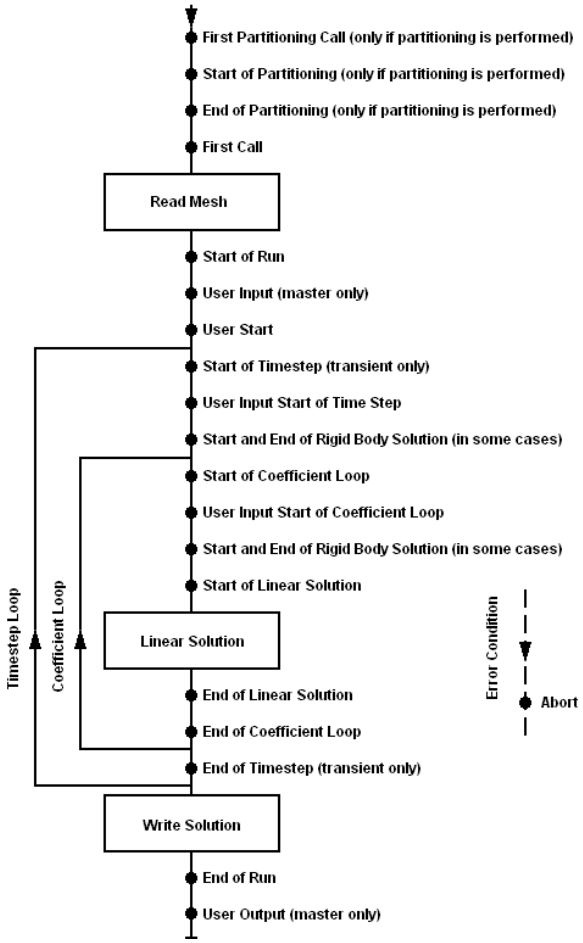

Figure 4.1: Calculation steps of a CFX calculation [ANS19].

Used for CASMO XS coupling:

For coupling with CASMO XS, the coupling routine is slightly changed. Since the macroscopic XS is calculated internally by PARCS, the XS-Generator in the coupling model (shown in 4.2) is replaced by a subroutine which writes the 3D TH and burnup parameters (TMO, TFU, BOR, BU) into a PARCS history format file and feeds it to PARCS.

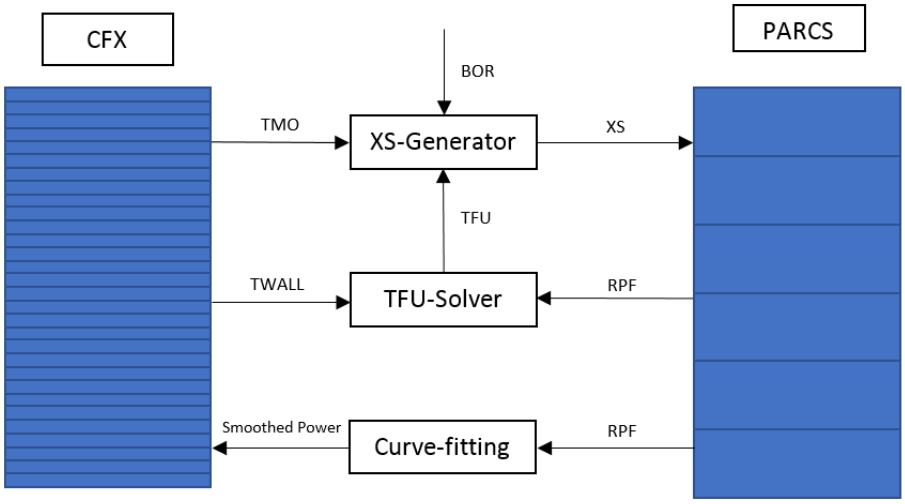

Figure 4.2: An illustration of the coupling model for SERPENT XS datasets.

4.2 The XS-Generator module

The XSs are necessary for solving the diffusion equation. Typically it can be interpreted as a function of TFU, TMO, density of the coolant (DCO) and control rod insertion shown in Eq. 4.1 [DXS12]. The equation basically suggests that the macroscopic XS has a linear correlation with the square root of TFU, TMO, percentage of the control rod insertion and BOR while a non linear correlation with DCO. A more detailed evaluation of the influence are shown in section 3.2.1.

$$\begin{aligned}\Sigma(\alpha, TFU, TMO, DCO, BOR) =& \Sigma^{r} + \alpha\partial\Sigma^{cr} + \frac{\partial\Sigma}{\partial\sqrt{TFU}}\partial\sqrt{TFU} \\ &+ \frac{\partial\Sigma}{\partial TMO}\partial TMO + \frac{\partial\Sigma}{\partial BOR}\partial BOR \\ &+ \frac{\partial\Sigma}{\partial DCO}\partial DCO + + \frac{\partial^{2}\Sigma}{\partial DCO^{2}}(\partial DCO)^{2}\end{aligned} \tag{4.1}$$

where

$$\begin{aligned}
\Sigma^r &= \text{the macroscopic XS at the reference state} \\
\alpha &= \text{percentage of the control rod insertion} \\
TFU &= \omega T_F^{CL} + (1-\omega) T_F^{PS} \\
\omega &= \text{weight factor between 0 and 1} \\
T_F^{CL} &= \text{fuel temperature at the center-line} \\
T_F^{PS} &= \text{fuel temperature at the pellet surface}
\end{aligned}$$

Since in the SERPENT calculation the temperature induced density change is considered for the moderator and the control rod is not modeled, only TFU, BOR and TMO are the parameters that can influence the XS. The desired XS is obtained through linear interpolation or extrapolation between a set of state points (shown in Fig. 4.3).

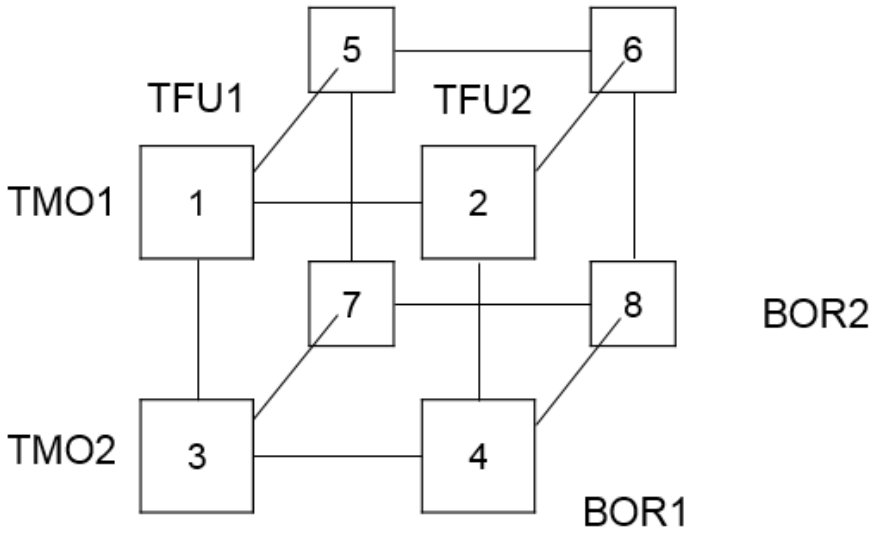

Figure 4.3: An illustration of the data structure of the XS set.

4.3 The TFU solver

4.3.1 An introduction to the TFU solver

Since CFX cannot model the solid part with the mesh deformation method. A TFU solver is integrated inside the coupling model in order to calculate the correct nodal averaged fuel temperature. The TFU solver solves the 1-D heat conduction equation based on the state of the nodal relative power fraction and the temperature of the cladding outer surface. We assume that the heat conduction along the axial direction is negligible since the r/L is extremely small, the heat is generated inside the fuel pellet evenly and the temperature distribution has no dependence in the azimuthal direction. With these assumptions, the equation in cylinderal coordinate is written as:

$$C_V(T)\frac{\partial T}{\partial t} = \frac{1}{r}\frac{\partial}{\partial r}\big[\lambda(T) r \frac{\partial T}{\partial r}\big] + \dot{q}''' \tag{4.2}$$

where $C_V(T)$ is the volumetric heat capacity, $\lambda(T)$ the thermal conductivity of the material and both of them are dependent on temperature. $\dot{q}'''$ is the volumetric heat generation rate.

In steady-state case, the time-dependent term is neglected and Eq. 4.2 is simplified as:

$$\frac{1}{r}\frac{\partial}{\partial r}\big[\lambda(T) r \frac{\partial T}{\partial r}\big] = -\dot{q}''' \tag{4.3}$$

$$\Rightarrow \int_r \big[\lambda(T) r \frac{\partial T}{\partial r}\big]\partial r = -\int_r \dot{q}''' r \partial r \tag{4.4}$$

$$\Rightarrow \lambda(T) r \frac{\partial T}{\partial r} = -\frac{\dot{q}''' r^2}{2} + C \tag{4.5}$$

where C is determined separately by applying different boundary conditions in the fuel zone where $\dot{q}'''$ is not zero and in the non-fuel zone where $\dot{q}'''$ is zero.

In the fuel zone ($\dot{q}'''$ is not zero):

$$-\lambda(T)\frac{\partial T}{\partial r}\bigg|_{r=0} = 0 \Rightarrow C_{fuel} = 0 \tag{4.6}$$

In the none-fuel zone ($\dot{q}'''$ is zero):

$$-\lambda(T)\frac{\partial T}{\partial r}\bigg|_{r=r_{fo}} = \dot{q}'''\frac{\pi r_{fo}^2}{2\pi r_{fo}} \tag{4.7}$$

$$\Rightarrow C_{non-fuel} = \frac{\dot{q}'''r_{fo}^2}{2} \tag{4.8}$$

where r_{fo} is the radius of the fuel pellet.

Then Eq. 1.3 is rewritten as:

$$\text{fuel zone:} \quad \frac{\partial T}{\partial r} = \frac{\dot{q}'''r}{2\lambda(T)} \tag{4.9}$$

$$\text{none-fuel zone:} \quad \frac{\partial T}{\partial r} = \frac{\dot{q}'''r_{fo}^2}{2\lambda(T)r} \tag{4.10}$$

The TFU-solver in the coupling model solves the above mentioned two differential equations 4.9 4.10 based on the 4^{th} order Runge-Kutta method illustrated as follows:

$$\dot{T} = f(r,T), \quad T(r_0) = T_{co}$$
$$T_{n+1} = T_n + \frac{1}{6}(k_1 + 2k_2 + 2k_3 + k_4)$$
$$r_{n+1} = r_n + \partial r$$

where

$$
\begin{aligned}
k_1 &= \partial r f(r_n, T_n) \\
k_2 &= \partial r f(r_n + \frac{\partial r}{2}, T_n + \frac{k_1}{2}) \\
k_3 &= \partial r f(r_n + \frac{\partial r}{2}, T_n + \frac{k_2}{2}) \\
k_4 &= \partial r f(r_n + \partial r, T_n + k_3) \\
&\partial r : \text{the step size} \\
&f(r, T) : \text{the differential equations 4.9 4.10} \\
&T_{co} : \text{temperature of the cladding outer surface}
\end{aligned}
$$

The material properties, the thermal conductivity $\lambda(T)$, are taken from FRAPCON [GLRP15a, LGP15]. The thermal conductivity of UO_2 at 95% of the theoretical density is calculated as:

$$\lambda_{f95} = [A + a \cdot gad + BT + f(Bu) + (1 - 0.9 \exp^{-0.04Bu}) g(Bu) h(T)]^{-1} + \frac{E}{T^2} e^{-F/T} \tag{4.11}$$

where

$$
\begin{aligned}
A &= 0.0452\ mK/W \\
B &= 2.46E-4\ m/W \\
E &= 3.5E9\ WK/m \\
F &= 16361\ K \\
a &= 1.1599 \\
gad &= \text{gadolinia weight fraction} \\
Bu &= \text{burnup, GWd/MTU} \\
f(Bu) &= \text{effect of fission products in crystal matrix} \\
&= 0.00187Bu
\end{aligned}
$$

$$
\begin{aligned}
g(Bu) &= \text{effect of irradiation defects} \\
&= 0.038 Bu^{0.28} \\
h(T) &= \text{temperature dependence of annealing on irradiation defects} \\
&= \frac{1}{1 + 396 \exp(-Q/T)} \\
Q &= 6380\ K
\end{aligned}
$$

Assuming that the FA is a fresh one and contains only UO_2 in the fuel pellet at 95% of the theoretical density, the thermal conductivity is plotted in Fig. 4.4 with different temperatures.

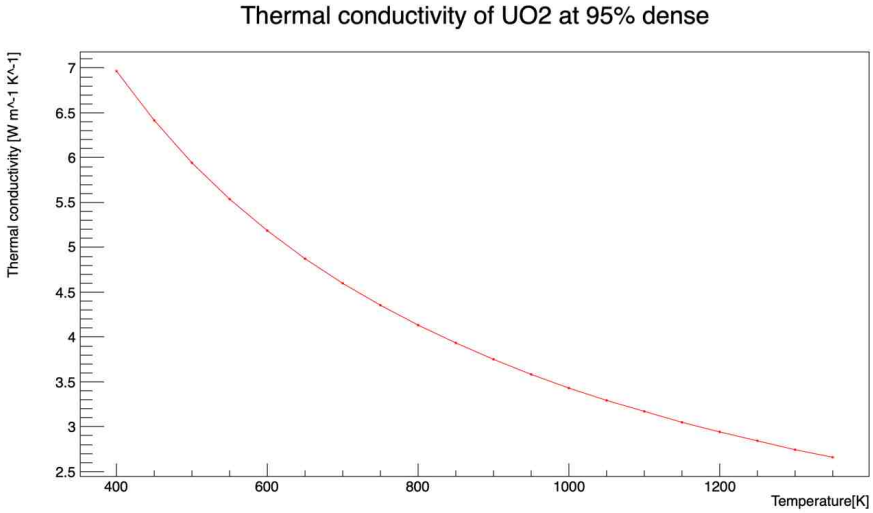

Figure 4.4: The thermal conductivity of UO_2 at 95% dense in range of 400-1300K.

The none-fuel zone consists of the helium gas gap and the cladding material. Here we assume that the heat is conducted only through conduction. The thermal conductivity for the helium gas is calculated in Eq. 4.12 and for zircaloy as Eq. 4.13 [LGP15].

$$\lambda_{He} = 2.531 * 10^{-3} T^{0.7146} \tag{4.12}$$

$$\lambda_c = 7.51 + 2.09 * 10^{-2}T - 1.45 * 10^{-5}T^2 + 7.67 * 10^{-9}T^3 \tag{4.13}$$

And the thermal conductivity for the helium gas gap and zircaloy are plotted in Fig. 4.5 and 4.6. While the thermal conductivity for UO_2 decreases with an increasing temperature, the thermal conductivity for the helium gas as well as for zircaloy increases(in range of 400-1300K).

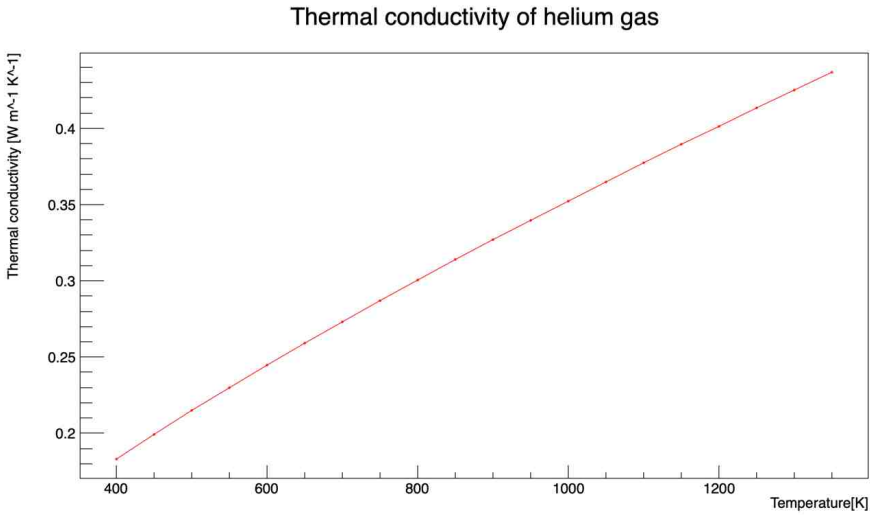

Figure 4.5: The thermal conductivity of helium gas in range 400-1300K.

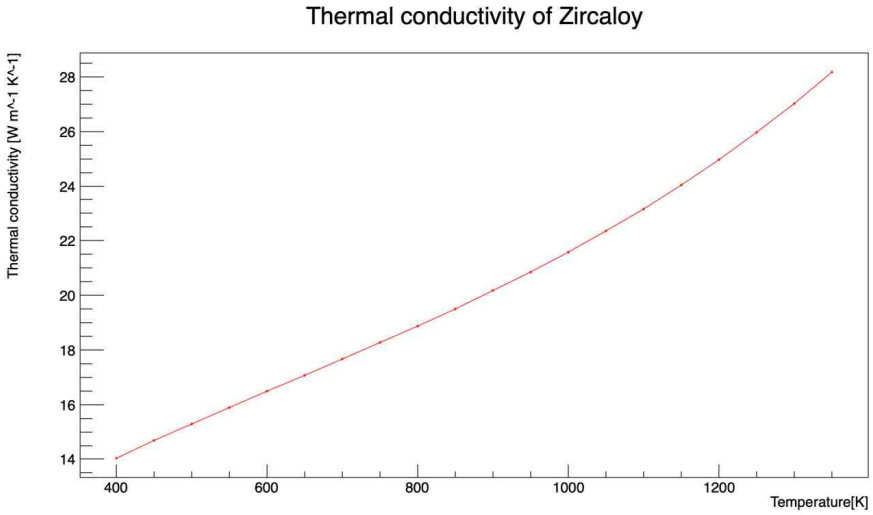

Figure 4.6: The thermal conductivity of zircaloy in range 400-1300K.

As already illustrated in Eq. 4.1, the effective Doppler fuel temperature (TFU) is calculated in PARCS by default as a linear interpolation between the fuel center-line temperature and the fuel pellet surface temperature. The default value for ω is 0.3. One can also change the mode in PARCS to calculate the volumetric averaged fuel temperature. On the other hand, other reactor simulator, such as SIMULATE-3, uses different subroutines to calculate TFU shown in Eq. 4.14 [BHD+13].

$$TFU = TMO + aQ + bQ^2 \tag{4.14}$$

where

Q = the nodal power density

a = the linear coefficient of fuel temperature with respect to Q

b = the quadratic coefficient of fuel temperature with respect to Q

In this work the volumetric averaged fuel temperature is used and it is solved by the following equation 4.15.

$$TFU = \frac{\sum TFU^m \cdot V^m}{\sum V^m} \tag{4.15}$$

where TFU^m is the fuel temperature of node m and V^m is the volume of node m.

In the transient calculation we simply consider the fuel pellet as a whole with a temperature of T, and Eq. 4.2 is rewritten as:

$$\int_V C_V(T)\rho(T)\frac{\partial T}{\partial t}dV = \overbrace{\int_S \lambda(T)\nabla T dS}^{1} + \overbrace{\int_V \dot{q}''' dV}^{2} \tag{4.16}$$

where the first term on the right hand side (RHS) means the total heat

lost through area S and the second term on the RHS means the total heat generation over the volume V. In literature [SKSB15] it is mentioned that the fuel pellet temperature responds normally several seconds later to power burst due to its large heat capacity and density. Here is one example.

We assume that the first term in Eq. 4.16 is the same and the temperature change is due to a power burst of 10%. The C_V is taken from FINIX and FRAPTRAN [Iko13, LGP15, GLCP16] which are two transient codes for calculating fuel behavior. The specific heat capacity is given as:

$$C_V = \frac{K_1\theta^2 \exp(\theta/T)}{T^2[\exp(\theta/T)-1]^2} + K_2 T + \frac{Y K_3 E_D}{2RT^2}\exp(-E_D/RT) \tag{4.17}$$

where

$$\begin{aligned} T &= \text{temperature(K)} \\ Y &= \text{oxygen-to-metal ratio} \\ R &= 8.3143\ \text{(J/mol*K)} \\ \theta &= 535.285\ \text{(K) for } \mathrm{UO_2} \\ E_D &= 1.577\text{E5}\ \text{(J/mol)} \\ K_1 &= 296.7 \\ K_2 &= 2.43\text{E-2} \\ K_3 &= 8.745\text{E7} \end{aligned}$$

Assuming the oxygen-to-metal ratio is 2, the specific heat capacity of UO_2 is then shown in Fig. 4.7. With an increasing temperature the specific heat capacity increases, which means if the temperature gets higher, the material is more resistant to temperature increase in case of power burst.

Assuming the volumetric power generation rate is 3.34E8 W/m^3 which corresponds to the averaged volumetric heat generation rate of a 20 MW FA, and the density of the fuel pellet is 10.2 g/cm^3, the maximal temperature

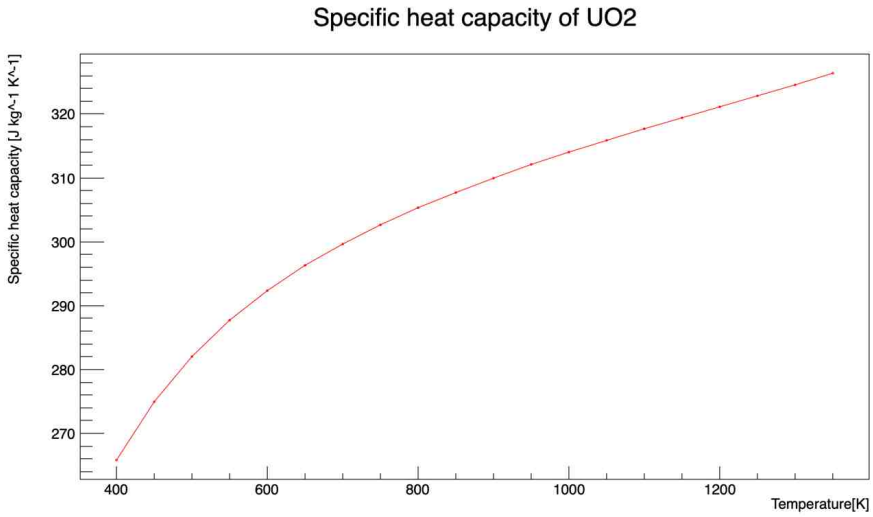

Figure 4.7: The specific heat capacity of UO_2 in range 400-1300K.

increase due to a 1 Hz oscillating 10% power burst is listed in Tab. 4.1 with respect to different reference temperatures. Given that typically the MTC is in the magnitude of several dozens of pcm/K (negative value) whereas the fuel temperature coefficient is about several pcm/K (negative value), the influence of the fuel temperature change is much smaller than the moderator temperature change. Due to this effect the fuel temperature is therefore considered constant in the transient calculation.

Temperature (K)	∂T (K)
600	3.57
700	3.48
800	3.41
900	3.36
1000	3.32
1100	3.28
1200	3.25
1300	3.21

Table 4.1: Temperature increase of the UO_2 pellet due to a 10% power burst at different reference temperatures.

Reference volumetric heat rate [W/s]	3.34E8
Power factors	0.2, 0.5, 1.0, 1.5, 2.0

Table 4.2: Power factor settings for TFU-solver & TRACE comparison.

4.3.2 A quick comparison with the TRACE solver

Steady state calculations are made here to examine the applicability of the TFU solver by comparing the results from the TFU solver and TRACE with the same boundary conditions. In the radial direction, the model is divided into 10 annular regions for the fuel pellet, one region for the gas gap and 5 layers for the cladding material. The fuel assembly is put under different volumetric heat generation rates so that the solver is examined under different power regimes. Detailed settings can be found in Tab. 4.2.

As is shown in Fig. 4.8 the results of the TFU-solver agree very well with the TRACE results for all power factors. The maximal deviation of the fuel center-line temperature is about 2.3K for the case with the power factor of 1.5 while the temperature deviation at fuel center-line for the other cases are well held within 1.3K.

4.4 Curve-fitting module

Since the PARCS model is a less discretized model, the RPF data obtained from the neutronics calculation is then the averaged value over each node. Normally with a reasonable number of nodes in the axial direction, these values can be directly applied to some 1-D TH code with the same number of axial layers. But tools like CFX, which offers the possibility to model the fuel assembly at the pin level, require a more smoother power distribution feedback. In Fig. 4.9 one example of the axial power distribution of a single FA model from PARCS can be seen. While the power profile in the middle is more or less flat, large gradient can be observed at the top and bottom nodes. Therefore this module is developed to transform the nodal RPF into

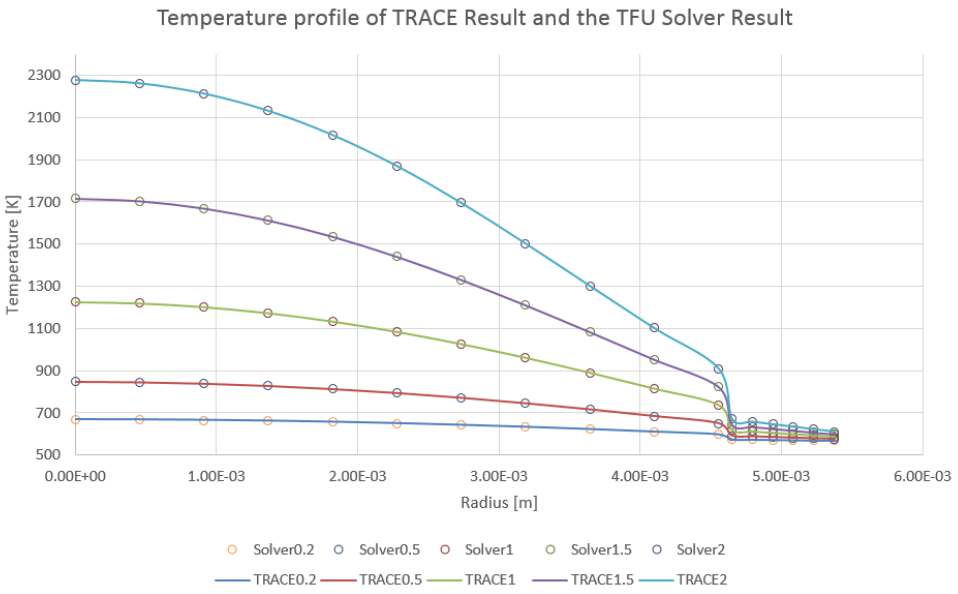

Figure 4.8: Comparison of the TFU-solver result with TRACE result with different power factors. The TFU-solver results are drawn with circles and the TRACE results are drawn with lines.

a 5^{th} order polynomial of the axial height z.

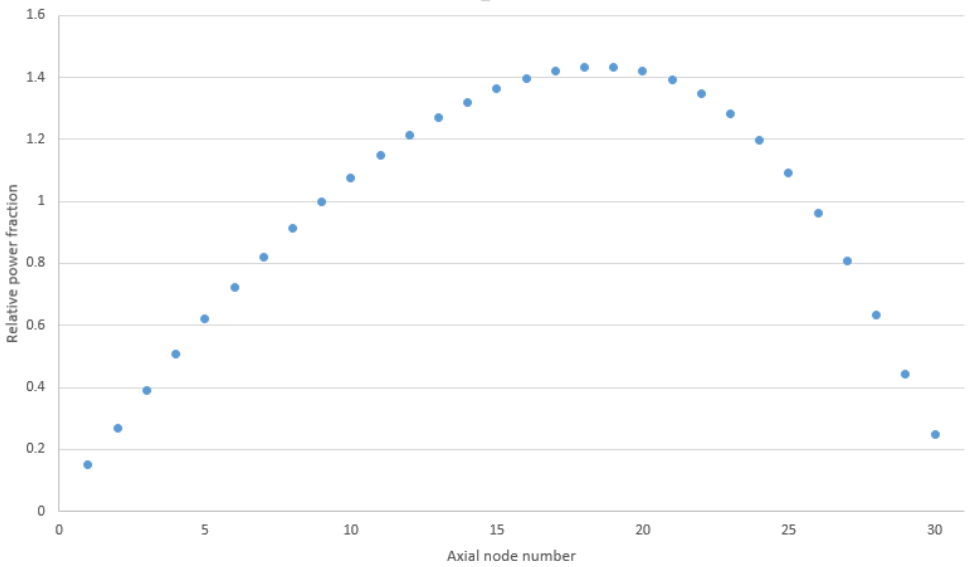

Figure 4.9: One example of the axial power distribution from PARCS.

The curve-fitting module is written based on the least squares methods which is achieved by minimize the error sum of squares, err, given by Eq. 4.18.

$$err = \sum_{i=1}^{n} \big(RPF_i - f_i(z_i)\big)^2 \tag{4.18}$$

where RPF_i is the data point value obtained from the PARCS calculation, $f_i(z_i)$ is the predicted value with a specific parameter z_i, which in our case is the axial height. Since we assume that the RPF has a shape of a 5^{th} order of polynomial, $f_i(z_i)$ is illustrated in Eq. 4.19.

$$f_i(z_i) = a_0 + a_1 z_i^1 + a_2 z_i^2 + a_3 z_i^3 + a_4 z_i^4 + a_5 z_i^5 \tag{4.19}$$

The goal is to determine the polynomial parameters $\{a_0, a_1, ..., a_5\}$ in order to minimize the error, err, whose derivative over each parameter should equal to zero.

$$\begin{aligned}
\frac{\partial err}{\partial a_0} &= -2 \sum_{i}^{n} \big(y_i - f_i(z_i)\big) = 0 \\
\frac{\partial err}{\partial a_1} &= -2 \sum_{i}^{n} \big(y_i - f_i(z_i)\big) z_i = 0 \\
\frac{\partial err}{\partial a_2} &= -2 \sum_{i}^{n} \big(y_i - f_i(z_i)\big) z_i^2 = 0 \\
\frac{\partial err}{\partial a_3} &= -2 \sum_{i}^{n} \big(y_i - f_i(z_i)\big) z_i^3 = 0 \\
\frac{\partial err}{\partial a_4} &= -2 \sum_{i}^{n} \big(y_i - f_i(z_i)\big) z_i^4 = 0 \\
\frac{\partial err}{\partial a_5} &= -2 \sum_{i}^{n} \big(y_i - f_i(z_i)\big) z_i^5 = 0
\end{aligned}$$

This turns into a set of linear equations with the form of $Ax = B$ which can be easily solved by method like Gaussian elimination.

$$A = \begin{bmatrix} \sum_i^n a_0 & \sum_i^n a_1 z_i^1 & \sum_i^n a_2 z_i^2 & \sum_i^n a_3 z_i^3 & \sum_i^n a_4 z_i^4 & \sum_i^n a_5 z_i^5 \\ \sum_i^n a_0 z_i^1 & \sum_i^n a_1 z_i^2 & \sum_i^n a_2 z_i^3 & \sum_i^n a_3 z_i^4 & \sum_i^n a_4 z_i^5 & \sum_i^n a_5 z_i^6 \\ \sum_i^n a_0 z_i^2 & \sum_i^n a_1 z_i^3 & \sum_i^n a_2 z_i^4 & \sum_i^n a_3 z_i^5 & \sum_i^n a_4 z_i^6 & \sum_i^n a_5 z_i^7 \\ \sum_i^n a_0 z_i^3 & \sum_i^n a_1 z_i^4 & \sum_i^n a_2 z_i^5 & \sum_i^n a_3 z_i^6 & \sum_i^n a_4 z_i^7 & \sum_i^n a_5 z_i^8 \\ \sum_i^n a_0 z_i^4 & \sum_i^n a_1 z_i^5 & \sum_i^n a_2 z_i^6 & \sum_i^n a_3 z_i^7 & \sum_i^n a_4 z_i^8 & \sum_i^n a_5 z_i^9 \\ \sum_i^n a_0 z_i^5 & \sum_i^n a_1 z_i^6 & \sum_i^n a_2 z_i^7 & \sum_i^n a_3 z_i^8 & \sum_i^n a_4 z_i^9 & \sum_i^n a_5 z_i^{10} \end{bmatrix},$$

$$x = \begin{pmatrix} a_0 \\ a_1 \\ a_2 \\ a_3 \\ a_4 \\ a_5 \end{pmatrix}$$

and

$$B = \begin{pmatrix} \sum_i^n y_i \\ \sum_i^n z_i^1 y_i \\ \sum_i^n z_i^2 y_i \\ \sum_i^n z_i^3 y_i \\ \sum_i^n z_i^4 y_i \\ \sum_i^n z_i^5 y_i \end{pmatrix}$$

A quick implementation of the curve-fitting module is shown in Fig. 4.10. It can be seen that the power profile prediction from the curve-fitting module agrees well with the PARCS result.

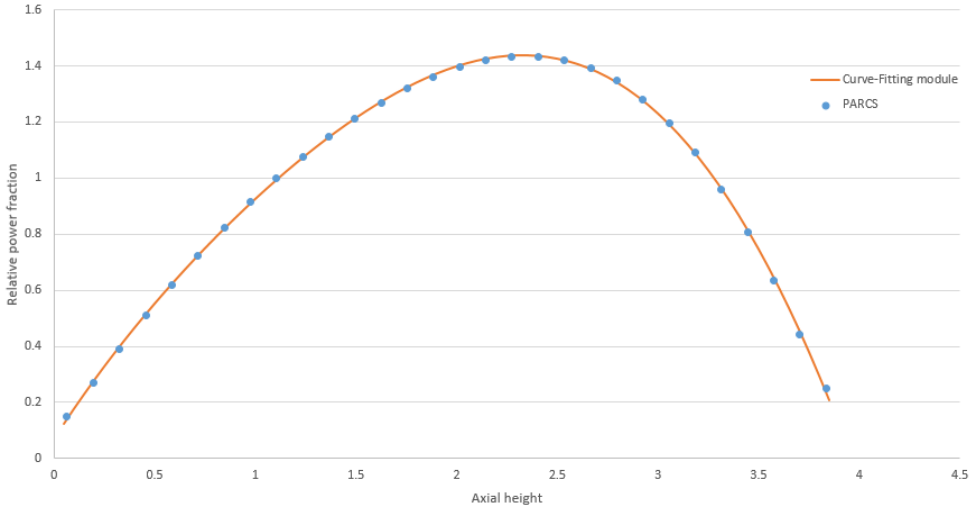

Figure 4.10: Comparison of the axial power distribution from PARCS and the result from the curve-fitting module.

Chapter 5

Single FA simulation

5.1 Definition of the test scenarios

Based on the current coupling methodology, the following scenarios are defined:

- Steady-state calculation
- Transient calculations
  - Tin transient cases: with oscillating inlet moderator temperature
  - Vin transient cases: with oscillating inlet moderator velocity
  - Rod movement cases: with oscillating fuel rod based on the mesh deformation method

5.2 Steady-State Calculation

The simulations are conducted firstly with a single fuel assembly model to have a general overview of the relative power fraction changes due to flow or structure oscillations. The power is kept constant at 20MW for the single fuel assembly model. Therefore all the RPF evaluations exclude the effect

brought by the total power change of the fuel assembly.

Fig. 5.1 shows the axial moderator temperature distribution. The maximal moderator temperature is located at the top of the model (30th layer) with a value of 597.2K. Fig. 5.2 illustrates the axial fuel temperature distribution. The nodal averaged fuel temperature is much more influenced by the axial power distribution (shown in Fig. 5.3). The maximal fuel temperature as well as the maximal relative power fraction are located on the 18th layer (TFU_{max}=1010K and RPF_{max}=1.45) whereas in the classic analysis with the assumption of having homogeneous temperature distribution in the axial direction, the axial power distribution has a sine shape with its maximum directly in the middle. With the feedback of the moderator temperature and the fuel temperature the power peak is shifted upwards. The direction of the shift is related to the value of boron concentration. A high boron concentration value results in a positive MTC (shown in Table 3.3) which could compensate the negative FTC. And with a higher moderator temperature in the upper part, the reactivity is also larger than the bottom part which causes the peak to shift upwards. But this behavior doesn't mean that the power peak should be located at the top layer where the TMO is the highest since the leakage of that layer is much larger than the other layers. For boron concentration which is low (500ppm for example), the peak is shifted downwards.

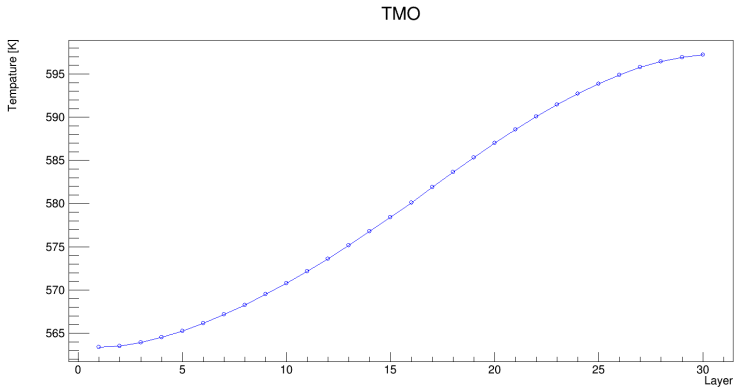

Figure 5.1: The axial TMO distribution of the steady state calculation with the single fuel assembly model.

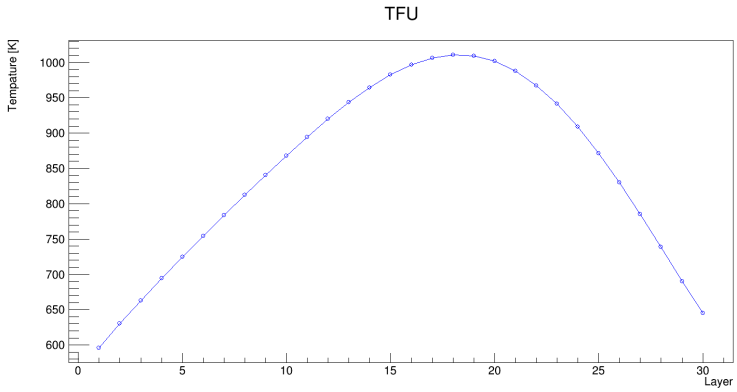

Figure 5.2: The axial TFU distribution of the steady state calculation with the single fuel assembly model.

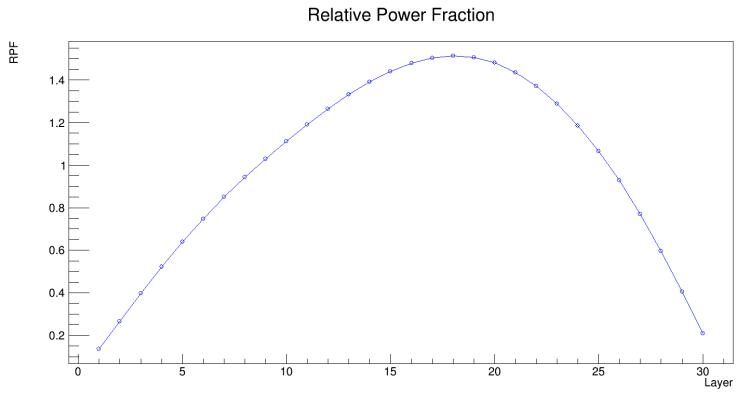

Figure 5.3: The axial RPF distribution of the steady state calculation with the single fuel assembly model.

	a	f
Tin	2[K]	5[Hz]
	2[K]	1[Hz]
	5[K]	5[Hz]
	5[K]	1[Hz]
Vin	0.2[m/s]	5[Hz]
	0.2[m/s]	1[Hz]
	0.5[m/s]	5[Hz]
	0.5[m/s]	1[Hz]

Table 5.1: Cases under oscillating moderator inlet boundary condition with single fuel assembly model.

5.2.1 Transient Calculations

This section presents the results of applying different oscillating boundary conditions on the model. A sine form time dependent disturance is applied to the moderator inlet temperature and moderator inlet velocity (see Eq. 5.1). To investigate the system's response to different oscillation mode, the cases are divided into two categories: varying the amplitude of the oscillation and varying the frequency of the oscillation. A list of the cases is shown in Tab. 5.1.

$$\delta = a \cdot sin(t \cdot f \cdot 2\pi) \tag{5.1}$$

where δ is the time dependent disturbance, a is the amplitude of the oscillation, t is time and f is the frequency of the oscillation.

Then simulations are done with the assumption that the fuel rods are under vibration condition with unknown reasons. The directions of the vibration is in one case in x direction and in the other case in x- & y-direction (diagonal direction). The displacement also follows a sine function with the amplitude of 1mm and the frequency of 1Hz. The fuel rod vibration is simulated using the mesh deformation method which changes the flow area accordingly. Four cases are set for the rod vibration case simulating different locations of the

Case1-single rod	x-directional displacement
Case2-single rod	x- & y-directional displacement
Case3-all rods	x-directional displacement
Case4-all rods	x- & y-directional displacement

Table 5.2: Cases for oscillating moderator inlet boundary condition with single fuel assembly model.

disturbance: single-rod vibration (center four pins) and all-rod vibration (settings shown in Tab. 5.2).

5.3 Tin investigations

Fig. 5.4 and 5.5 show the nodal averaged moderator temperature at different axial layers due to the Tin oscillation. Several things can be noticed here: the amplitude of the temperature becomes smaller with an increasing height. For example, an amplitude of 5K on layer 1 becomes 3.5K on layer 30 corresponding to the a=5K and f=1Hz case. A transport effect can be easily seen in the temperature field. Besides, the frequency of the oscillation can also influence the amplitude change. The lower the frequency is, the bigger the amplitude changes(defining this change as the difference of the oscillation amplitude between layer 30 and layer 1). For instance, comparing both cases with an amplitude of 5K at the entrance, the change in amplitude is 1.5K with an oscillation frequency of 1Hz and 4K with an oscillation frequency of 5Hz.

The results of the relative power fraction on the other hand also show a transport effect along the axial direction (shown in figure 5.6 and 5.7). With an increasing moderator temperature, a positive reactivity is introduced at that layer which results in an increasing RPF at that layer. On the contrary the RPF at the other layers are reduced so that the averaged RPF equals to 1. Fig. 5.8 shows a heterogeneous distribution of the oscillation amplitude along the axial direction with a maximum value of about 8% absolute value

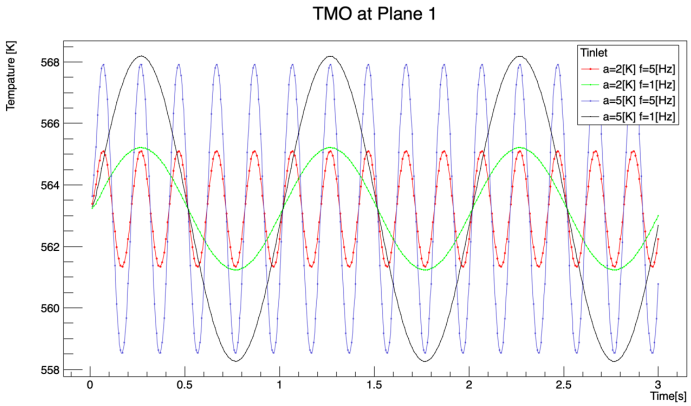

(a)

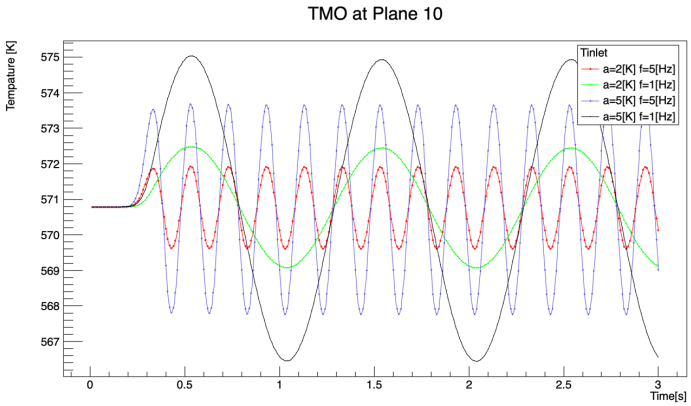

(b)

Figure 5.4: TMO at lower layers due to Tin oscillation.

at around the 7th and 23rd layer (a=5K, f=1Hz). It is also seen that the percentage-wise oscillation amplitude curve has its maximum at the bottom layer and decreases firstly to the middle layer and then increases further to the top layer. It seems the inlet temperature oscillation has minimum effect on the middle layer. Besides, higher frequency of inlet temperature oscillation can bring very limited effects in the RPF field.

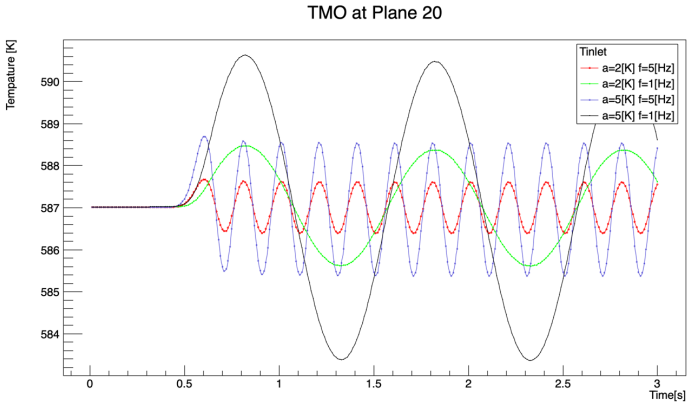

(a)

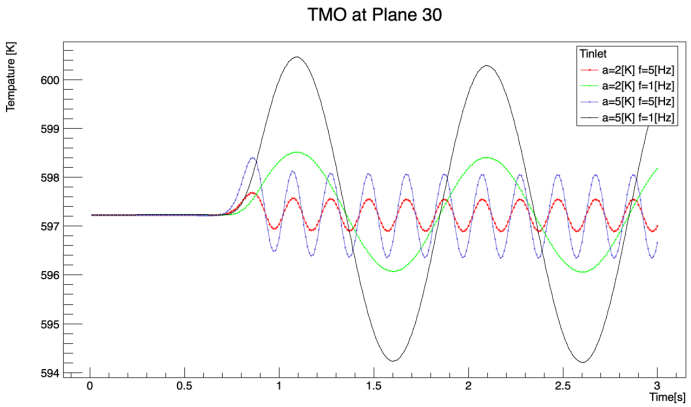

(b)

Figure 5.5: TMO at upper layers due to Tin oscillation.

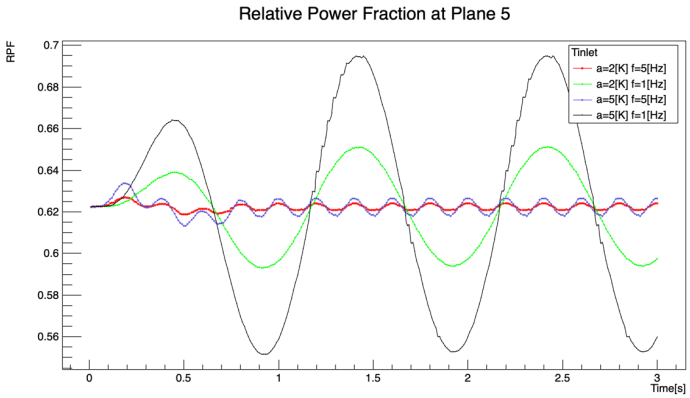

(a)

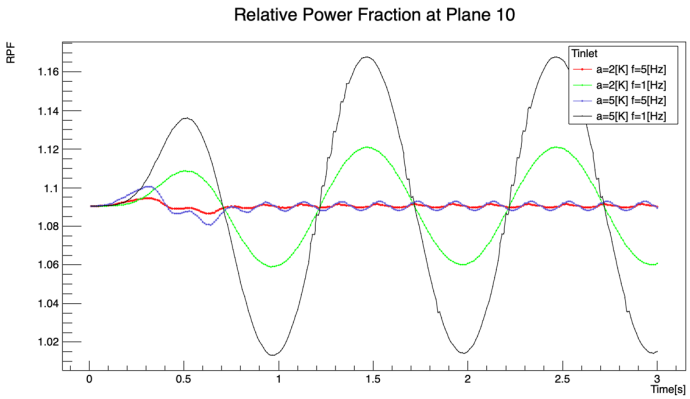

(b)

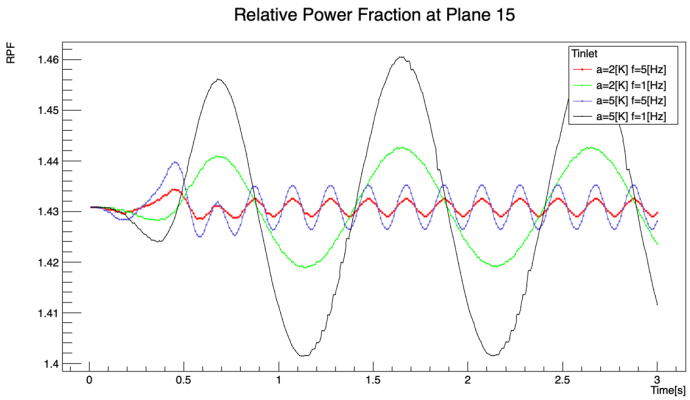

(c)

Figure 5.6: RPF at lower layers due to Tin oscillation.

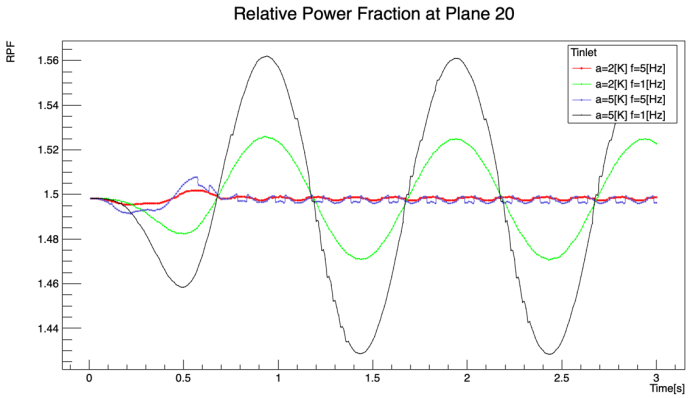

(a)

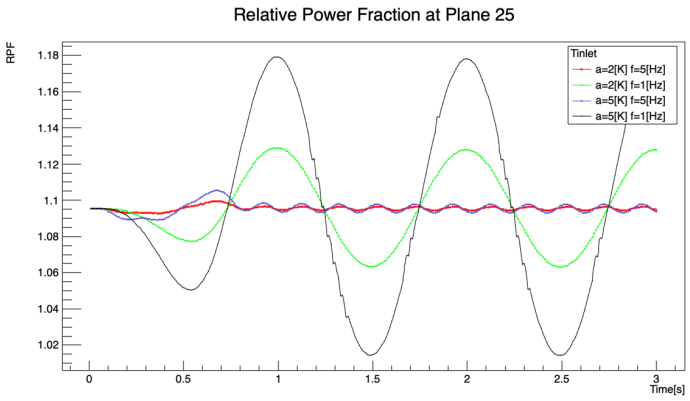

(b)

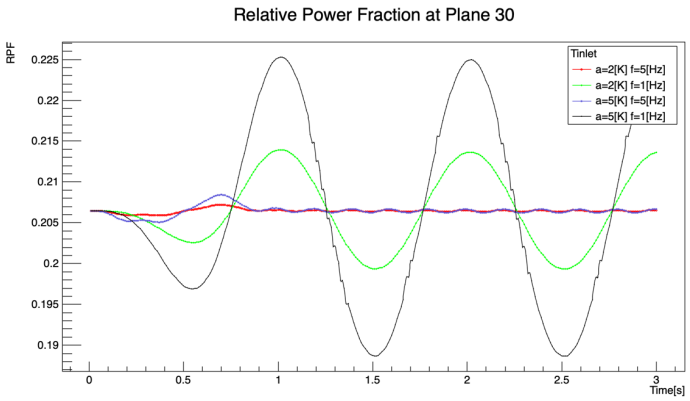

(c)

Figure 5.7: RPF at upper layers due to Tin oscillation.

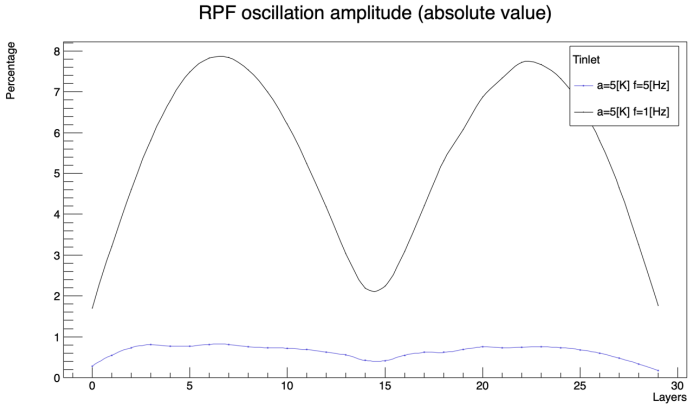

(a)

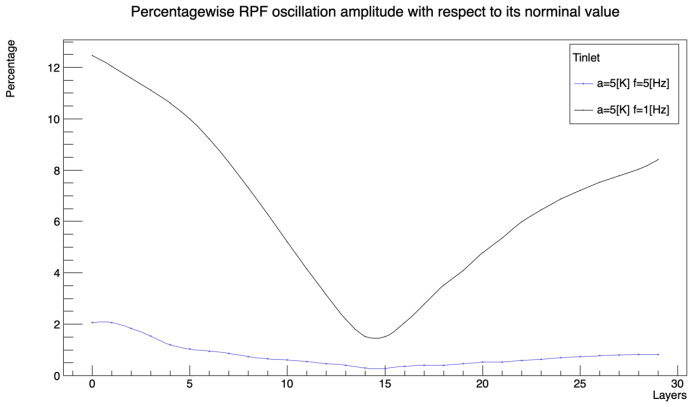

(b)

Figure 5.8: RPF oscillation amplitude along the axial direction.

5.4 Vin investigations

Fig. 5.9 and 5.10 show the nodal averaged moderator temperature at different axial layers due to the Vin oscillation. With an increasing inlet velocity, the mass flow rate increases and TMO decreases globally. Same as the Tin cases, the frequency of the oscillation can influence the amplitude change. The lower the frequency is, the bigger the amplitude changes(defining this change as the difference of the oscillation amplitude between layer 30 and layer 1). Furthermore, given a=0.5m/s and f=1Hz which corresponds to an oscillation about 11kg/s of coolant mass flow rate, the outcome of the temperature change is relatively small (about 1K at plane 30 and 0.6K at plane 10).

The results on the neutronics side on the other hand show that the inlet mass flow rate oscillation has a global effect along the axial direction (shown in figure 5.6 and 5.7). With an increasing coolant mass flow rate, the RPF at the lower layers increases whereas the RPF at the upper layers decreases. It seems that the moderator temperature changes more at the top than at the bottom and an larger positive reactivity is introduced at the lower layers which results in an increasing RPF at the lower layers. The amplitude of the RPF oscillation has a heterogeneous distribution along the axial direction with a maximum value of about 1.2% absolute value at around the 7th and 23rd layer (a=0.5m/s, f=1Hz). Fig. 5.13 shows the oscillation amplitude along the axial direction. It is seen that the percentage-wise oscillation amplitude curve has its maximum at the bottom layer and decreases first to the middle layer and then increases further to the top layer. It seems the inlet velocity oscillation has minimum effect on the middle layer. Besides, the higher the frequency of inlet velocity oscillation is, the smaller the RPF oscillates.

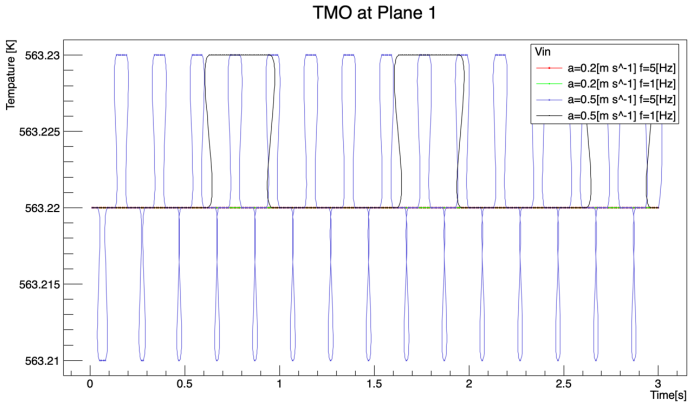

(a)

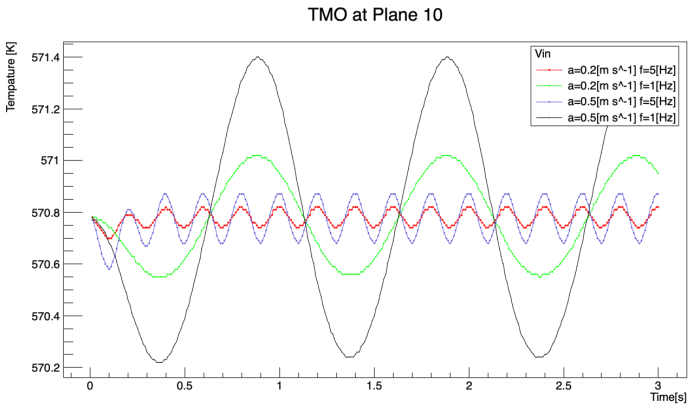

(b)

Figure 5.9: TMO at lower layers due to Vin oscillation.

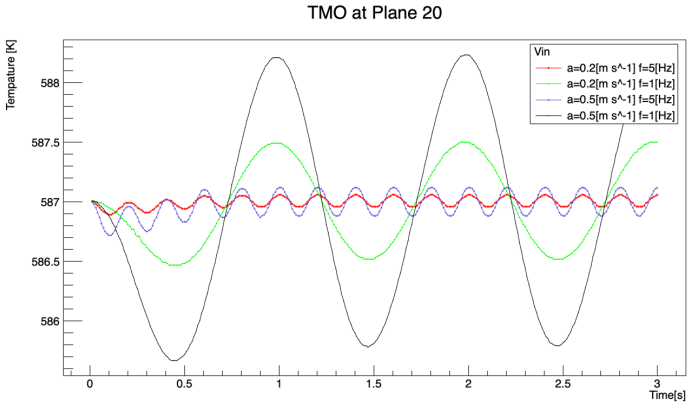

(a)

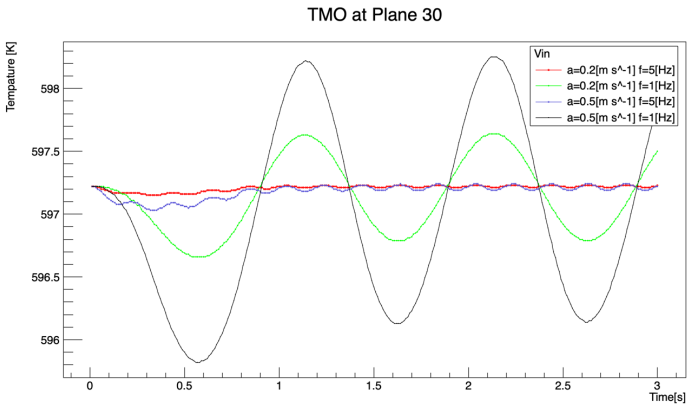

(b)

Figure 5.10: TMO at upper layers due to Vin oscillation.

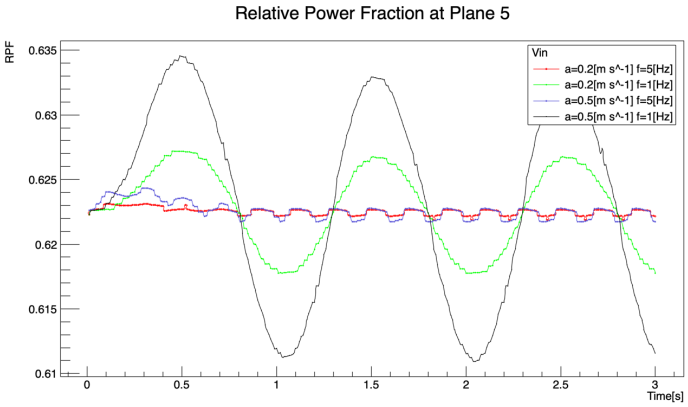

(a)

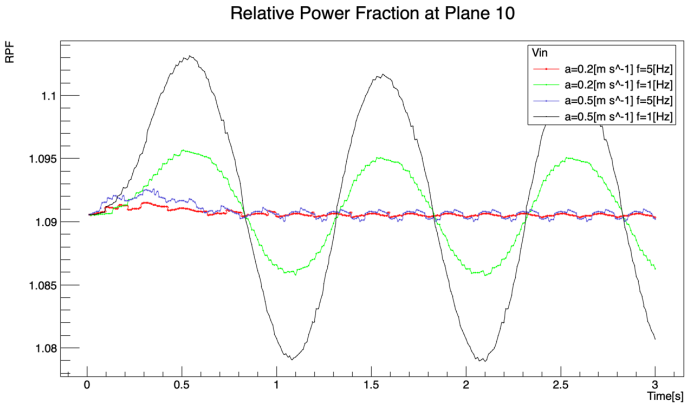

(b)

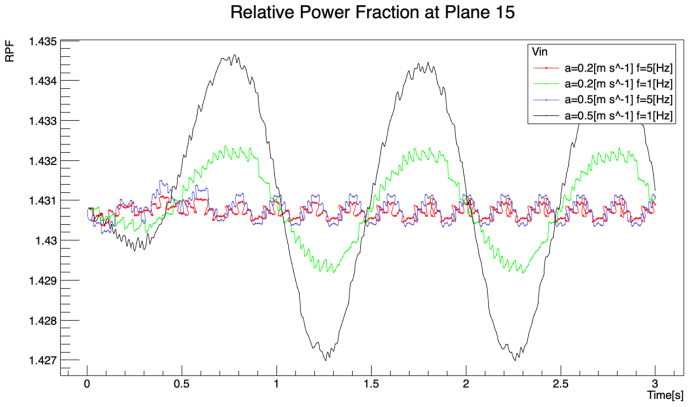

(c)

Figure 5.11: RPF at lower layers due to Vin oscillation.

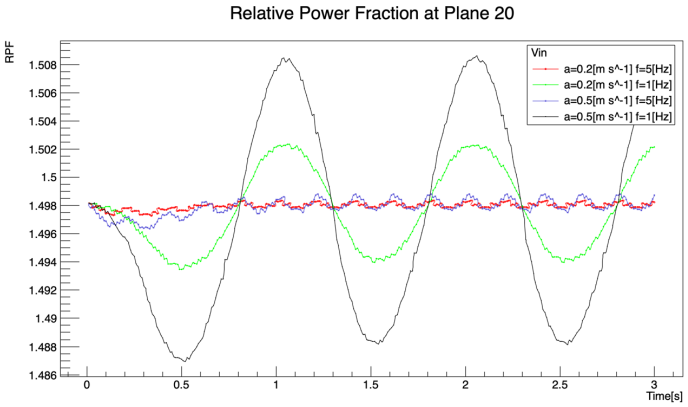

(a)

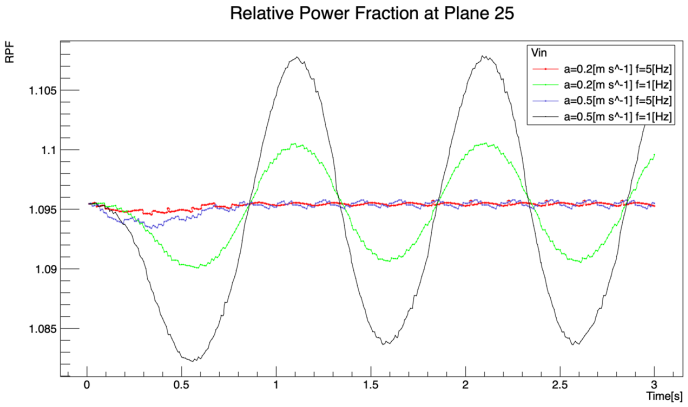

(b)

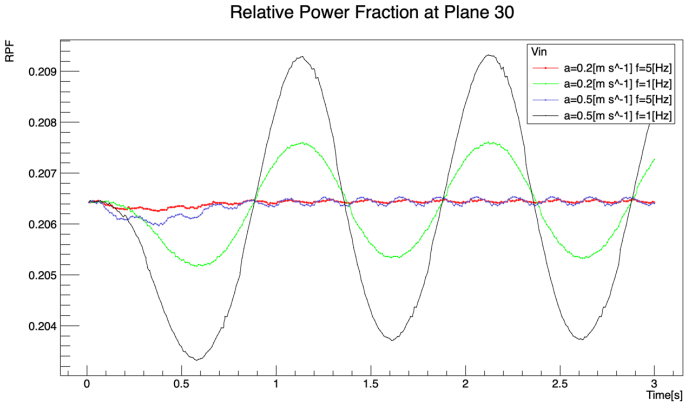

(c)

Figure 5.12: RPF at upper layers due to Vin oscillation.

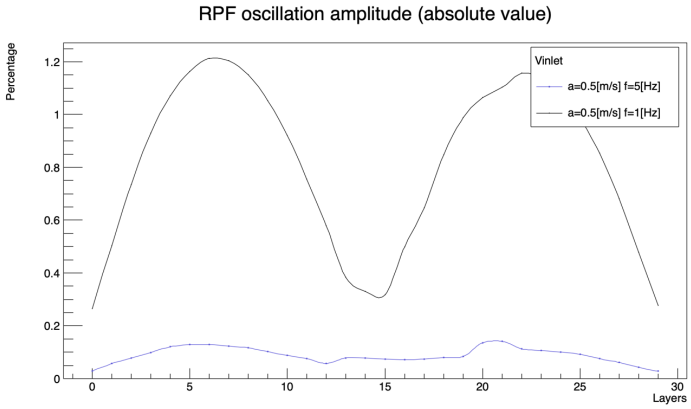

(a)

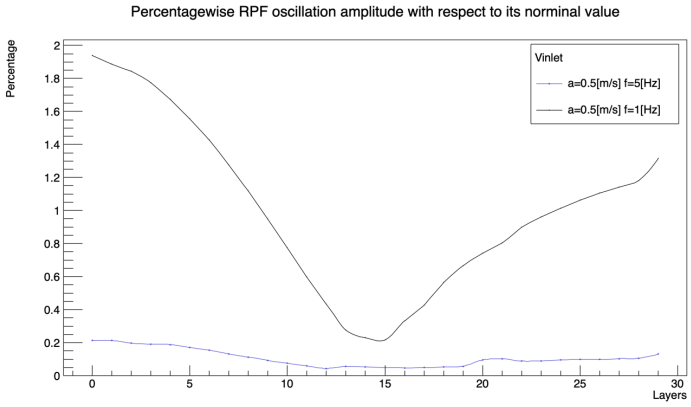

(b)

Figure 5.13: RPF oscillation amplitude along the axial direction in Vin cases.

5.5 Rod movement investigations

As it can be seen in Fig. 5.14 and 5.15, the nodal averaged temperature change due to the rod movement is very limited. And the relative power fraction change, on the other hand (Fig. 5.16 and 5.17), shows an oscillating behavior. But judging on the magnitude of the oscillation (below 0.05% at layer 10 for example), the rod vibration can hardly influence the RPF with a maximum displacement of 1mm.

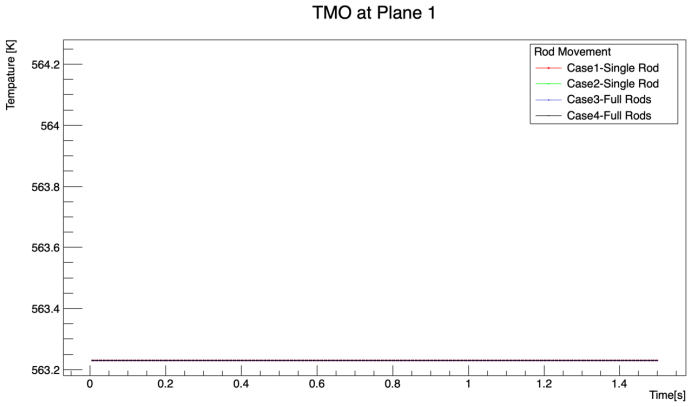

(a)

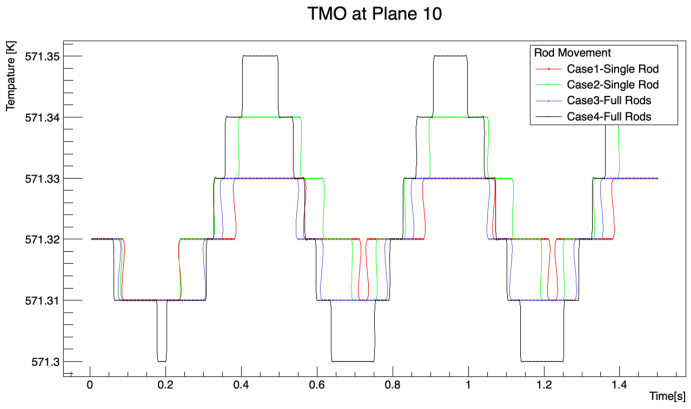

(b)

Figure 5.14: TMO at lower layers due to rod oscillation.

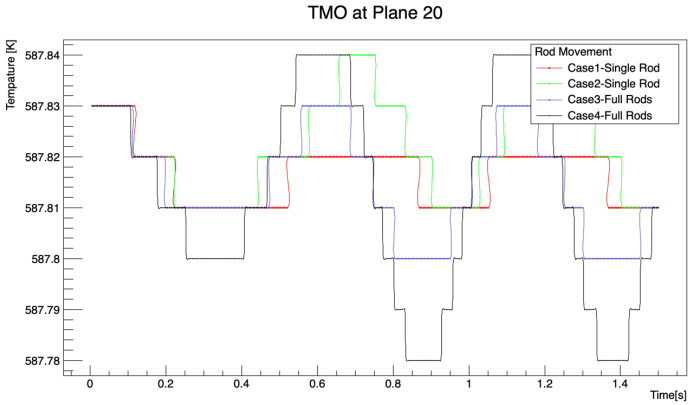

(a)

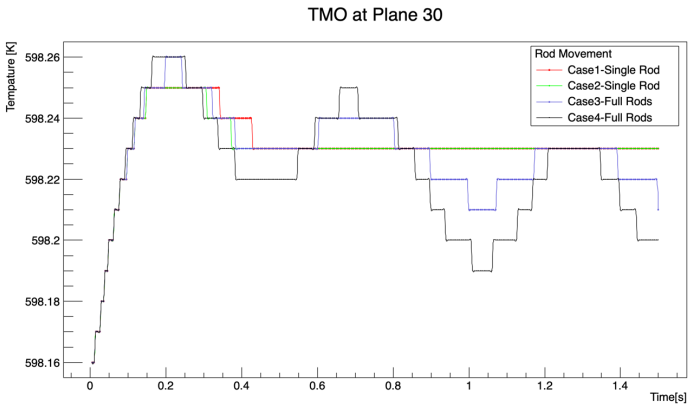

(b)

Figure 5.15: TMO at upper layers due to rod oscillation.

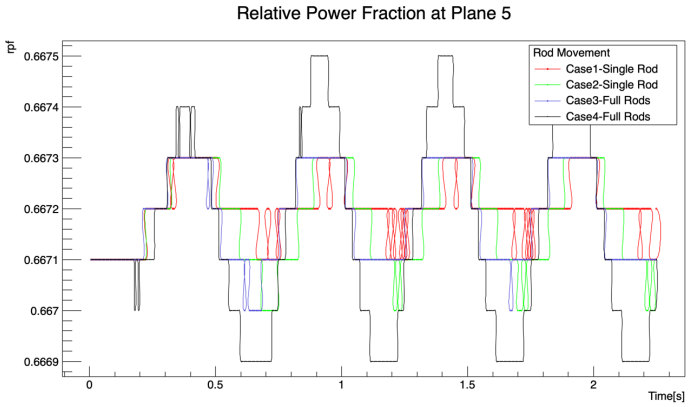

(a)

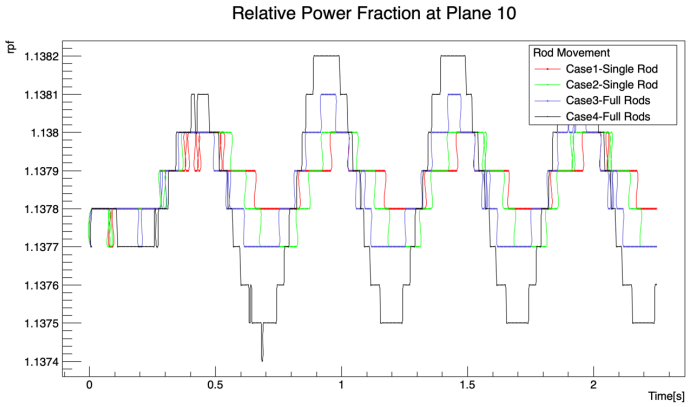

(b)

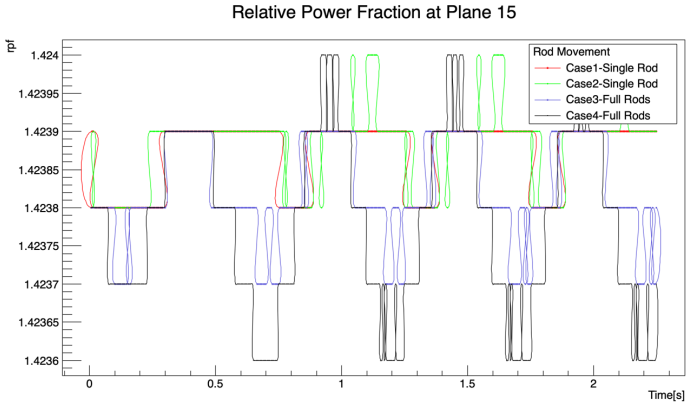

(c)

Figure 5.16: RPF at lower layers due to rod oscillation.

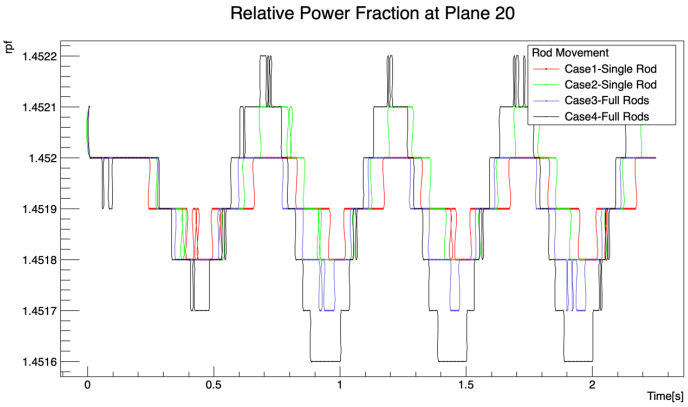

(a)

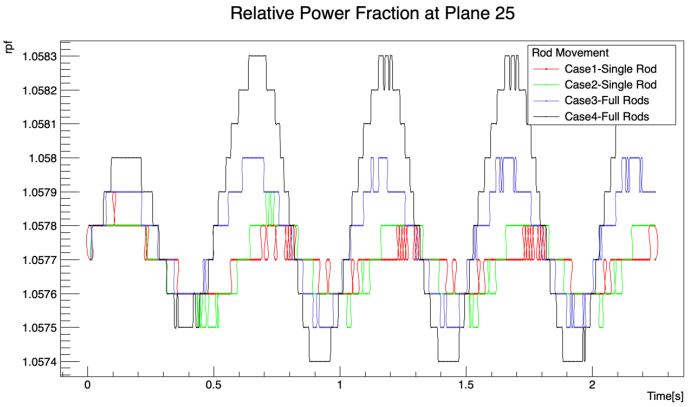

(b)

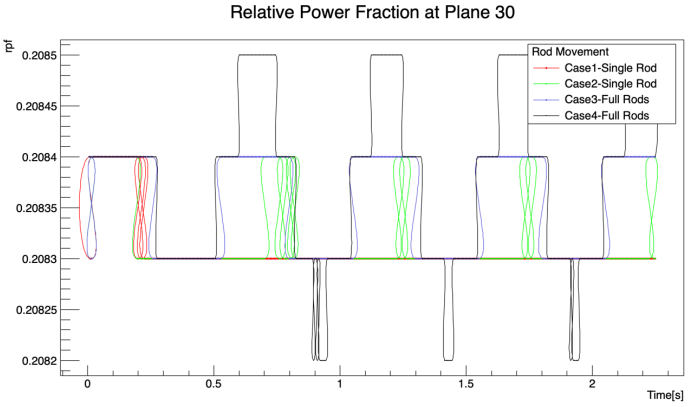

(c)

Figure 5.17: RPF at upper layers due to rod oscillation.

5.6 Summary

In this chapter, the coupled model is tested on the single fuel assembly model. Both steady-state and transient calculations are conducted. The transient cases are simulated with oscillating inlet temperature, oscillating inlet velocity and oscillating fuel rods to investigate the resulted power distribution oscillation.

In the Tin cases, two oscillation frequencies and two oscillation amplitudes are chosen so that the RPF response to different oscillation modes can be obtained. From the temperature oscillation aspect, it is seen that the oscillation amplitude at the top is smaller than at the bottom. The higher the frequency is, the faster the oscillation amplitude decreases with increasing height. The first behavior can be explained by the feedback of the neutronic field and the second behavior is caused by the fact that with a higher oscillation frequency, the coolant flow per unit time, which is influenced by the temperature oscillation, is smaller. Consequently the coolant flow is more influenced by the neutronics feedback and therefore the amplitude oscillation is decreasing faster with increasing height. From the neutronics aspect, the RPF oscillation is caused by the moderator temperature oscillation which includes the density factor in one-phase flow (since the cross-section generation puts these two factors together). In general high neutron oscillation happens when and where strong temperature oscillation occurs. It is seen that in the mode with low temperature oscillation frequency and high amplitude the neutron oscillation is the largest. After calibration (in Fig. 5.13) it is seen that the oscillation is the strongest at the bottom layer (about 12%) and the amplitude decreases from the bottom to the middle region (about 2%). Then the amplitude increases roughly linearly from the middle to the top region (about 8%). Besides, due to the transport effect of the coolant, the neutron oscillation also shows a phase difference between different layers. There is an almost 180°phase difference between the neutron signals at the top half and the bottom half of the fuel assembly.

In the Vin investigation, two oscillation frequencies and amplitudes are chosen based on the same consideration in the Tin cases. The transport effect can be barely seen in the temperature plot in the Vin cases since the change of inlet velocity is a global effect. Like the Tin cases, the neutronics feedback in the Vin cases also shows a 180°phase difference between the top and bottom half fuel assembly. The oscillation amplitudes correspond to 4.3% and 10.9% of the total mass flow rate and it is seen that the temperature oscillation under these conditions is relatively small. Therefore, the resulted neutronic oscillation is small compared the the Tin cases. Like the Tin cases, after calibration the amplitude of the neutron oscillation shows a similar behavior in the axial direction with a maximum of 2% at the bottom layer and a minimum of 0.2% in the middle.

The last part of single fuel assembly section consists of the investigations on the rod movement cases. It is seen that due to the changed flow area and the unchanged heat flux the moderator temperature has a slight oscillation (around 0.02K) which also results in a almost negligible neutron oscillation. One can also see that in case 4 where all fuel rods move in the diagonal direction has a higher oscillation amplitude. In the future investigation on the 3x3 FA model the FA will bow to the same direction (diagonal direction) to see some effects.

Since in the Tin and Vin cases it is seen that high frequency oscillations only bring limited influences on the temperature field as well as the neutronic field. It is decided to fix the frequency 1 Hz in the future 3x3 FA model to see the effect more clearly.

In the next chapter the results using the coupled 3x3 FA model are illustrated. The CFX model is built with an simplified mesh due to the lack of computation resources. From the neutronics point of view, PPFs are calculated for the 3x3 FA model under both FA bow and no FA bow conditions. A dramatic ADF change can be observed and the power distribution of the fuel pins on the periphery row change up to 8% when the center fuel assembly

has a displacement of 2mm in both x- & y-directions. Besides, the pin power distribution change has a roughly linear correlation with the displacement.

Chapter 6

3x3 FA Simulation

This chapter depicts the results of the TH/neutronics coupled transient simulations with both SERPENT and CASMO cross sections. The SERPENT XS simulations (shown in sec. 6.1) address the neutronics response of a chess board configuration filled with U-FA and Gd-FA. Both kinds of FAs are in fresh state. In this part the pin-by-pin power distribution is implemented in the FA bow investigation to achieve a higher fidelity. In the second section the CASMO XS simulations (shown in sec. 6.2) contain more investigations on the influence of BUs and MOX-FA.

6.1 SERPENT XS simulations

6.1.1 Description of the Cases

The model has been extended to the 3x3 FA model in order to investigate the relative power fraction change due to flow oscillations in a larger scale. Heat transfer as well as the cross flow is enabled between two neighboring fuel assemblies. The averaged power for each fuel assembly is kept at 20MW. The RPF evaluation only reflects the power fraction relative to the nominal power. The model has a chessboard configuration in the radial direction

(shown in Fig. 6.1) consisting of two different FA types (Gd-FA and U-FA). The power difference between the center FA (Gd-FA) and its neighboring FAs (U-FAs) is about 10%. The boron concentration is set to be in one case as 500ppm while in the other case 2200ppm. As it is shown in section 3.2.3, the pin power distribution can be influenced by the fuel assembly bow. Therefore, additional subroutine is implemented in the rod movement cases in the coupling model to apply the heterogeneous heat generation rate on the fuel pins. Results are compared in this section between simulations with PPFs and without PPFs to see whether PPFs have an influence on both temperature and neutronic field.

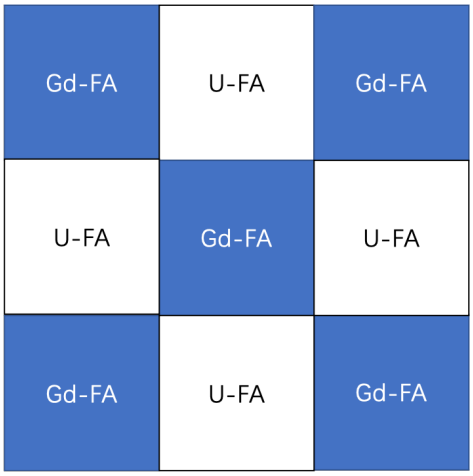

Figure 6.1: Radial configuration of the SERPENT XS case

In sec. 6.1.2 the steady state calculation results are shown for both BOR 500ppm and 2200ppm cases. In sec. 6.1.3 the results of selected transient calculations are shown and discussed.

6.1.2 Steady-State Calculation

Fig. 6.2 depicts the axial averaged RPF for the 3x3 fuel assembly matrix in both cases. The radial power distribution is pretty similar in both cases showing a factor of 0.97 in the middle and 0.94 in the corner fuel assembly despite of different boron concentrations. On the other hand, because of

different boron concentrations, the axial power distribution shows a different shape. Fig. 6.3 illustrates the axial relative power fraction of FAs at different locations (FA3, FA5, FA6). The axial power distribution in the BOR500ppm case has a peak in the lower half of the fuel assembly (around node 11) whereas in the BOR2200ppm case the peak is located slightly above the middle of the fuel assembly (around node 18). The maximum RPF is around 1.6 in the BOR500ppm case and 1.54 in the BOR2200ppm case.

In Fig. 6.3 the axial moderator temperature distribution is shown for FAs at different locations. Since the radial power distribution is almost the same in both cases, it is seen that the moderator temperature is quite the same at the outlet (node 30) in both cases. The maximal moderator temperature is around 597.8K for the middle Gd-FA (FA5), 600.6K for the side U-FA (FA6) and 596.6K for the corner GA-FA (FA3).

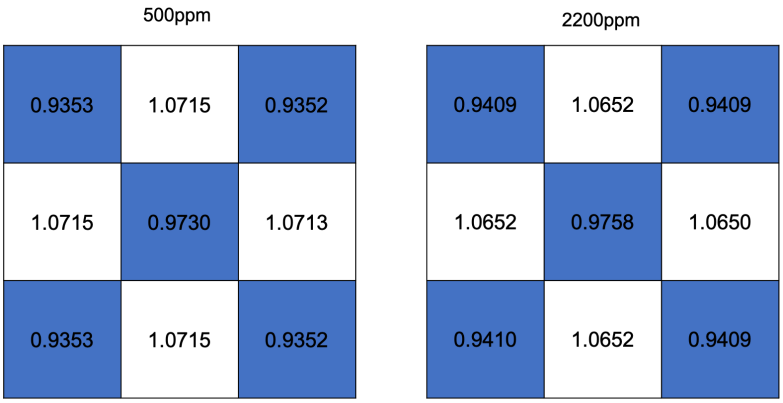

Figure 6.2: The radial RPF distribution of the steady state calculation with the 3x3 assembly model (SERPENT XS): 500ppm case (left), 2200ppm case(right).

Besides, Fig. 6.4 shows the moderator temperature distribution radially at the height of 2.5m. It can be seen that the moderator temperature distribution is locally influenced by PPFs. By applying the PPFs, the power is higher at the fuel pins around the guide tubes where a higher moderation effect is expected. The location of the Gd fuel rod can also be easily identified since the Gd is a strong neutron absorber and its power is largely suppressed

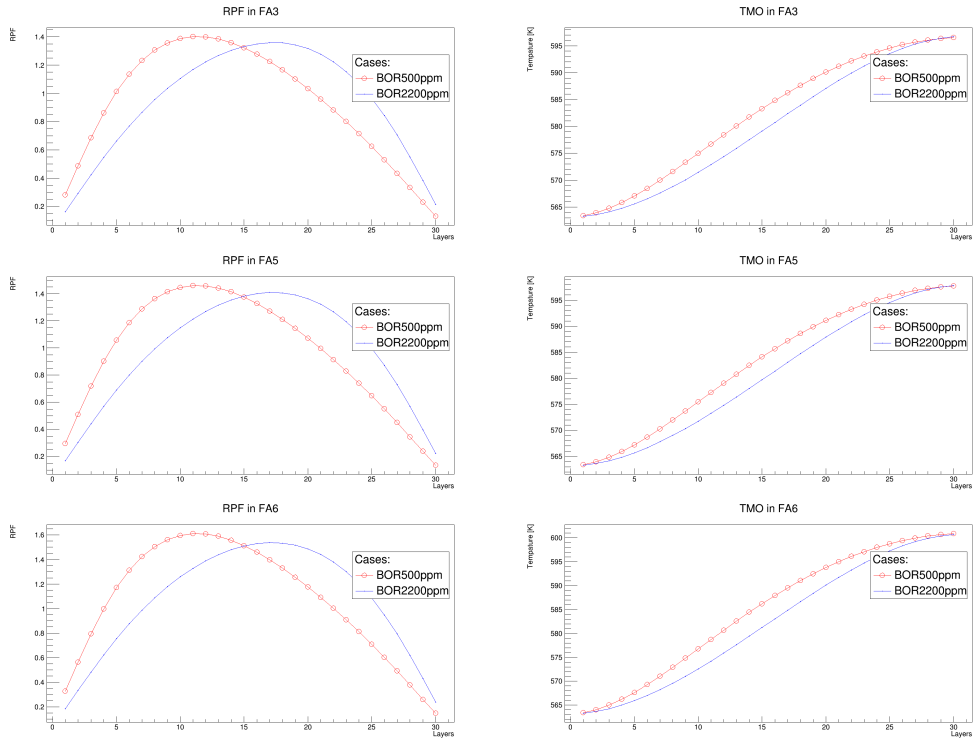

Figure 6.3: The axial RPF and moderator temperature distributions in the steady state calculation with the 3x3 fuel assembly model (SERPENT XS).

compared to other fuel rods.

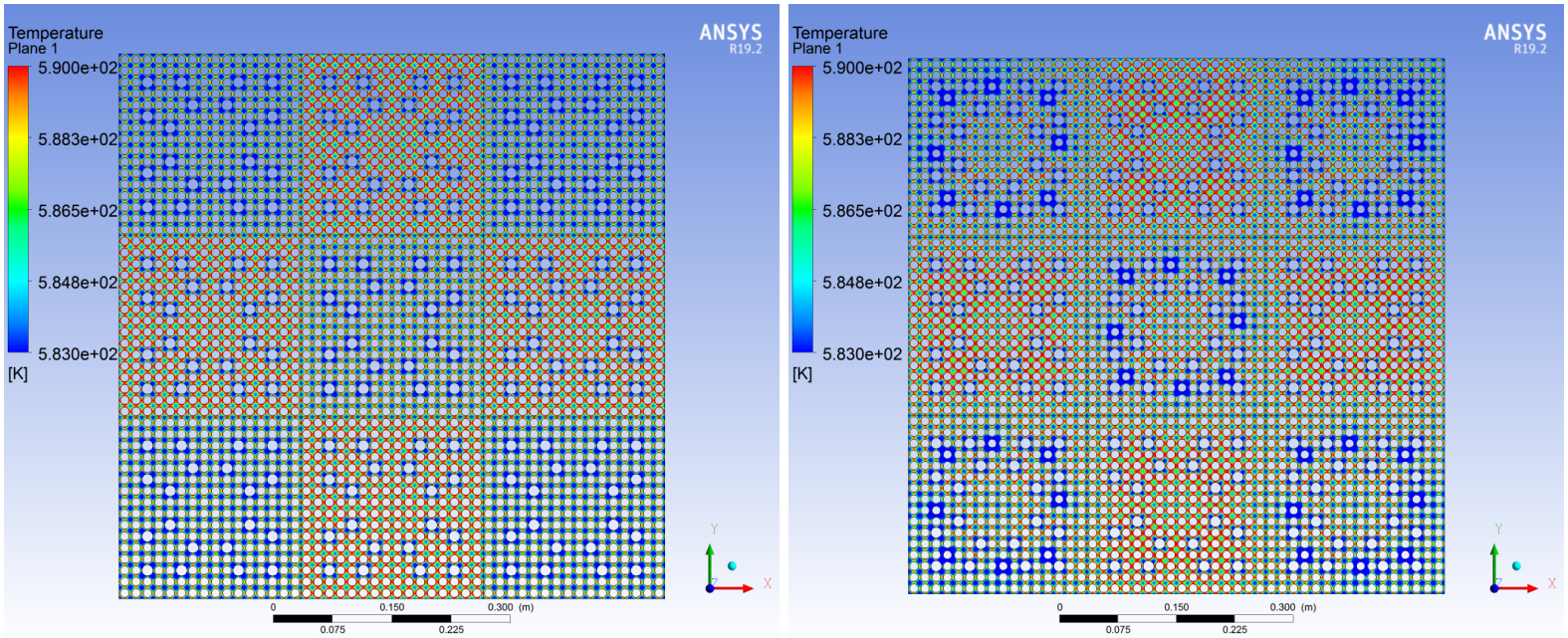

(a) Without PPFs

(b) With PPFs

Figure 6.4: The radial moderator temperature distribution of the steady state calculation with the 3x3 fuel assembly model at the height of 2.5m (SERPENT XS).

6.1.3 Transient Calculations

This section presents the results of applying different oscillating boundary conditions on the model. A sine form time dependent disturbance is applied to the moderator inlet temperature and moderator inlet velocity (see Eq. 6.1). The frequency is fixed at 1Hz and the amplitude of the oscillation varies. Another varying parameter is the location where the oscillation boundary condition is applied. Here it differs between FA5 and all FAs. A list of the cases is shown in Tab. 6.1.

$$\delta = a \cdot sin(t \cdot 1[Hz] \cdot 2\pi) \tag{6.1}$$

where δ is the time dependent disturbance, a is the amplitude of the oscillation and t is time.

As for the simulations with the fuel assembly bow, here the bow is simply assumed located in the center fuel assembly where axially the displacement follows a sine distribution which means 0mm for the top and bottom and maximum at the middle of the fuel assembly. The direction of the vibration is just assumed to be in x- & y-direction (diagonal direction). And the maximum displacement is assumed to follow a rump function (shown in Fig. 6.5).

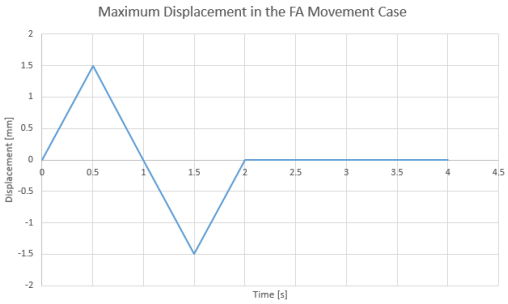

Figure 6.5: The maximum displacement of the center fuel assembly in the FA bow case (SERPENT XS).

	a	Location	BOR [ppm]
Tin	-3[K]	FA5	500
	-5[K]	FA5	500
	-3[K]	All FAs	500
	-5[K]	All FAs	500
	-3[K]	FA5	2200
	-5[K]	FA5	2200
	-3[K]	All FAs	2200
	-5[K]	All FAs	2200
Vin	0.5[m/s]	FA5	500
	1.0[m/s]	FA5	500
	0.5[m/s]	All FAs	500
	1.0[m/s]	All FAs	500
	0.5[m/s]	FA5	2200
	1.0[m/s]	FA5	2200
	0.5[m/s]	All FAs	2200
	1.0[m/s]	All FAs	2200

Table 6.1: Cases under oscillating moderator inlet boundary condition with 3x3 fuel assembly model (SERPENT XS).

6.1.3.1 Tin investigations

Fig. 6.6 shows the nodal TMO at different axial layers of two neighboring FAs (FA5 and FA6) due to the Tin oscillation. The label in the legend-box contains the basic boundary condition of the transient: the magnitude of the oscillation, the location of the applied oscillation and the boron concentration. Noted that the inlet coolant velocity is around 4.6m/s and the total active length is 3.9m which means that the coolant total travel time is about 0.85s. This can also be seen when comparing the TMO charts between plane 1 and plane 30 that the first bottom in the 30th plane is about at around 1.1s whereas in the 1st plane at about 0.26s. Due to different boundary conditions (oscillation modes & boron concentration) and the resulting neutronics feedback, the temperature oscillation of the other planes can have different amplitudes than the inlet boundary condition. For example in FA5, with an oscillating inlet temperature of 3K the outlet temperature oscillates with a smaller amplitude (around 2.2K) in both BOR500 cases whereas in the

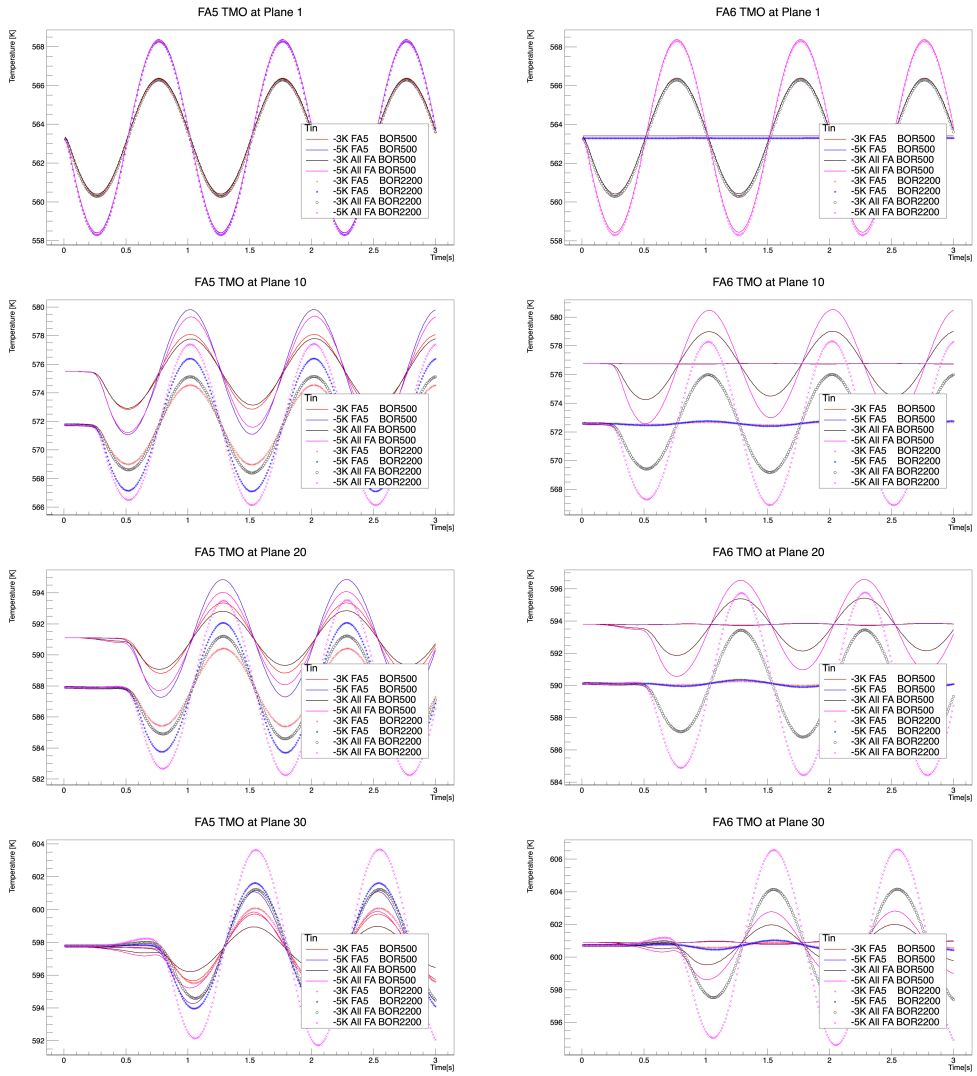

(a) (b)

Figure 6.6: TMO oscillation due to Tin oscillation with 3x3 FA model (SERPENT XS).

BOR2200 cases with oscillation applied on all FAs the outlet temperature oscillates with a slightly higher amplitude of 3.3K. A similar behavior can also be found in FA6 temperature distribution.

The neutronics response (RPF) also shows a oscillating behavior (shown in Fig. 6.7). When comparing cases of BOR500 and cases of BOR2200, it is seen

that at the beginning of the transient due to different neutronics feedback (different moderator temperature feedback caused by boron concentration) the power increases in the bottom half in the BOR500 cases while decreasing in the BOR2200 cases. The power in the upper half of the fuel assembly reacts oppositely. It can also be seen when the oscillating boundary condition is applied only on the central fuel assembly, the power oscillation is smaller compared to the "ALL FA" cases.

In Fig. 6.8 the RPF oscillation amplitude of each plane is normalized to its initial value. This figure gives an idea of the oscillation amplitude detected by the detectors at different axial height. It is seen in both figures the power oscillation has a minimum amplitude at about the middle height (around plane 15). The power oscillation is generally smaller in "FA5" cases than in "All FA" cases indicating that the local oscillation of inlet TMO, in which only small amount of FAs are involved, has a limited effect on the neutronics field. With an amplitude of 5K oscillating inlet TMO on FA5, the power fraction on each plane only oscillates about 0.2 to 2%. On the other hand, when the oscillating BC is applied on all FAs' inlet, with an amplitude of 5K, the power can oscillate between 1 to 13%.

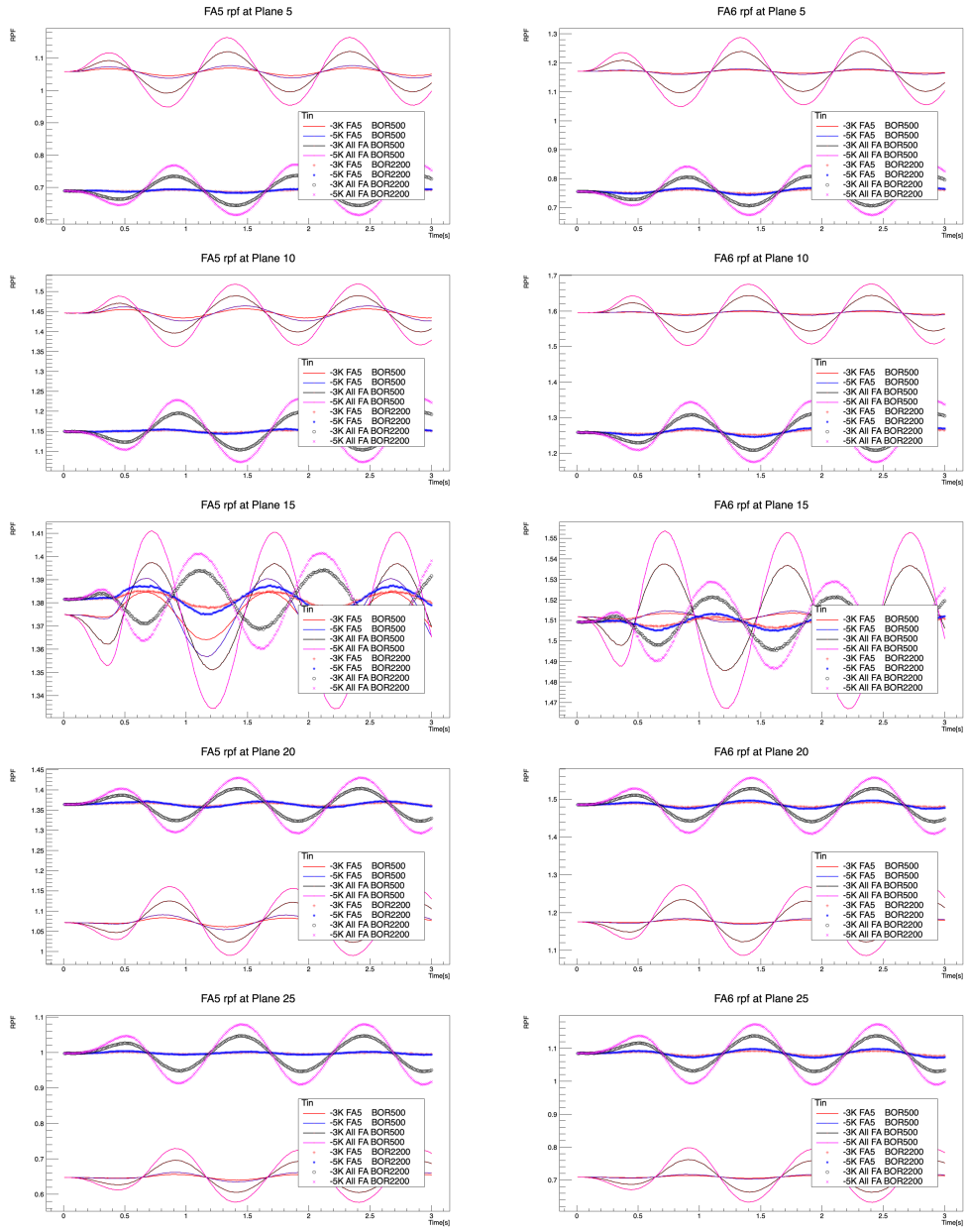

(a) (b)

Figure 6.7: RPF oscillation due to Tin oscillation with 3x3 FA model (SERPENT XS).

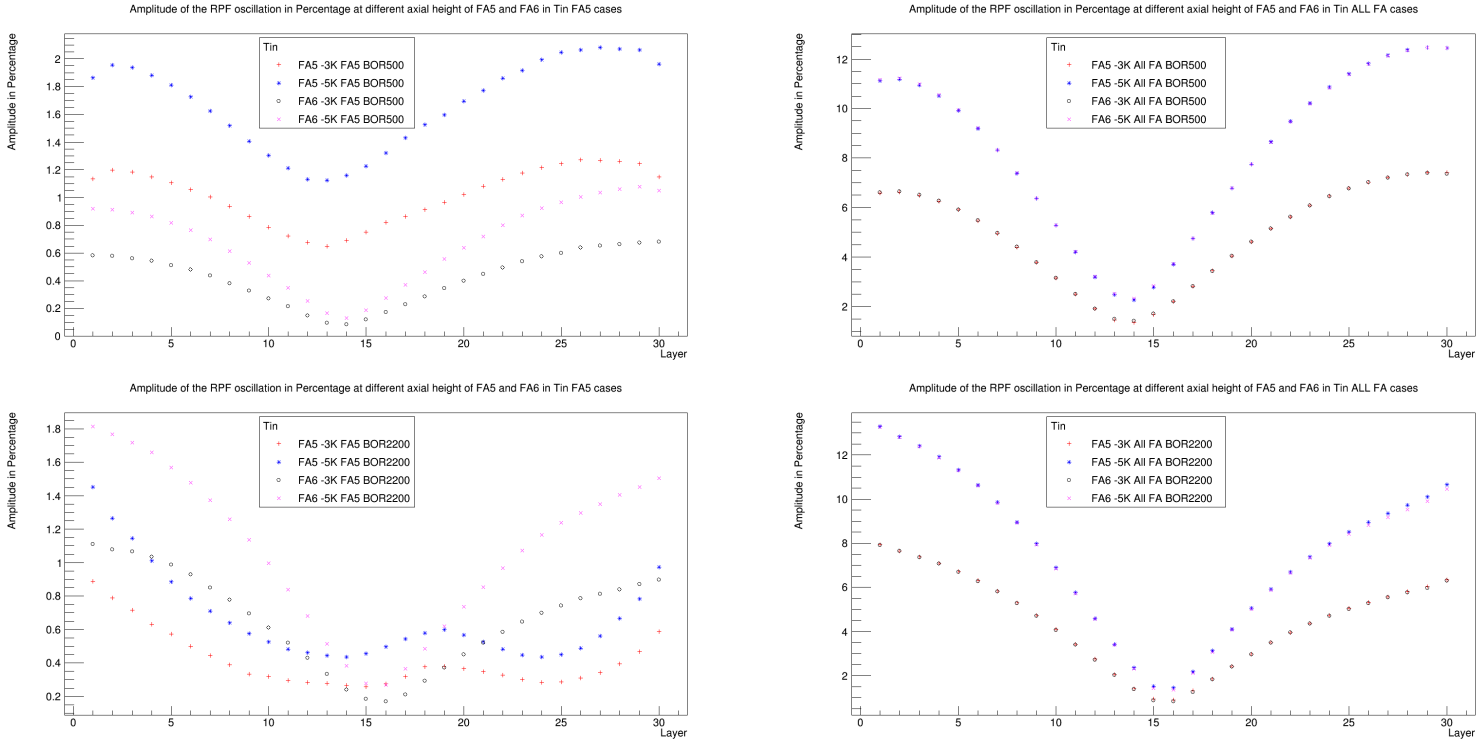

Figure 6.8: Percentage-wise amplitude of RPF oscillation with respect to its reference value at different axial height of FA5 and FA6 in Tin (left: FA5, right: All FA) cases (SERPENT XS).

6.1.3.2 Vin investigations

Assuming that the inlet moderator temperature doesn't change, changing the inlet velocity change results in the inlet mass flow change. Consequently the moderator temperature oscillates since the total heat power conducted through the cladding surface remains merely changed. Unlike the Tin cases in which the temperature change has some transport effect along the axial direction, the mass flow change should be effective on all axial planes at the same time since the mass continuity law must be fulfilled. Besides, different mass flow should induce different pressure loss for different FAs resulting in cross-flow between FAs which could introduce more moderator mixing effects (cold and hot moderator in neighboring FAs). But on the other hand, the cross-flow also compensates the mass flow difference which is introduced on the inlet and in the end the mass flow is quite similar in each FA.

Fig. 6.9 illustrates the temperature oscillation of both FA5 and FA6 at different layers in the Vin cases. With an increasing inlet velocity which is equivalent to an increasing mass flow rate, the moderator temperature on all axial layers also oscillates. In general, the larger the amplitude of the Vin oscillation is, the stronger the moderator temperature oscillates on each plane. Unlike the Tin cases, there's a phase difference of the TMO oscillation between "FA5" and "ALL FA" cases. It is seen in "FA5" cases, the TMO on each plane reaches its first bottom value 0.2-0.5s later than in the "ALL FA" cases and the higher the plane is, the later the oscillation reaches its first bottom. This can be explained that due to the pressure difference between two FAs the induced cross-flow helps the moderator to redistribute and rehomogenize. And the rehomogenization can also influence the moderator temperature which furtherly influences the power distribution.

In Fig. 6.10, the RPF changes of both FA5 and FA6 at different axial height are shown for the Vin oscillation case. The RPF change shows a similar behavior to what we observed in the Tin cases, namely with a decreasing inlet velocity the RPF of the bottom half FA decreases in the BOR500 cases

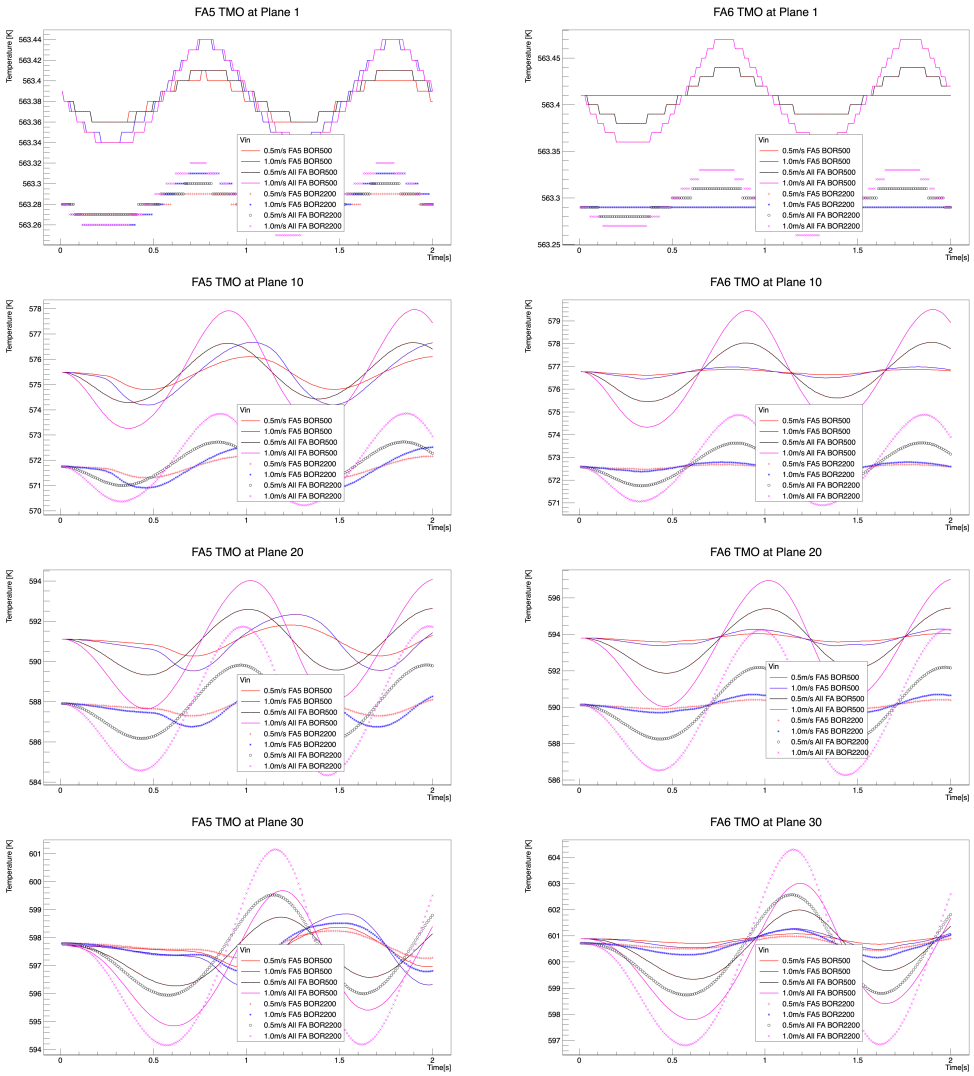

(a) (b)

Figure 6.9: TMO oscillation due to Vin oscillation with 3x3 FA model (SERPENT XS).

while increases in the BOR2200 cases. The amplitude of the RPF oscillation is quite small for the cases in which only the FA5 inlet boundary condition is changed. As a consequence, the RPF oscillations of these cases contribute a negligible amount of influence to the TMO oscillations. And the TMO oscillates mainly due to the mass flow rate change. On the other hand, since the amplitude of the TMO oscillation is small, the neutronic field can also

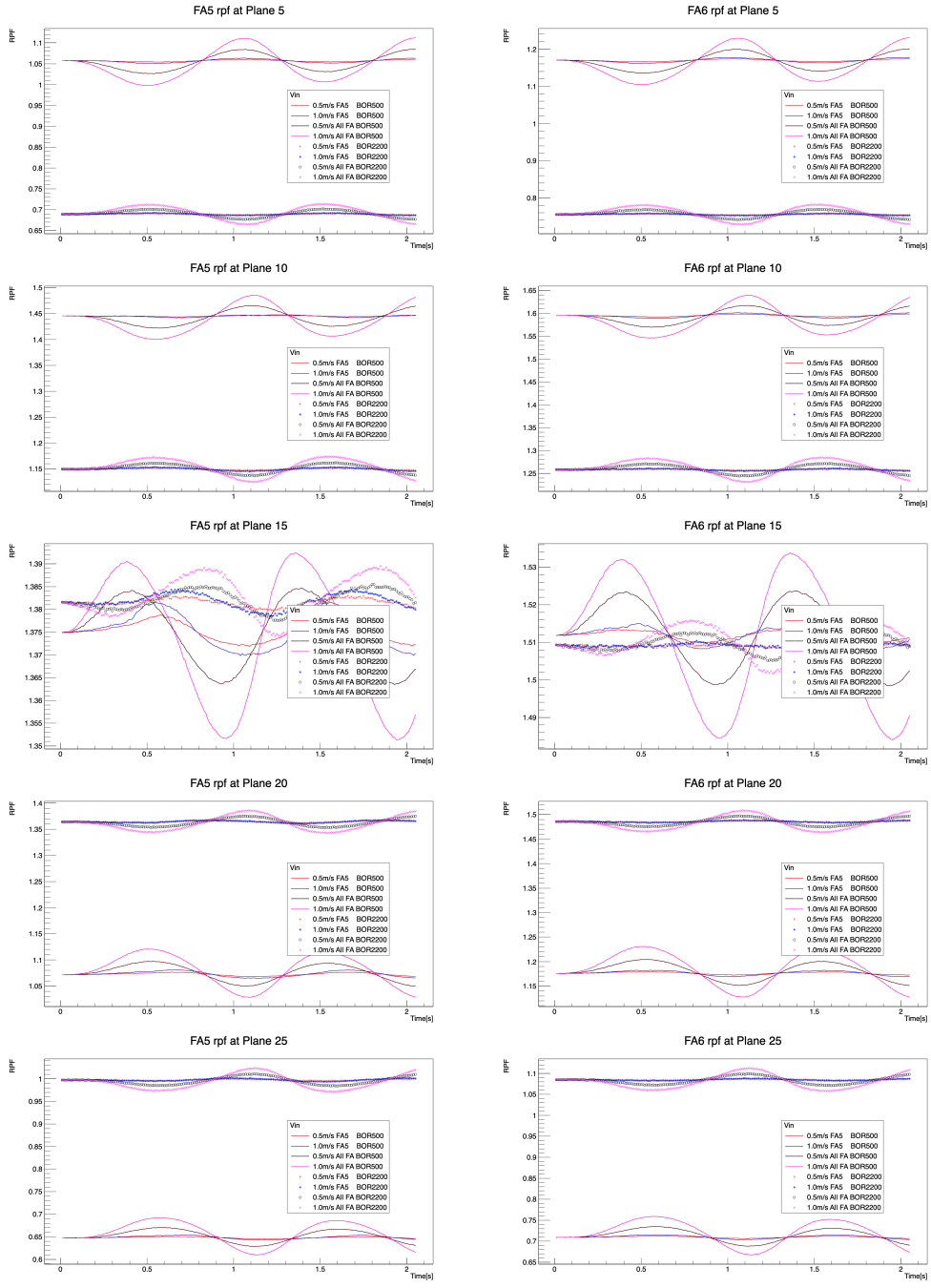

(a) (b)

Figure 6.10: RPF oscillation due to Vin oscillation with 3x3 FA model (SERPENT XS).

only be limited influenced. As a consequence, the temperature oscillation is reduced in "FA5" case.

The percentage-wise amplitude of the RPF oscillation is plotted in Fig. 6.11 for FA5 and FA6 with different axial heights. Similar to the Tin cases, the RPF oscillation amplitude is larger in the "All FA" cases than in the "FA5" cases. It can also be seen that, in these cases the middle region is the least influenced region with values of around 1% in "BOR500" cases and around 0.5% in "BOR2200" cases (e.g. in "ALL FA" cases). The effect is more obvious at the top and the bottom region. Up to 6% (BOR500) and 4% (BOR2200) RPF oscillation can be found at the top and bottom layer (e.g. in "ALL FA" cases).

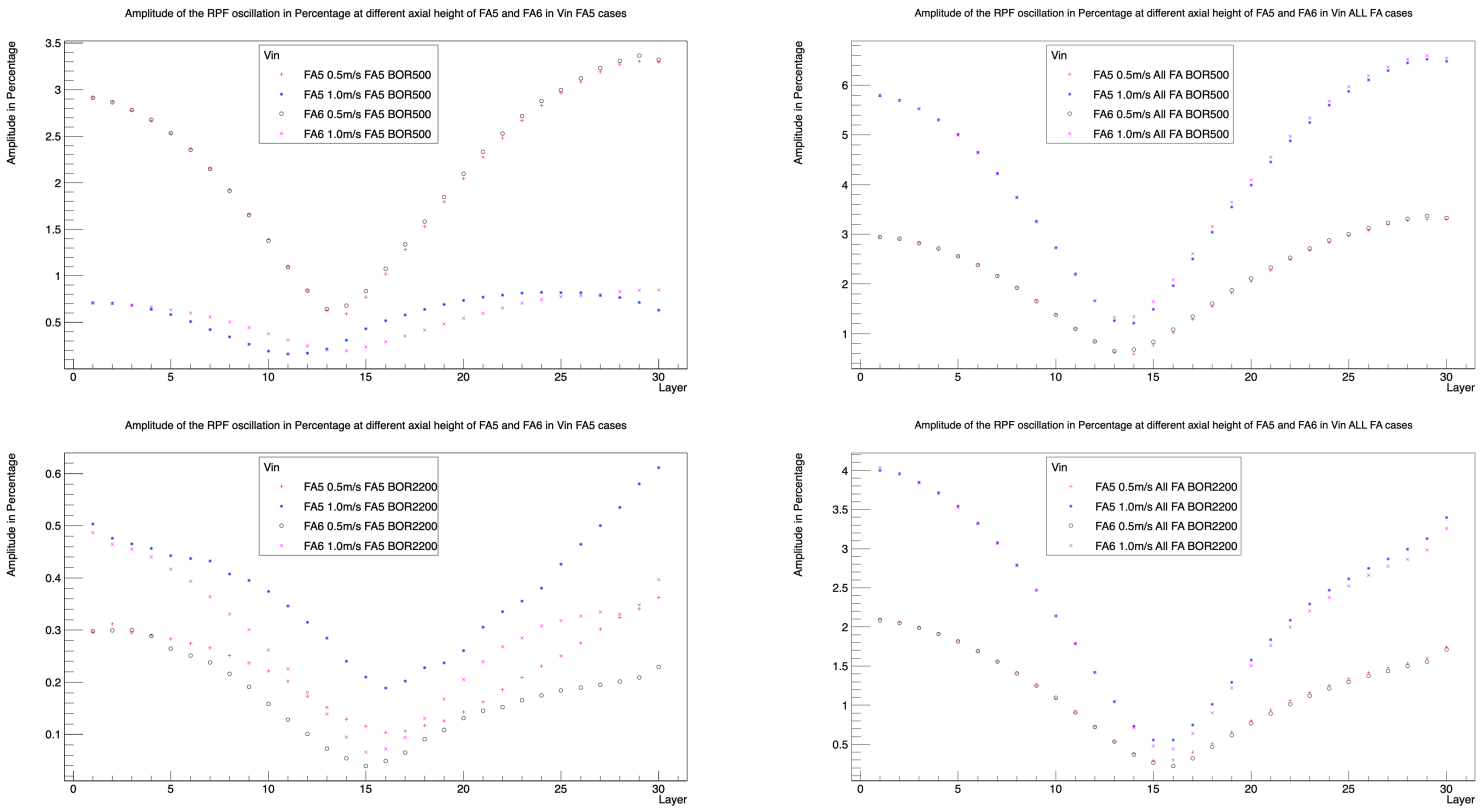

Figure 6.11: Percentage-wise amplitude of RPF oscillation with respect to its reference value at different axial height of FA5 and FA6 in Vin (left: FA5, right: ALL FA) cases (SERPENT XS).

6.1.3.3 Rod movement investigations

In Fig. 6.12 and 6.13, the results of moderator temperature and relative power fraction are shown for FA5 and FA6 at different axial planes. It is seen that although some oscillating behavior can be observed in the TMO plot at plane 20 for both FA5 and FA6, the amplitude of the oscillation is still relatively small (0.06K for FA5 and 0.1K for FA6) to cause an obvious change in the relative power fraction. Furthermore, the neutronic response doesn't show an oscillating behavior and the amplitude can also be considered as negligible small (smaller than 0.1%). Therefore, PPFs doesn't play an important role here.

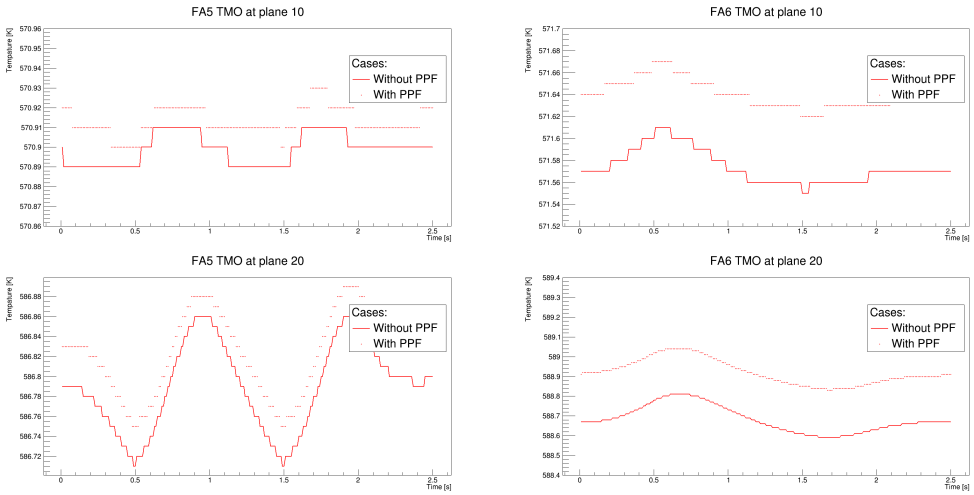

Figure 6.12: TMO of FA5 and FA6 at plane 10 and plane 20 due to FA bow (SERPENT XS).

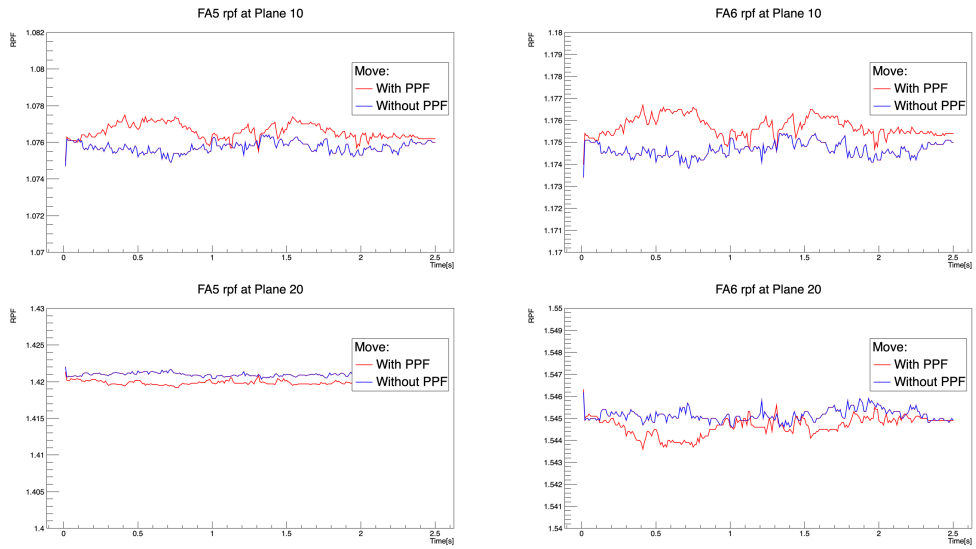

Figure 6.13: RPF of FA5 and FA6 at plane 10 and plane 20 due to FA bow (SERPENT XS).

6.2 CASMO XS simulations

6.2.1 Description of the Cases

Changing the burnup of the fuel assembly meaning changing the internal nuclide vector can strongly influence the neutronic feedback coefficients (the moderator temperature coefficient, the Doppler feedback coefficient, etc.). It is shown in Tab. 3.6 that the moderator temperature coefficient of the U-FA becomes almost twice as large when changing the burnup from 0 to 30 MWd/kgHM. Considering that the real reactor core has a heterogeneous loading pattern, that is to say the neighboring fuel assemblies could have different types (Uranium, MOX, shown in Fig. 6.14), different enrichments and different burnups, the neutronic behavior of each fuel assembly inside a bundle unit (e.g. 3x3 FA matrix) can be different under a transient situation.

The purpose of this section is investigate the neutronic behavior of each fuel assembly inside the 3x3 FA matrix with different burnup compositions under transient conditions. Two types of configuration are applied in this investigation: one configuration only with Uranium-FA, the other configuration with both Uranium-FA and MOX-FA. Both a heterogeneous FA pattern and a heterogeneous burnup distribution are considered. Besides, two sets of boron concentration are applied: 1300ppm simulating a BOC condition while 50ppm simulating a near EOC condition. A more detailed overview of the setups is shown in Tab. 6.2. The transient cases are set to be the same cases as the SERPENT cases described in Sec. 6.1.1.

Configuration	Burnup [MWd/kgHM]	Boron Concentration [ppm]
U-FA	0-10	50
	0-10	1300
	10-30	50
	10-30	1300
U-FA & MOX-FA	0-10	50
	0-10	1300
	10-30	50
	10-30	1300

Table 6.2: FA pattern, burnup and boron concentration setup for the CASMO cases.

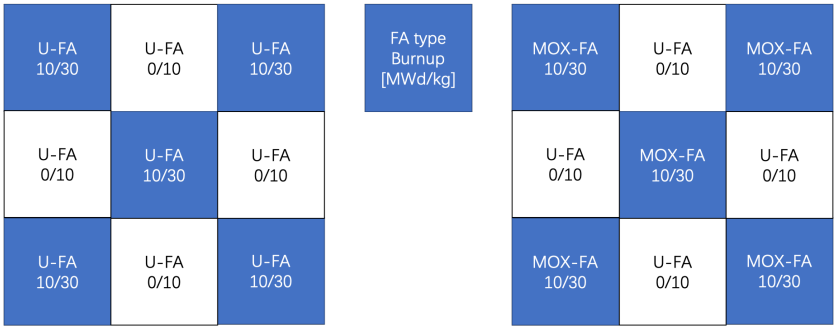

Figure 6.14: The radial configuration of the CASMO cases.

6.2.2 U-FA Cases

6.2.2.1 Burnup 0-10 MWd/kgHM

6.2.2.1.1 Steady-State Calculation

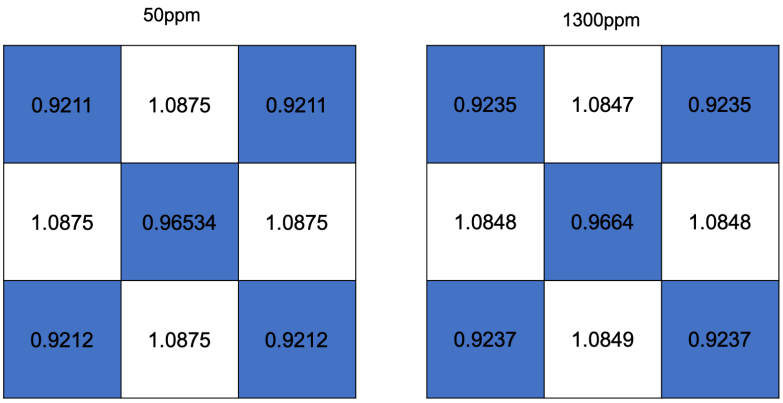

Figure 6.15: The radial RPF distribution of the steady state calculation with the 3x3 assembly model (CASMO XS, U-FA, BU: 0-10 MWd/kgHM): 50ppm case (left), 1300ppm case(right).

Fig. 6.15 depicts the radial power distribution of each FA with respect to different boron concentrations. Compared to the SERPENT XS cases, the power fraction distribution is similar.

Fig. 6.16 depicts the moderator temperature distributions along the FA 3, 5 and 6. The outlet temperature is around 596K in FA3, 597.5K in FA5 and 601K in FA6. In Fig. 6.16 the RPF is plotted for each planes in FA3, FA5 and FA6. While in the BOR50ppm case the axial power profile has a peak on the bottom half of the FA, the axial power profile in the BOR1300ppm is more symmetric distributed. The maximum RPF can be found in FA6 with a value of 1.6 in the BOR50ppm case and 1.45 in the BOR1300ppm case respectively.

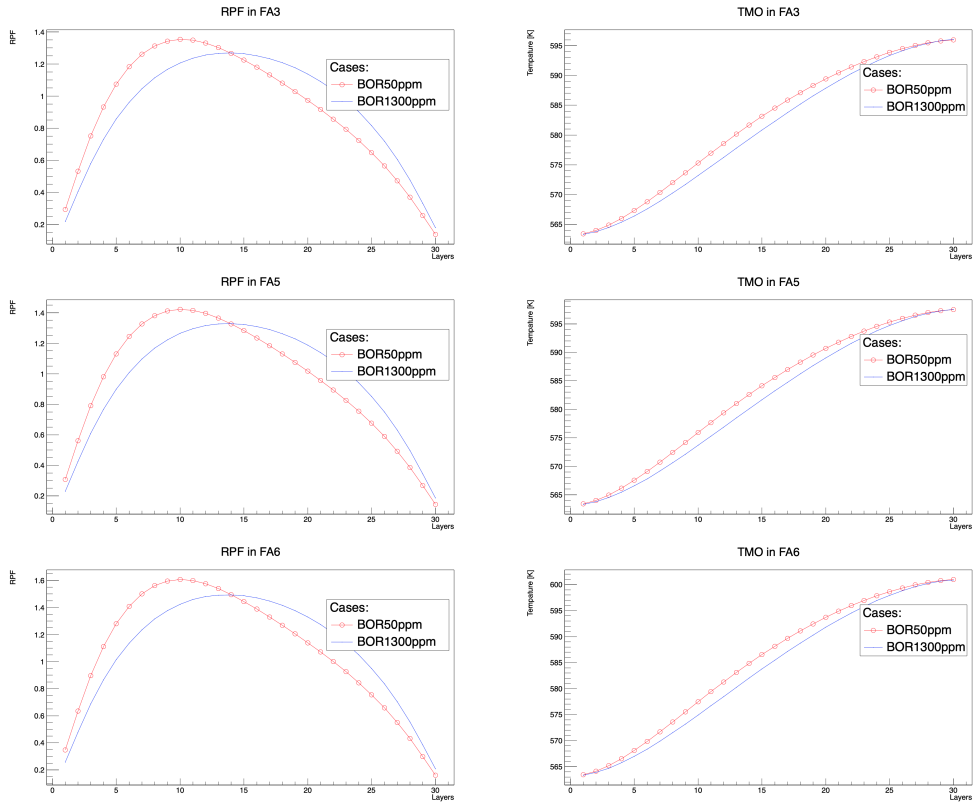

Figure 6.16: The axial RPF and TMO distribution in the steady state calculation with the 3x3 fuel assembly model (CASMO XS, U-FA, BU: 0-10 MWd/kgHM).

6.2.2.1.2 Transient cases

6.2.2.1.2.1 Tin cases

In Fig. 6.17 the TMO is shown for FA5 and FA6 with respect to different axial planes. Beside the temperature oscillation similar to the cases before, an interesting point is that while in the BOR1300 cases the temperature oscillation has a similar amplitude on each plane in FA5 when the inlet temperature oscillation has the same amplitude (-3 or -5K), whereas in the BOR50 cases the temperature oscillation has a obvious different amplitude between "FA5" and "ALL FA" cases. This behavior will be explained in the following paragraph when taking the RPF oscillation into consideration.

The neutronics response (RPF) also shows a oscillating behavior (shown in Fig. 6.18). In general the neutronics field is more sensitive to the temperature oscillation when the boron concentration is low (50ppm). When the inlet temperature decreases the positive reactivity causes the RPF at the bottom half of the FA to increase and on the contrary at the upper half to decrease. The increasing power at the bottom half also minimizes the temperature oscillation. Since the RPF oscillation is higher in the "ALL FA" cases compared to the "FA5 case", the TMO oscillation is more compensated in the "ALL FA" cases. On the other hand, when the the "cold" moderator travels to the upper part the induced increasing power in the upper half will continue minimizing the temperature oscillation. As a result, the temperature oscillation of FA5 in the "ALL FA" cases is smaller compared to the "FA5" cases (when the TMO oscillation amplitude is the same). This behavior can also be observed in the SERPENT cases (BOR500 cases) in Fig. 6.6, but the difference in the oscillation amplitude is not as obvious as the BOR50 case. But on the other hand, when the boron concentration is high enough (e.g. 2200ppm in SERPENT cases), the decreasing TMO introduces a negative reactivity which has an opposite effect on the RPF oscillation and results in a larger TMO oscillation.

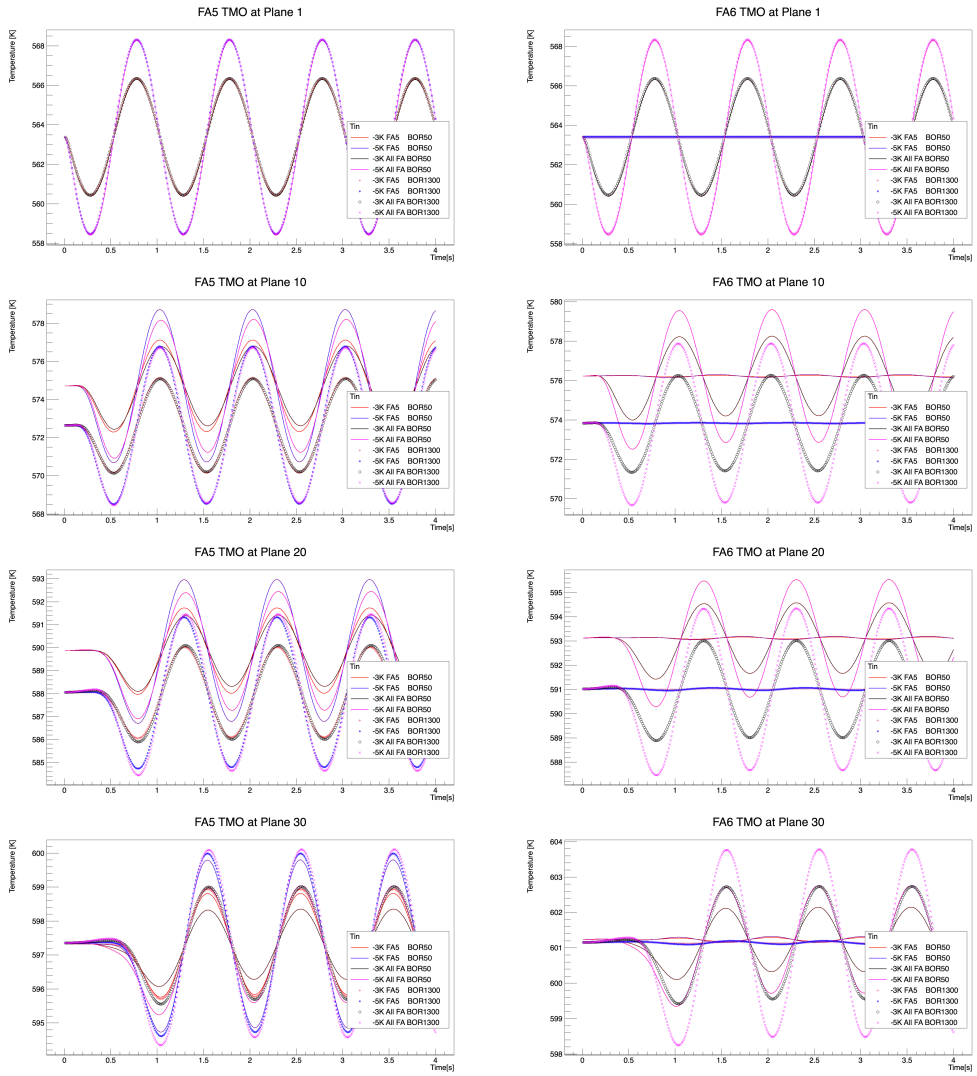

(a) (b)

Figure 6.17: TMO oscillation due to Tin ocillation with 3x3 FA model (CASMO XS, U-FA, BU: 0-10 MWd/kgHM).

In Fig. 6.19 the RPF oscillation amplitude of each plane is normalized to its initial value. This figures gives an impression of the oscillation amplitude detected by the detectors at different axial height. It is seen in both figures the power oscillation has a minimum amplitude at about the middle height (around plane 15). The power oscillation is generally smaller in "FA5" cases than in "All FA" cases, also smaller in BOR1300 cases compared to BOR50

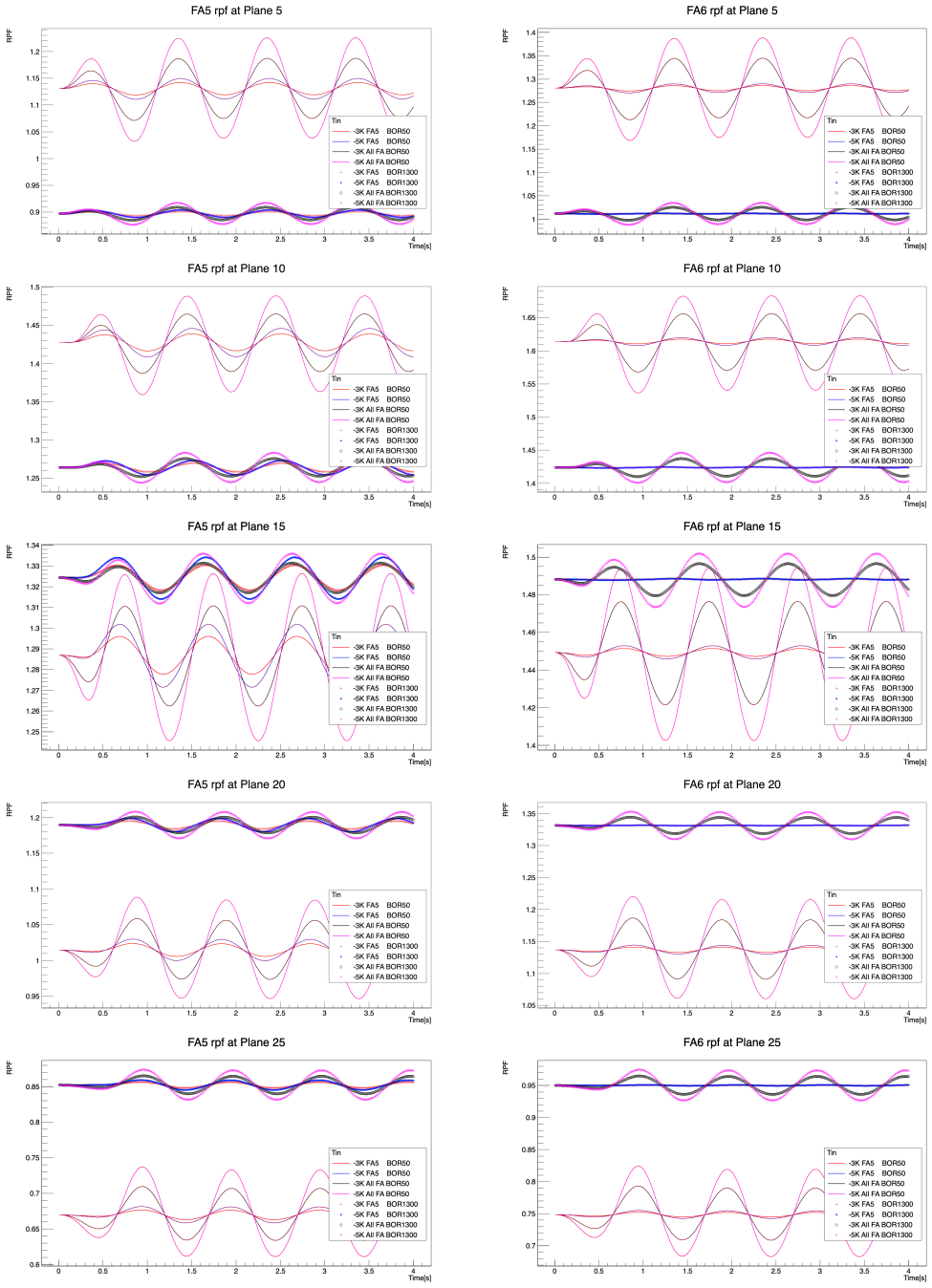

(a) (b)

Figure 6.18: RPF oscillation due to Tin oscillation with 3x3 FA model (CASMO XS, U-FA, BU: 0-10 MWd/kgHM).

cases. The maximum power oscillation can be found at the top and bottom nodes in the "ALL FA BOR50" cases with a value of around 10%.

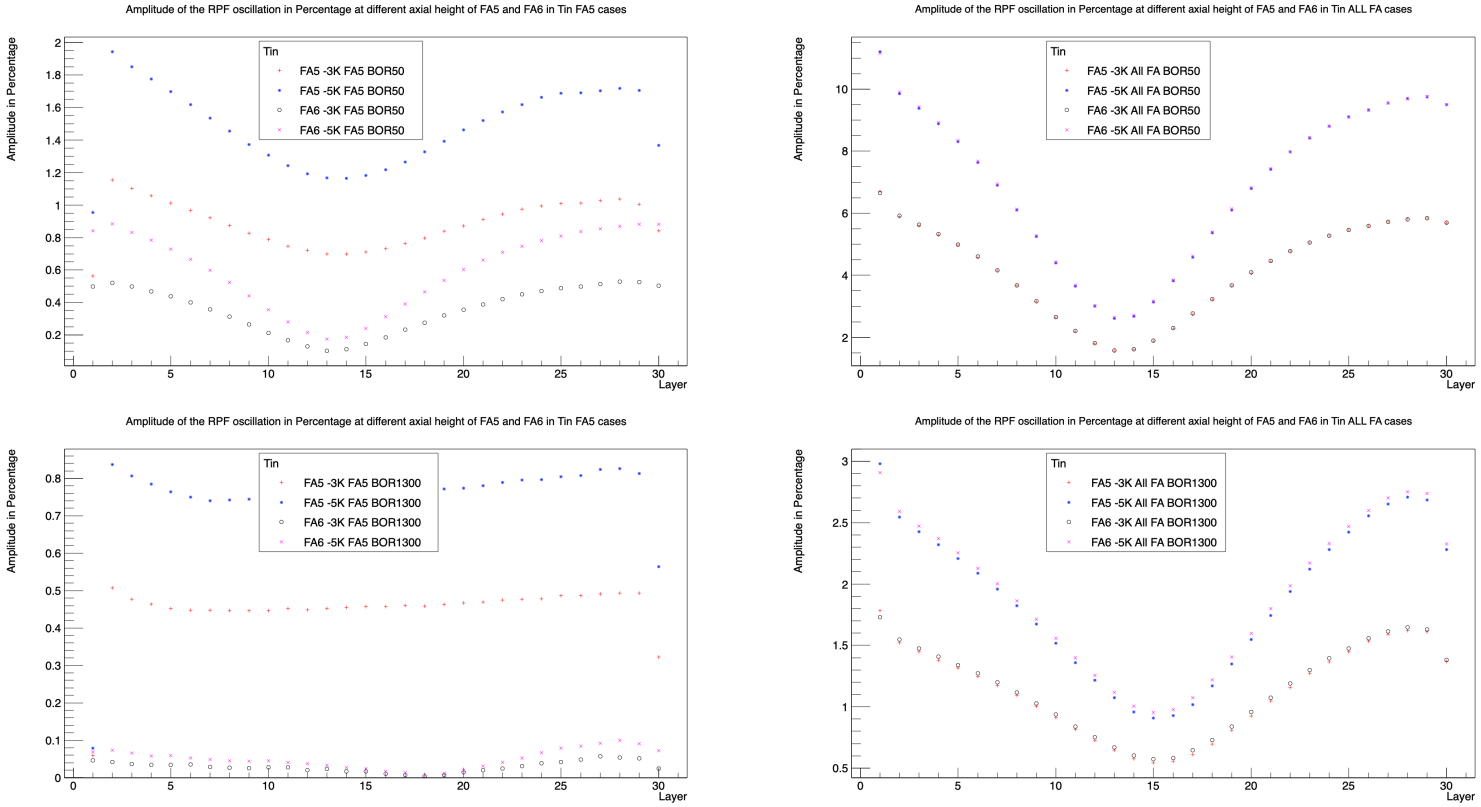

Figure 6.19: Percentage-wise amplitude of RPF oscillation with respect to its reference value at different axial height of FA5 and FA6 in Tin (left: FA5, right: ALL FA) cases (CASMO XS, U-FA, BU: 0-10 MWd/kgHM).

6.2.2.1.2.2 Vin cases

In Fig. 6.20 the TMO is shown for FA5 and FA6 with respect to different axial planes. Similar to what we have observed before in the SEPRENT cases, when the oscillating velocity (or mass flow) is only applied on one FA (FA5), the TMO oscillation effect will be reduced by the horizontal cross flow between FAs. In the Vin cases, the large difference between BOR50 and BOR1300 cases as in the Tin cases is not observed.

The neutronics response (RPF) also shows a oscillating behavior (shown in Fig. 6.21). In general the neutronics field is more sensitive to the velocity oscillation when the boron concentration is low (50ppm). When the mass flow increases at the FA inlet, the TMO starts to decrease on each plane of the FAs. From Fig. 6.20 it is seen the TMO oscillation is larger on the upper half of the FA (in "ALL FA" cases) causing a larger reactivity insertion on the upper half. Therefore at the beginning of the transient, the power decreases on the lower half while increasing on the upper half.

In Fig. 6.22 the RPF oscillation amplitude of each plane is normalized to its initial value. It is seen in both figures the power oscillation has a minimum amplitude at about the middle height (around plane 15). The power oscillation is generally smaller in "FA5" cases than in "All FA" cases, also smaller in BOR1300 cases compared to BOR50 cases. The maximum power oscillation can be found at the top and bottom nodes in the "ALL FA BOR50" cases with a value of around 5%.

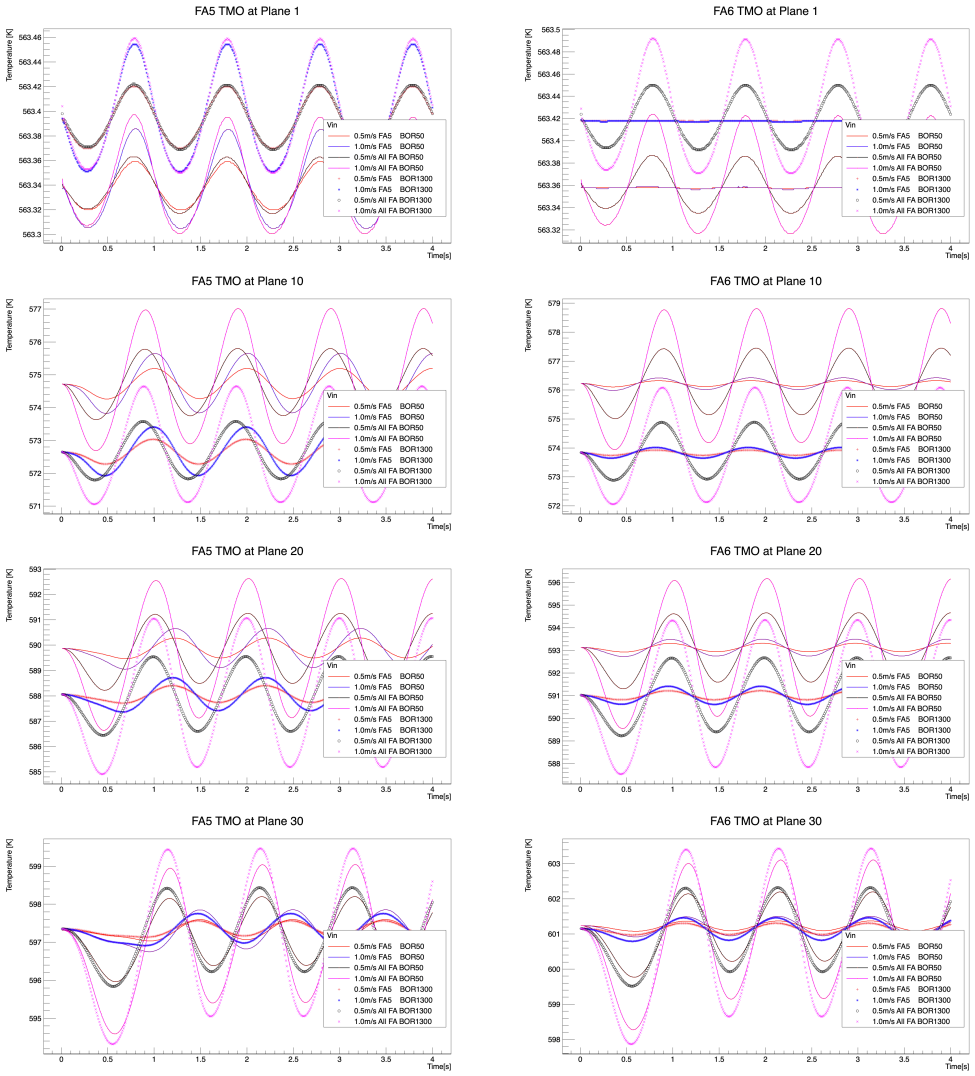

(a) (b)

Figure 6.20: TMO oscillation due to Vin oscillation with 3x3 FA model (CASMO XS, U-FA, BU: 0-10 MWd/kgHM).

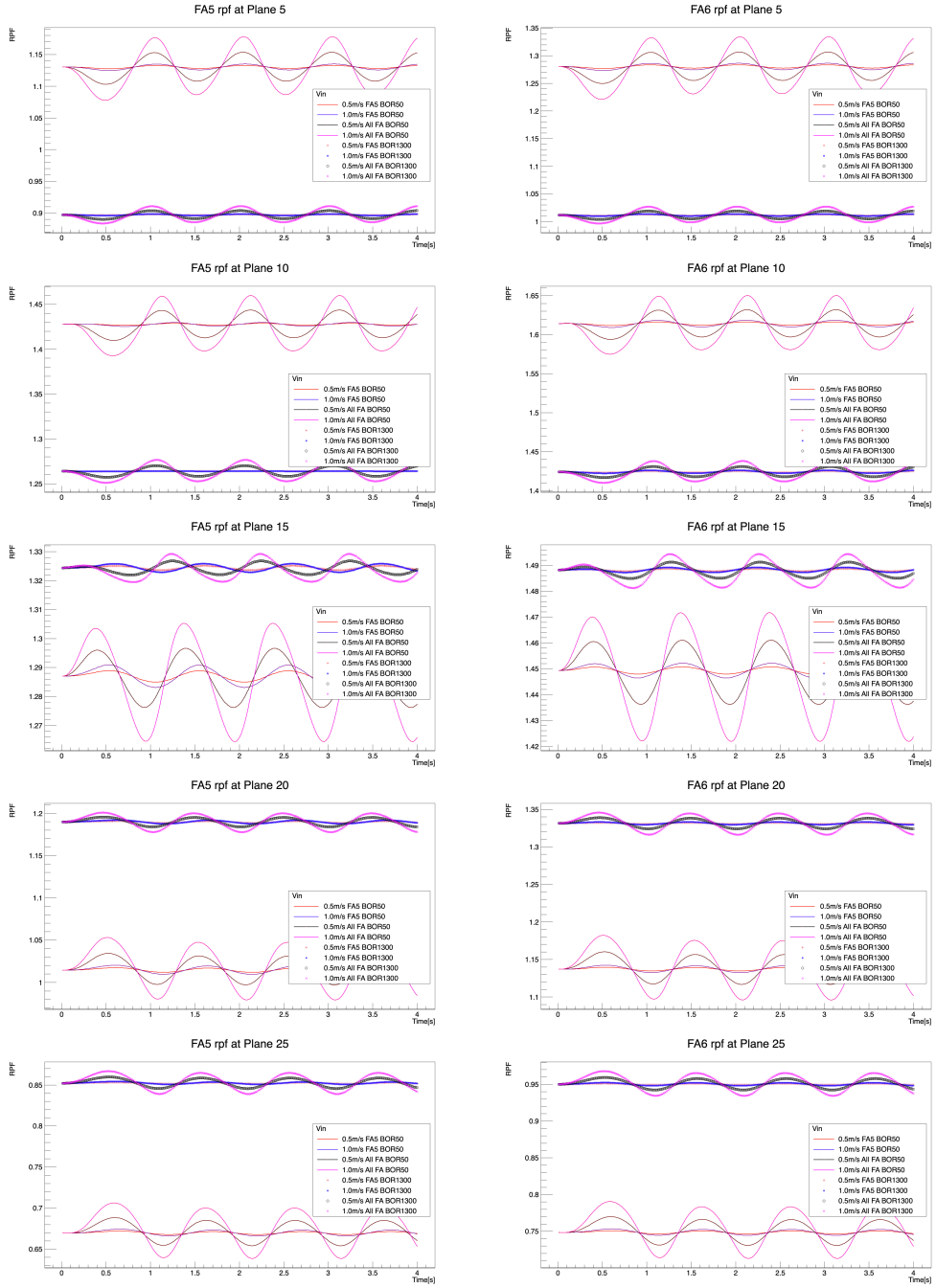

(a) (b)

Figure 6.21: RPF oscillation due to Vin oscillation with 3x3 FA model (CASMO XS, U-FA, BU: 0-10 MWd/kgHM).

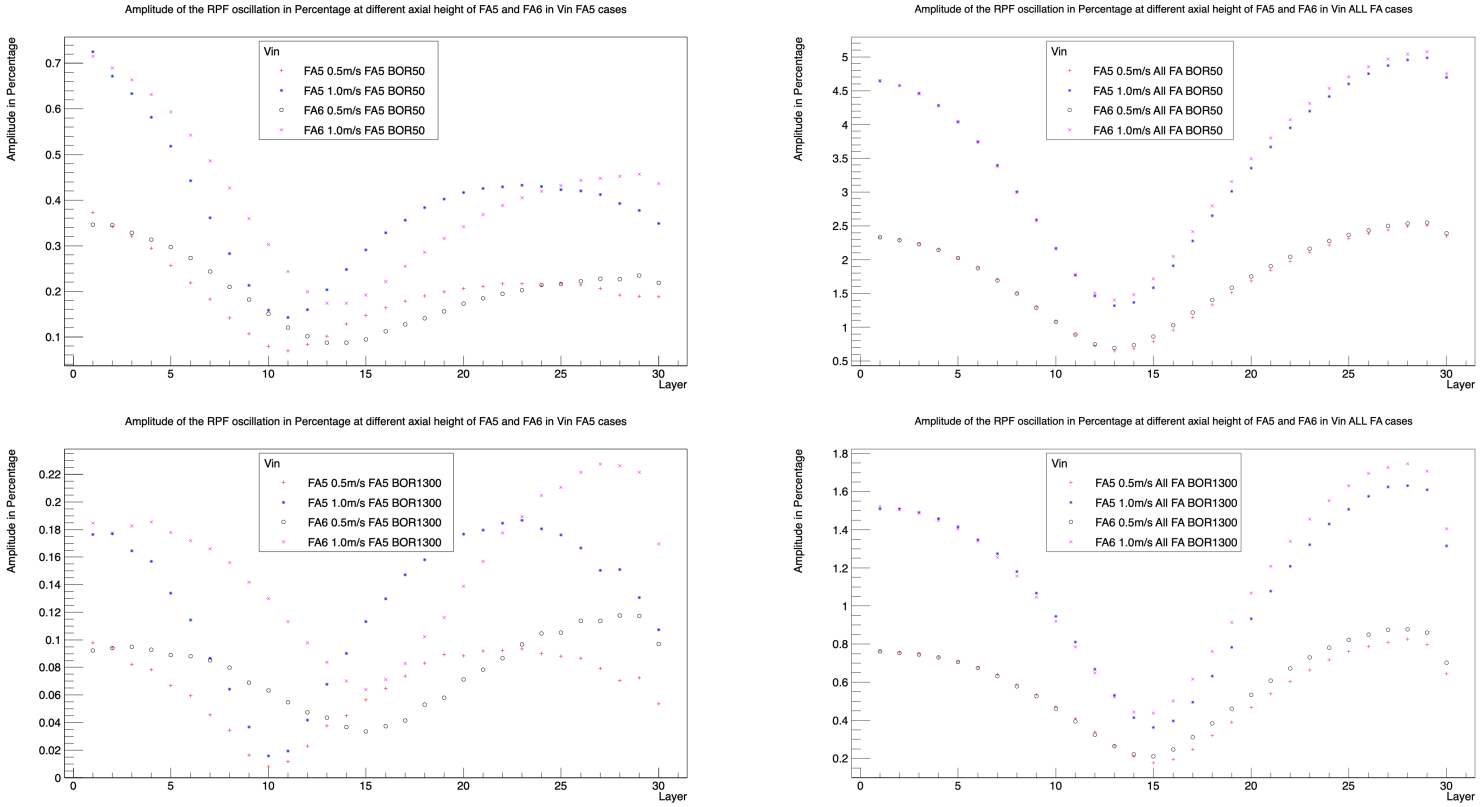

Figure 6.22: Percentage-wise amplitude of RPF oscillation with respect to its reference value at different axial height of FA5 and FA6 in Vin (left: FA5, right: ALL FA) cases (CASMO XS, U-FA, BU: 0-10 MWd/kgHM).

6.2.2.2 Burnup 10-30 MWd/kgHM

6.2.2.2.1 Steady-State Calculation

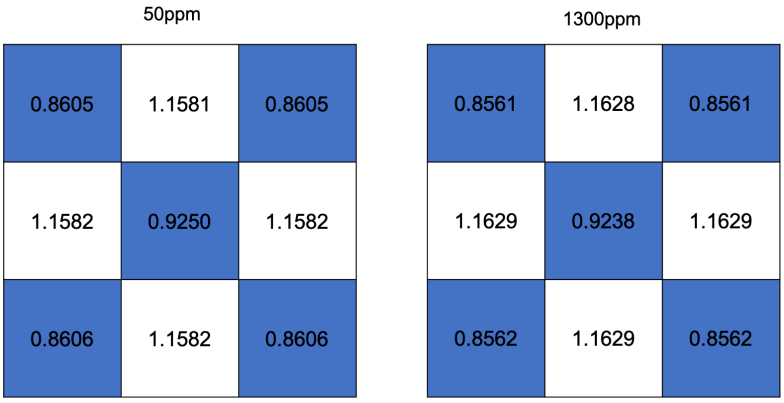

Figure 6.23: The radial RPF distribution of the steady state calculation with the 3x3 assembly model (CASMO XS, U-FA, BU: 10-30 MWd/kgHM): 50ppm case (left), 1300ppm case(right).

Fig. 6.23 depicts the radial power distribution of each FA with respect to different boron concentrations. Compared to the U-FA 0-10 MWd/kgHM case before (sec. 6.2.2.1.1), the RPF at the corner (which has a higher burnup) is around 10% smaller and the RPF on the side is around 10% larger.

Fig. 6.24 depicts the moderator temperature distributions and axial RPF distribution along the FA 3, 5 and 6. The outlet temperature is around 594K in FA3, 596K in FA5 and 603K in FA6. The maximum RPF can be found in FA6 with a value of 1.8 in the BOR50ppm case and 1.64 in the BOR1300ppm case respectively.

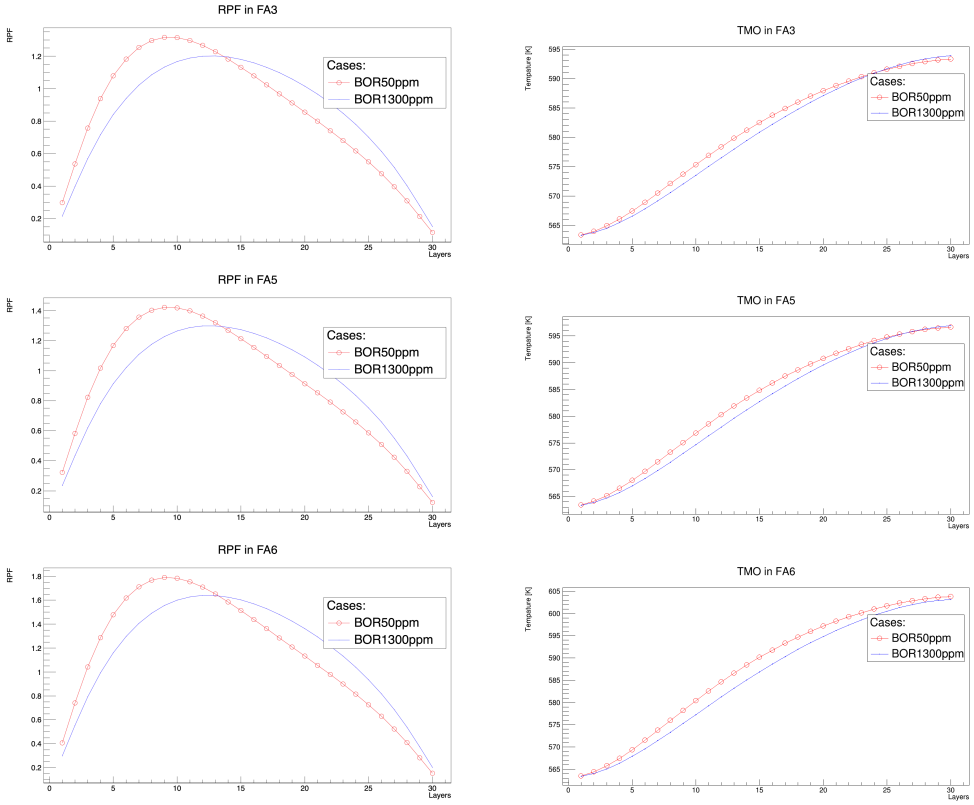

Figure 6.24: The axial RPF and TMO distribution in the steady state calculation with the 3x3 fuel assembly model (CASMO XS, U-FA, BU: 10-30 MWd/kgHM).

6.2.2.2.2 Transient cases

6.2.2.2.2.1 Tin cases

In Fig. 6.25 the TMO is shown for FA5 and FA6 with respect to different axial planes. In all cases, the TMO oscillation amplitude decreases with an increasing axial height. Depending on the cases, with an inlet temperature oscillation of 5K the outlet temperature oscillation can range from 2-3K while with an inlet temperature oscillation of 3K the temperature oscillation at the outlet is reduced to 1-1.5K. It is also seen in the BOR50 cases, the TMO oscillation is smaller in the "ALL FA" cases than in the "FA5" cases, which is not observed in the BOR1300 cases. This behavior is similar to the U-FA Tin cases which is explained in sec. 6.2.2.1.2.1.

The neutronics response (RPF) also shows a oscillating behavior (shown in Fig. 6.26). In general the neutronics field is more sensitive to the temperature oscillation when the boron concentration is low (50ppm). When the inlet temperature decreases the positive reactivity causes the RPF at the bottom half of the FA to increase and on the contrary at the upper half to decrease. The increasing power at the bottom half also minimizes the temperature oscillation. Since the RPF oscillation is higher in the "ALL FA" cases compared to the "FA5 case", the TMO oscillation is more compensated in the "ALL FA" cases. On the other hand, when the the "cold" moderator travels to the upper part the induced increasing power in the upper half will continue minimizing the temperature oscillation. As a result, the temperature oscillation of FA5 in the "ALL FA" cases is smaller compared to the "FA5" cases (when the TMO oscillation amplitude is the same).

In Fig. 6.27 the RPF oscillation amplitude of each plane is normalized to its initial value. It is seen in both figures the power oscillation has a minimum amplitude at about the middle height (around plane 15). The power oscilla-

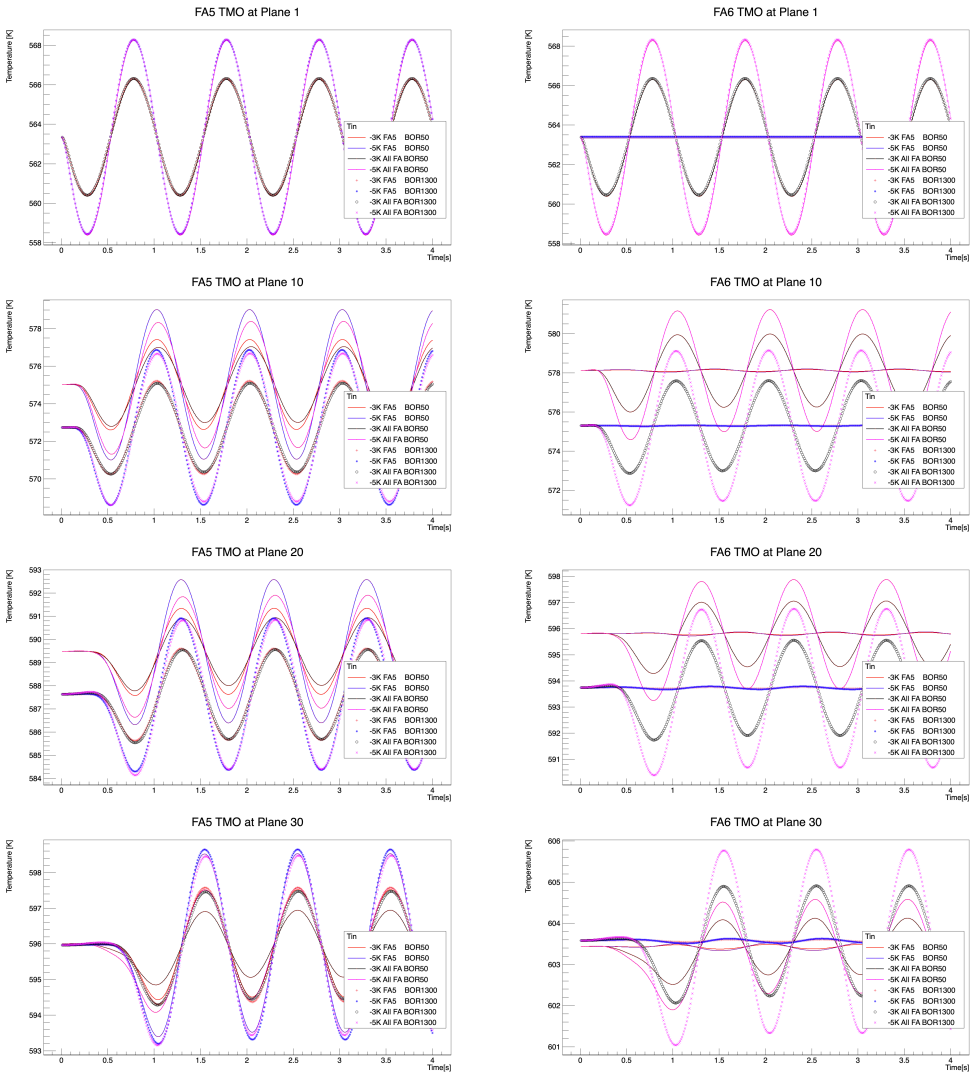

(a) (b)

Figure 6.25: TMO oscillation due to Tin ocillation with 3x3 FA model (CASMO XS, U-FA, BU: 10-30 MWd/kgHM).

tion is generally smaller in "FA5" cases than in "All FA" cases, also smaller in BOR1300 cases compared to BOR50 cases. Compared to the previous investigation with U-FA 0-10 MWd/kg the relative power oscillation is quite comparable. The maximum value can be found at top and bottom of the fuel assembly. The absolute amplitude is slightly higher in the "ALL FA" cases (10-30 MWd/kgHM). But in general the power and temperature oscillation

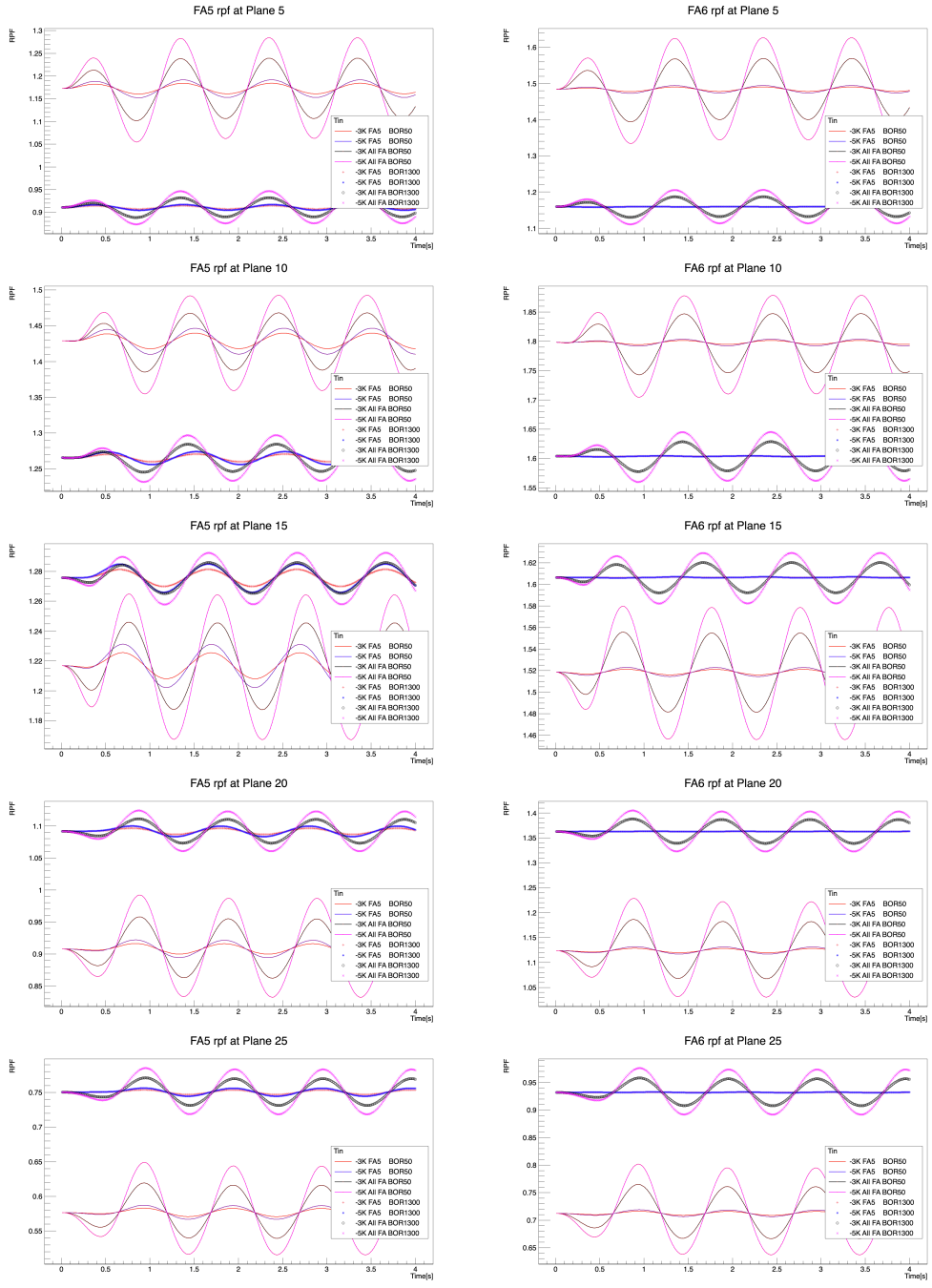

(a) (b)

Figure 6.26: RPF oscillation due to Tin oscillation with 3x3 FA model (CASMO XS, U-FA, BU: 10-30 MWd/kgHM).

amplitudes are similar between two burnup sets.

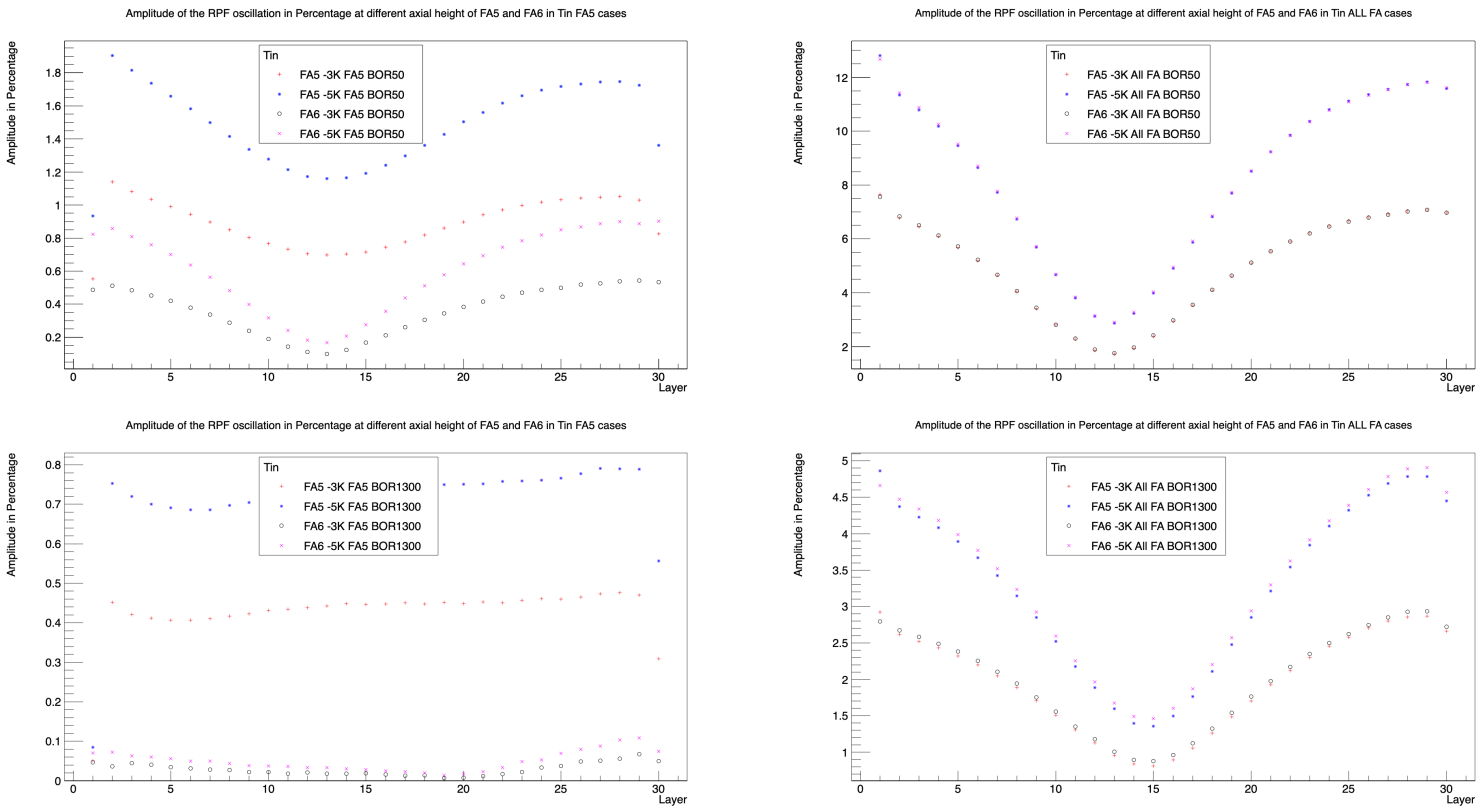

Figure 6.27: Percentage-wise amplitude of RPF oscillation with respect to its reference value at different axial height of FA5 and FA6 in Tin (left: FA5, right: ALL FA) cases (CASMO XS, U-FA, BU: 10-30 MWd/kgHM).

6.2.2.2.2.2 Vin cases

In Fig. 6.28 the TMO is shown for FA5 and FA6 with respect to different axial planes. The oscillation behavior is quite similar to what we have observed in U-FA 0-10 MWd/kgHM cases (s. sec. 6.2.2.1.2.2).

The neutronics response (RPF) is shown in Fig. 6.29. The oscillation behavior is quite similar to the U-FA 0-10 MWd/kgHM (s. sec. 6.2.2.1.2.2) featuring a higher oscillation amplitude in the 50ppm cases. The reason has already been explained in sec. 6.2.2.1.2.2.

In Fig. 6.30 the RPF oscillation amplitude of each plane is normalized to its initial value. Despite of the similarities of the oscillation behavior, the maximum oscillation amplitude is slightly higher (6% in the "ALL FA BOR50" case) than in the U-FA 0-10 MWd/kgHM cases (around 5% in the "ALL FA BOR50" case), which is consistent with the observation in the Tin cases (s. sec. 6.2.2.2.2.1).

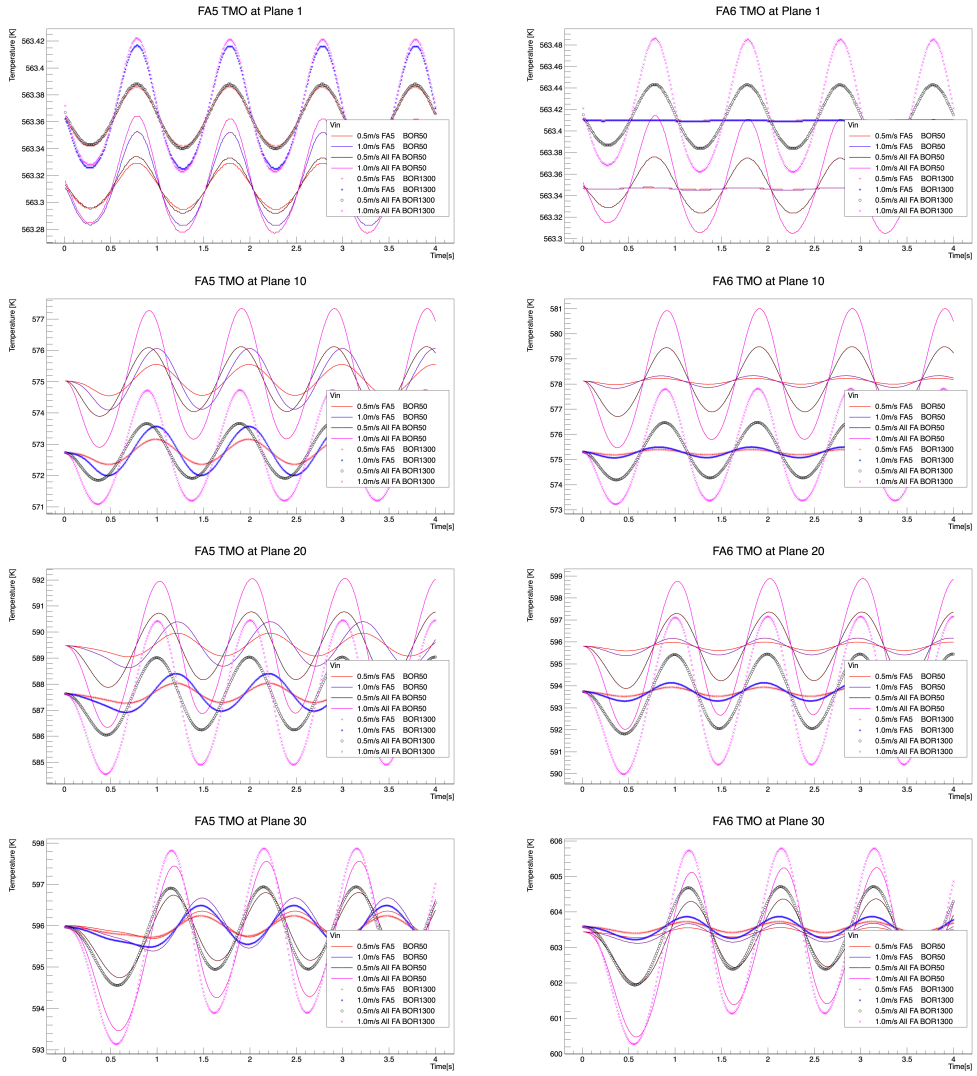

(a) (b)

Figure 6.28: TMO oscillation due to Vin oscillation with 3x3 FA model (CASMO XS, U-FA, BU: 10-30 MWd/kgHM).

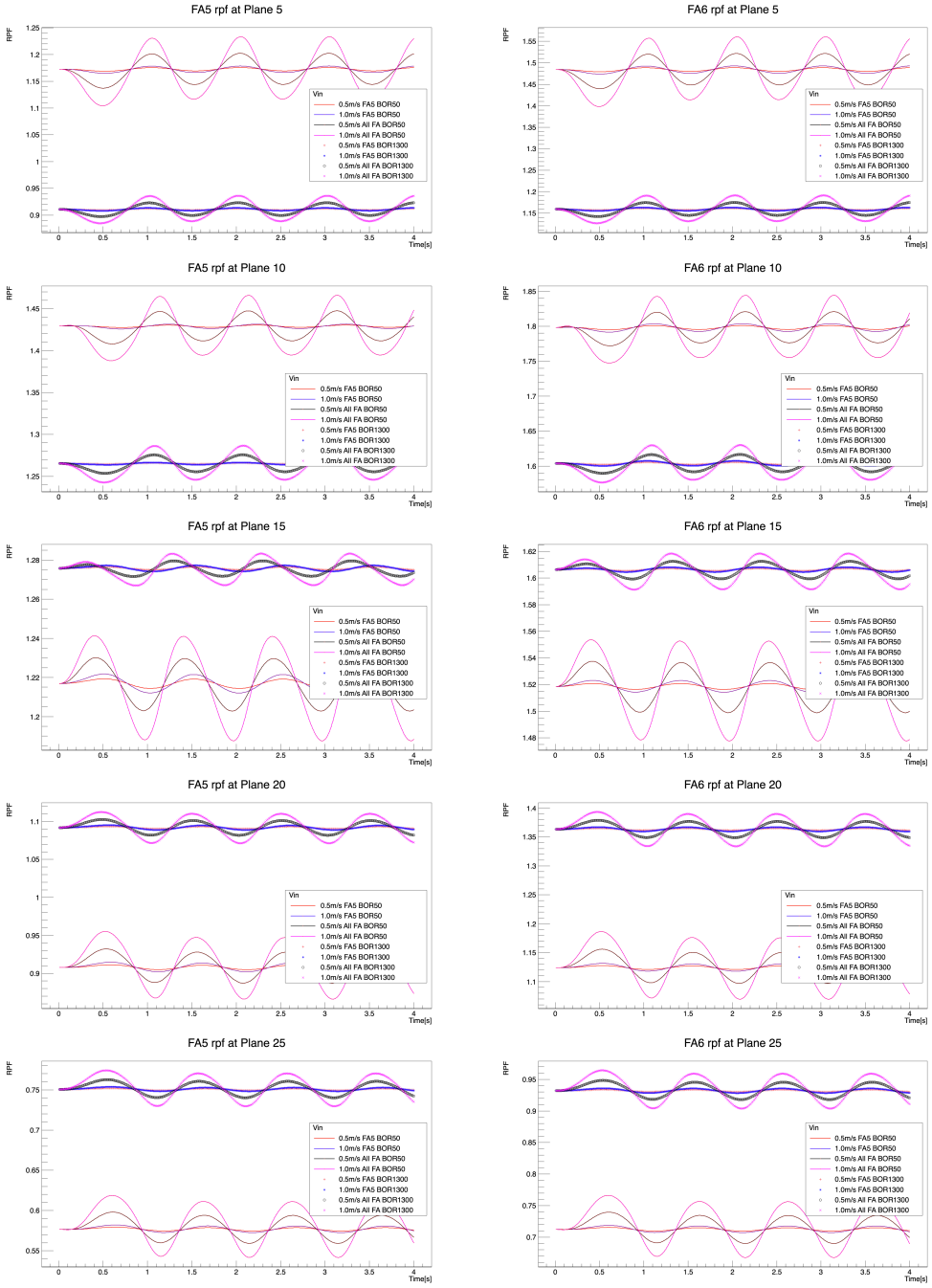

(a) (b)

Figure 6.29: RPF oscillation due to Vin oscillation with 3x3 FA model (CASMO XS, U-FA, BU: 10-30 MWd/kgHM).

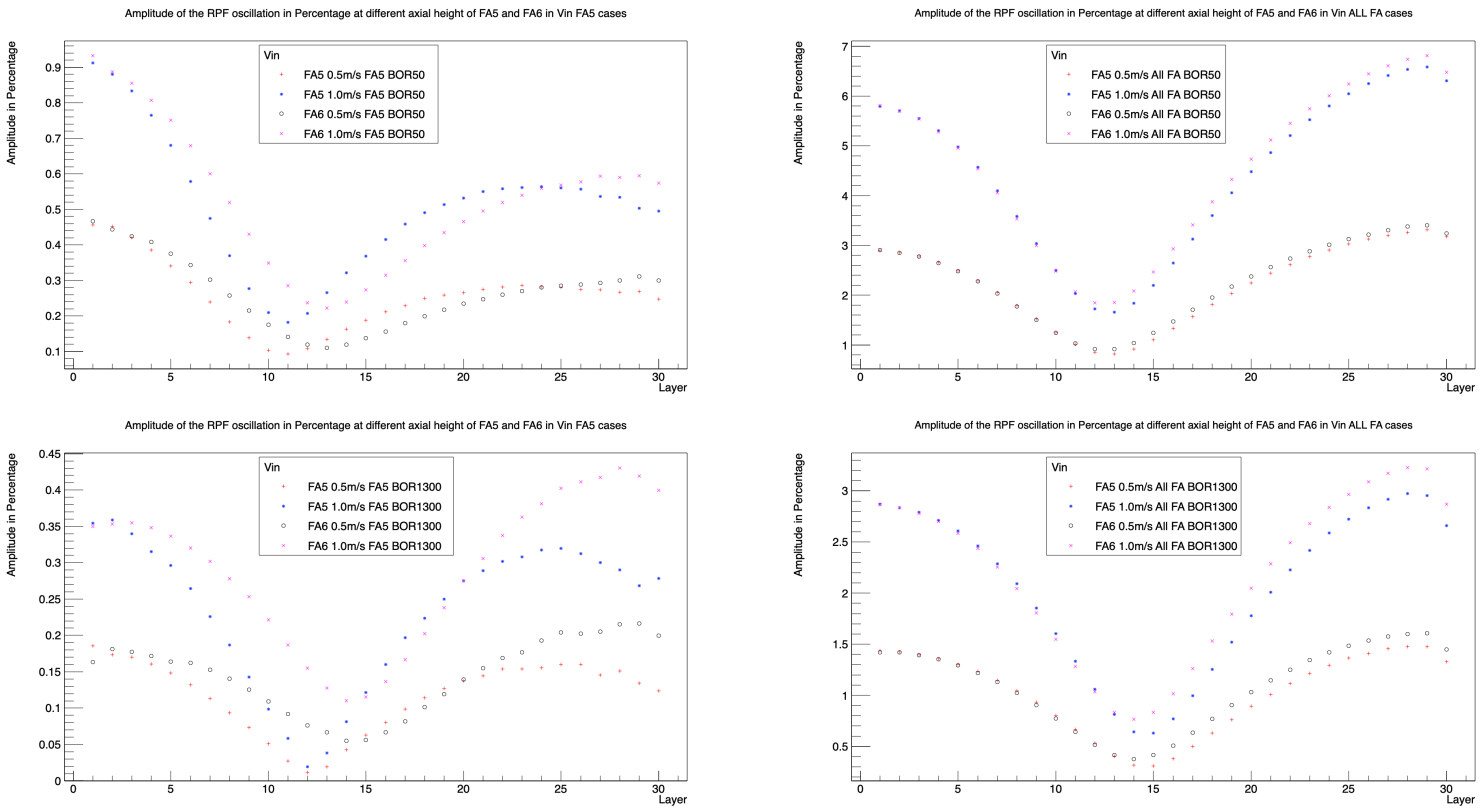

Figure 6.30: Percentage-wise amplitude of RPF oscillation with respect to its reference value at different axial height of FA5 and FA6 in Vin (left: FA5, right: ALL FA) cases (CASMO XS, U-FA, BU: 10-30 MWd/kgHM).

6.2.3 U-MOX-FA Cases

6.2.3.1 Burnup 0-10 MWd/kgHM

6.2.3.1.1 Steady-State calculation

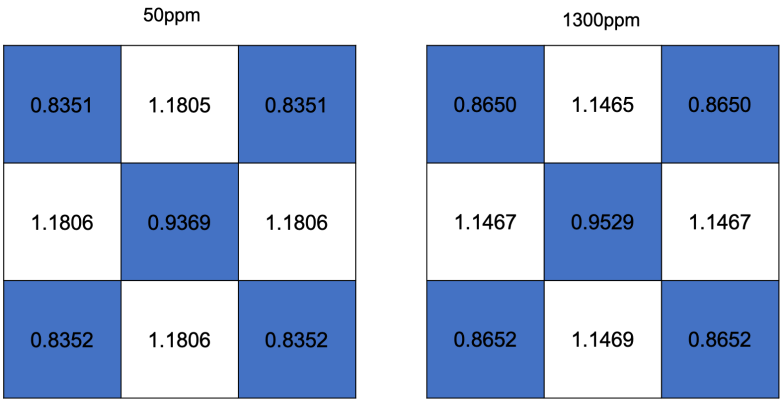

Figure 6.31: The radial RPF distribution of the steady state calculation with the 3x3 assembly model (CASMO XS, U-MOX-FA, BU: 0-10 MWd/kgHM): 50ppm case (left), 1300ppm case(right).

Fig. 6.31 depicts the radial power distribution of each FA with respect to different boron concentrations. Compared to the cases with only U-FA at presence (s. sec. 6.2.2.1.1), the power fraction distribution shows a lower power fraction in the corner MOX-FA (0.8351-0.8650) and a higher power fraction in the side U-FA (1.1465-1.1805). This behavior also reflects that this MOX-FA has a lower reactivity than the U-FA with the same burnup (10 MWd/kgHM).

Fig. 6.32 depicts the moderator temperature distributions along the FA 3, 5 and 6. The outlet temperature is around 594K in FA3, 597K in FA5 and 603K in FA6. In Fig. 6.32 the RPF is plotted for each planes in FA3, FA5 and FA6. The maximum RPF can be found in FA6 with a value of 1.8 in the BOR50ppm case and 1.6 in the BOR1300ppm case respectively.

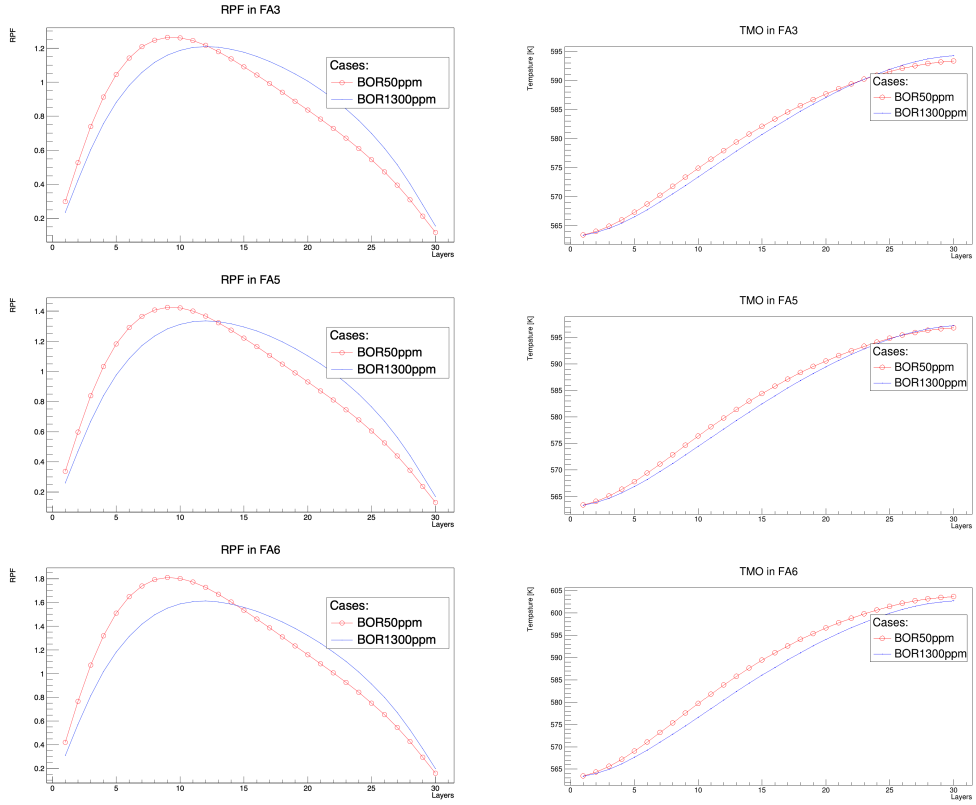

Figure 6.32: The axial RPF and TMO distribution in the steady state calculation with the 3x3 fuel assembly model (CASMO XS, U-MOX-FA, BU: 0-10 MWd/kgHM).

6.2.3.1.2 Transient cases

6.2.3.1.2.1 Tin cases

In Fig. 6.33 the TMO is shown for FA5 and FA6 with respect to different axial planes. As previously described, the temperature oscillation amplitude decreases with an increasing axial height. It can also be seen that due to different neutronic feedback between "FA5" and "ALL FA" cases the TMO oscillation shows a different amplitude between these two series although the inlet oscillation amplitude is the same (when looking at the TMO oscillation in FA5). On layer 30 in FA5, the TMO starts to drop faster in the "ALL FA BOR50" cases than in the "FA5 BOR50" cases however resulting in a smaller oscillation amplitude. The same behavior can also be observed in the BOR1300 cases but the difference is smaller.

The neutronics response (RPF) also shows a oscillating behavior (shown in Fig. 6.34). In general the neutronics field is more sensitive to the temperature oscillation when the boron concentration is low (50ppm).

In Fig. 6.35 the RPF oscillation amplitude of each plane is normalized to its initial value. The power oscillation is generally smaller in "FA5" cases than in "All FA" cases, also smaller in BOR1300 cases compared to BOR50 cases. The maximum power oscillation can be found at the top and bottom nodes in the "ALL FA BOR50" cases with a value of around 12%.

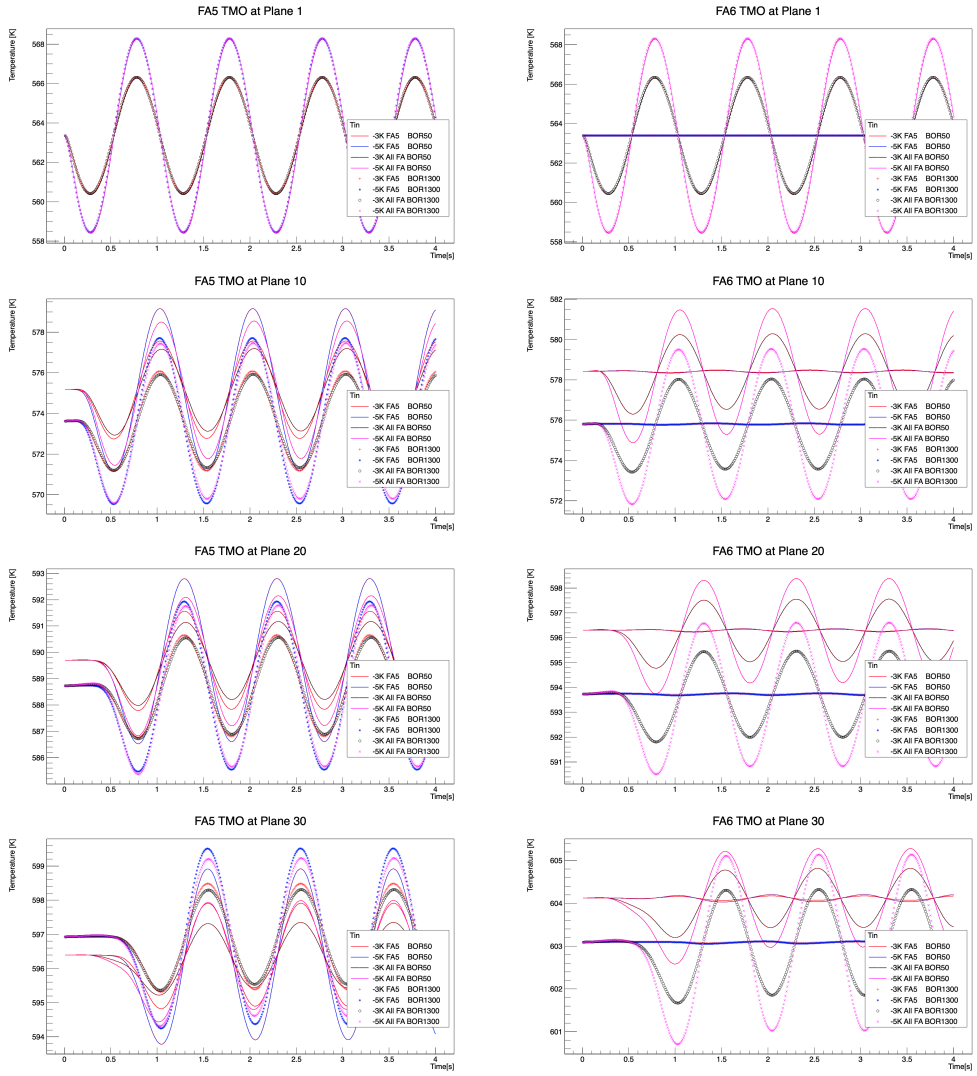

(a) (b)

Figure 6.33: TMO oscillation due to Tin oscillation with 3x3 FA model (CASMO XS, U-MOX-FA, BU: 0-10 MWd/kgHM).

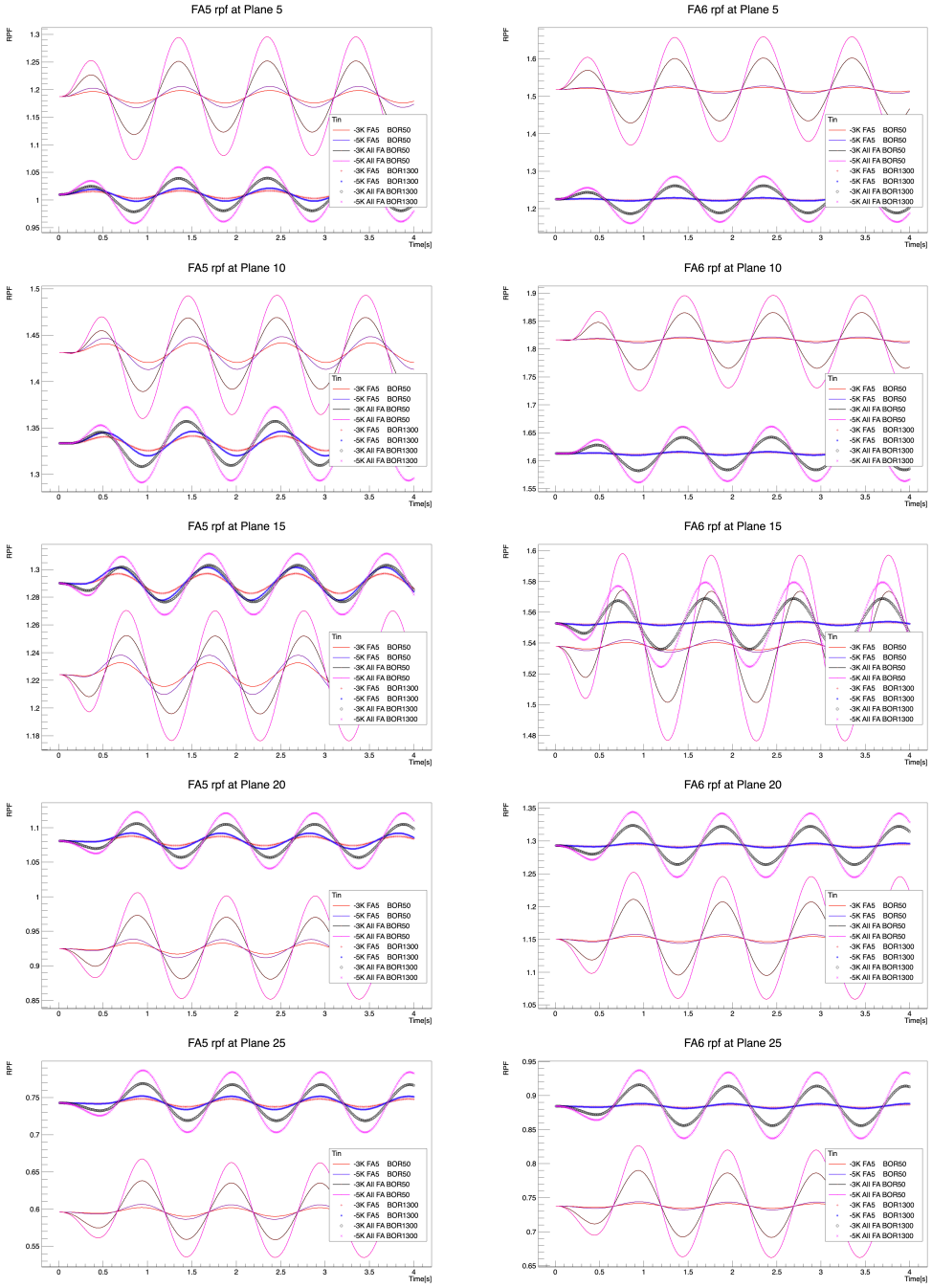

(a) (b)

Figure 6.34: RPF oscillation due to Tin ocillation with 3x3 FA model (CASMO XS, U-MOX-FA, BU: 0-10 MWd/kgHM).

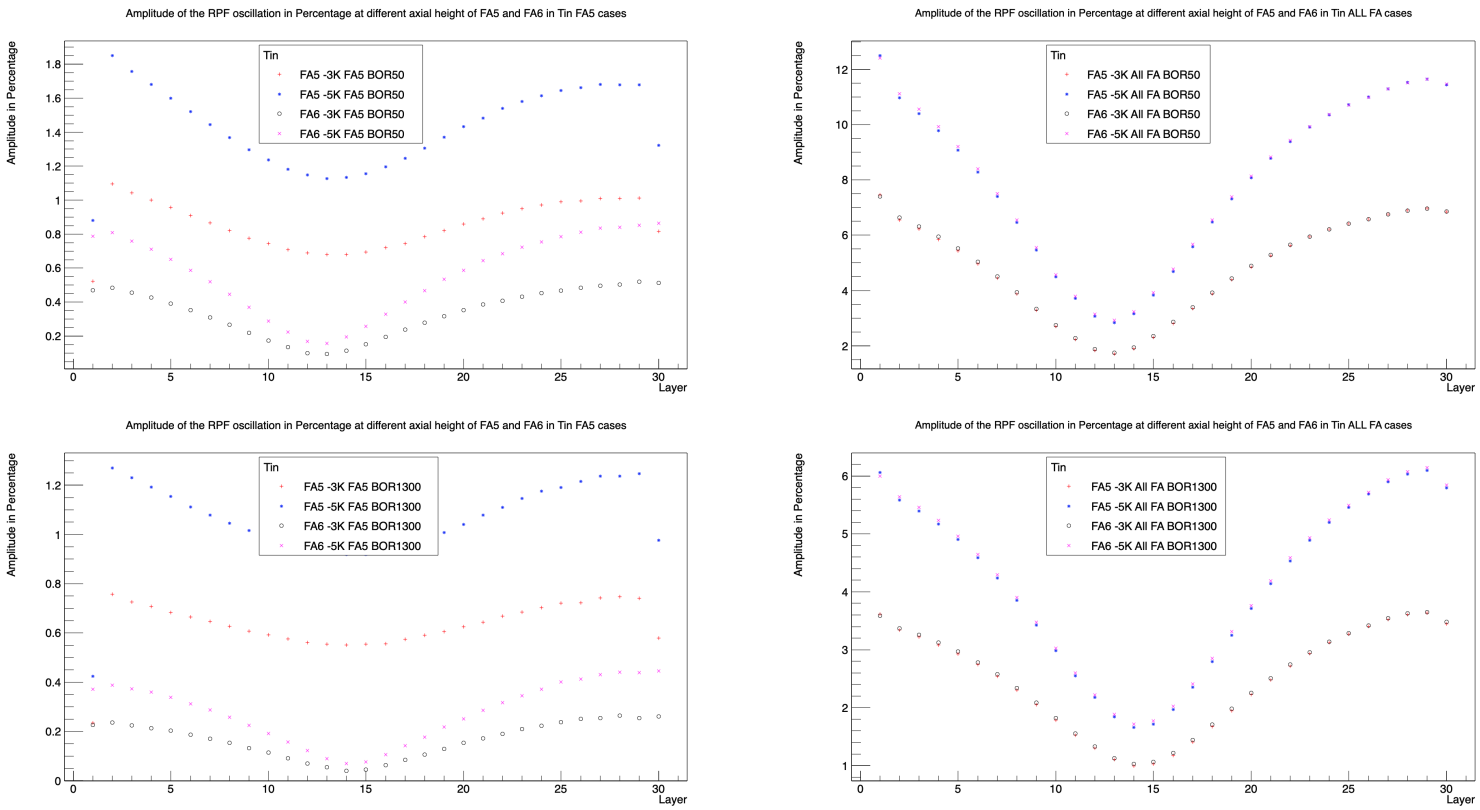

Figure 6.35: Percentage-wise amplitude of RPF oscillation with respect to its reference value at different axial height of FA5 and FA6 in Tin (left: FA5, right: ALL FA) cases (CASMO XS, U-MOX-FA, BU: 0-10 MWd/kgHM).

6.2.3.1.2.2 Vin cases

In Fig. 6.36 the TMO is shown for FA5 and FA6 with respect to different axial planes. In both BOR50 and BOR1300 cases, the temperature oscillation shows a similar behavior. The maximum oscillation amplitude is around 2K.

The neutronics response (RPF) also shows a oscillating behavior (shown in Fig. 6.37). Although the TMO oscillation figure shows a similar behavior in the BOR50 and BOR1300 cases, the RPF oscillation shows a larger amplitude in the BOR50 than in the BOR1300 cases.

In Fig. 6.38 the RPF oscillation amplitude of each plane is normalized to its initial value. It is seen in both figures the power oscillation has a minimum amplitude at about the middle height (around plane 13). The power oscillation is generally smaller in "FA5" cases than in "All FA" cases, also smaller in BOR1300 cases compared to BOR50 cases. The maximum power oscillation can be found at the top and bottom nodes in the "ALL FA BOR50" cases with a value of around 6-7%.

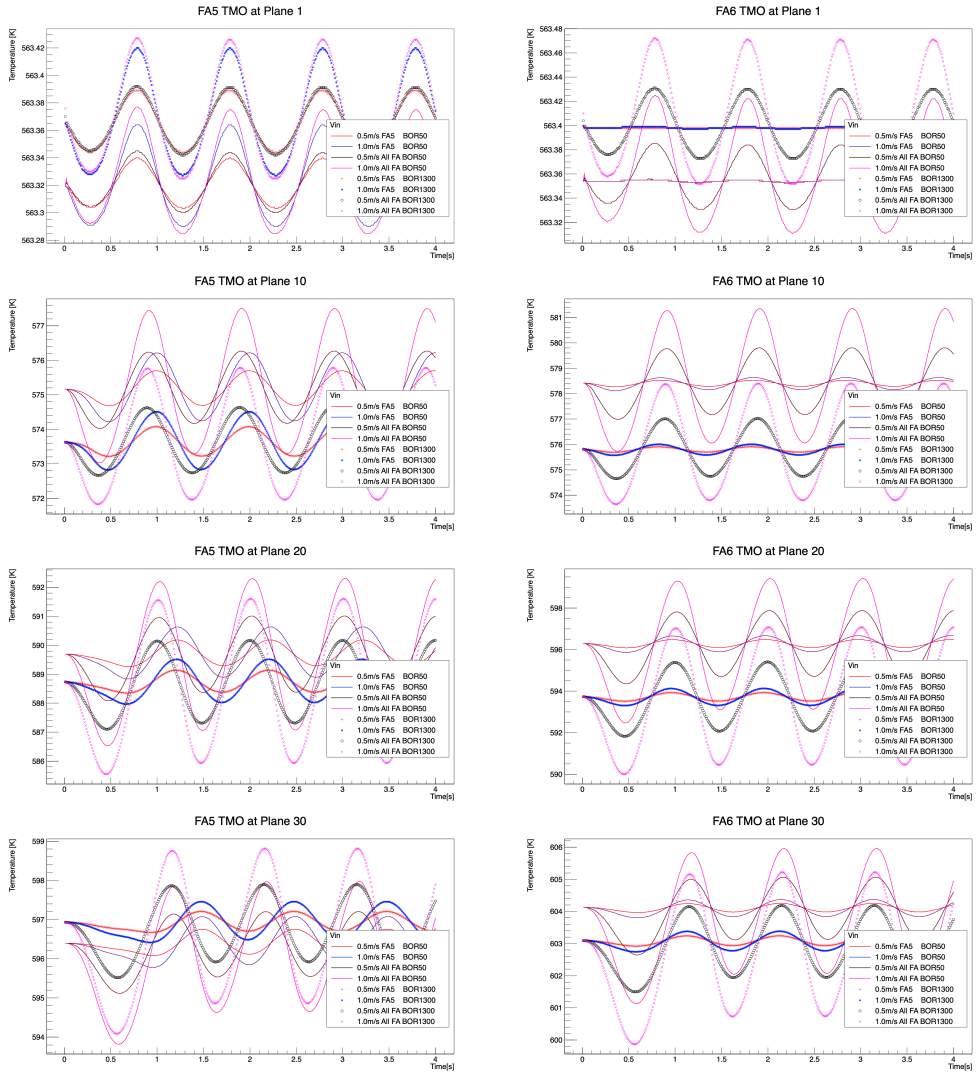

(a) (b)

Figure 6.36: TMO oscillation due to Vin oscillation with 3x3 FA model (CASMO XS, U-MOX-FA, BU: 0-10 MWd/kgHM).

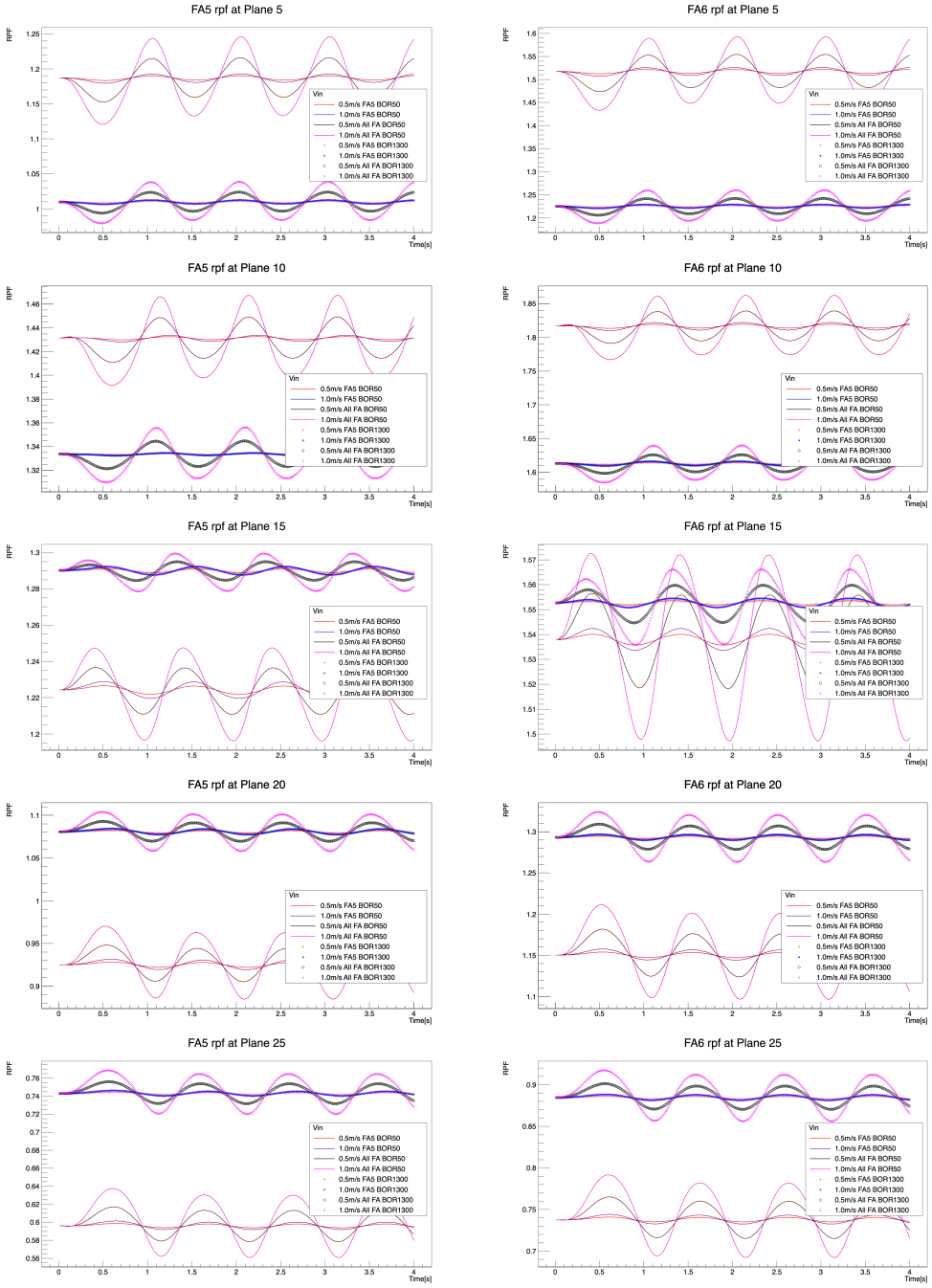

(a) (b)

Figure 6.37: RPF oscillation due to Vin oscillation with 3x3 FA model (CASMO XS, U-MOX-FA, BU: 0-10 MWd/kgHM).

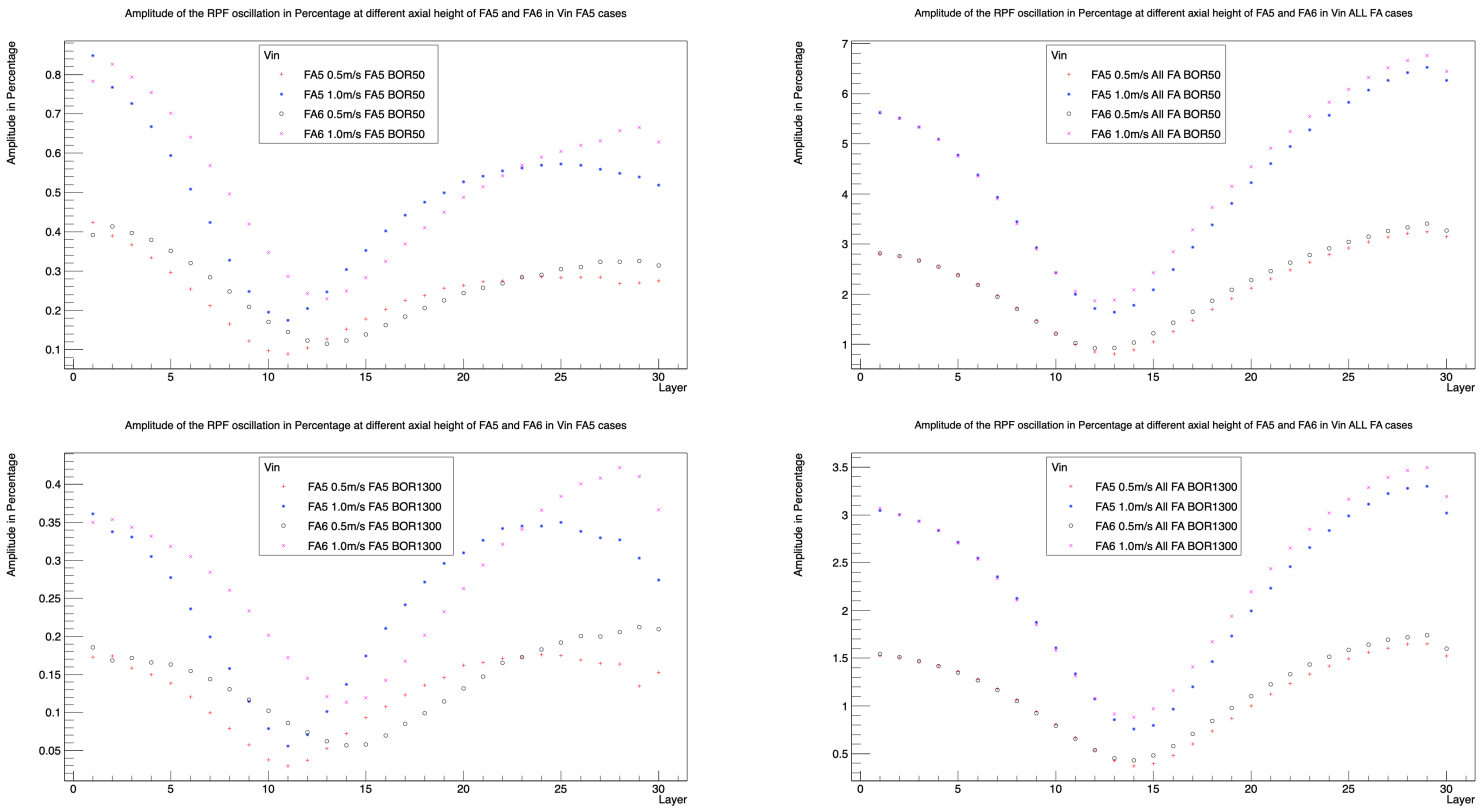

Figure 6.38: Percentage-wise amplitude of RPF oscillation with respect to its reference value at different axial height of FA5 and FA6 in Vin (left: FA5, right: ALL FA) cases (CASMO XS, U-MOX-FA, BU: 0-10 MWd/kgHM).

6.2.3.2 Burnup 10-30 MWd/kgHM

6.2.3.2.1 Steady-State calculation

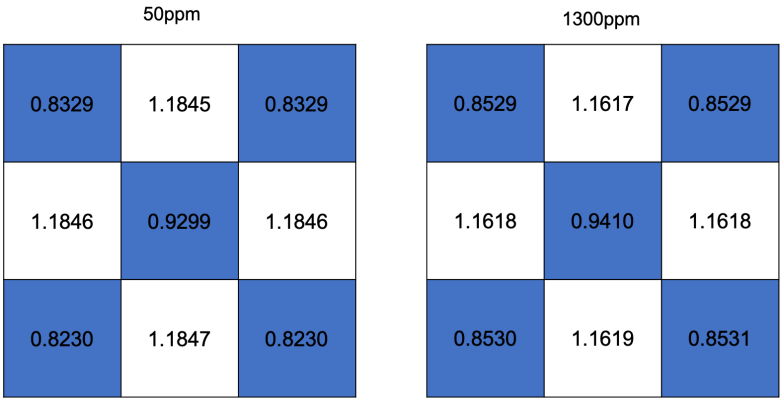

Figure 6.39: The radial RPF distribution of the steady state calculation with the 3x3 assembly model (CASMO XS, U-MOX-FA, BU: 10-30 MWd/kgHM): 50ppm case (left), 1300ppm case(right).

Fig. 6.39 depicts the radial power distribution of each FA with respect to different boron concentrations. Compared to the U-MOX-FA 0-10 MWd/kgHM case before (sec. 6.2.3.1.1), the RPF has a similar distribution which is different to the observation when comparing the RPF distribution in the U-FA cases with different burnup compositions (s. in Fig. 6.15 and 6.23).

Fig. 6.40 depicts the moderator temperature distributions and axial RPF distribution along the FA 3, 5 and 6. The outlet temperature is around 594K in FA3, 596K in FA5 and 604K in FA6. The maximum RPF can be found in FA6 with a value of 1.85 in the BOR50ppm case and 1.6 in the BOR1300ppm case respectively.

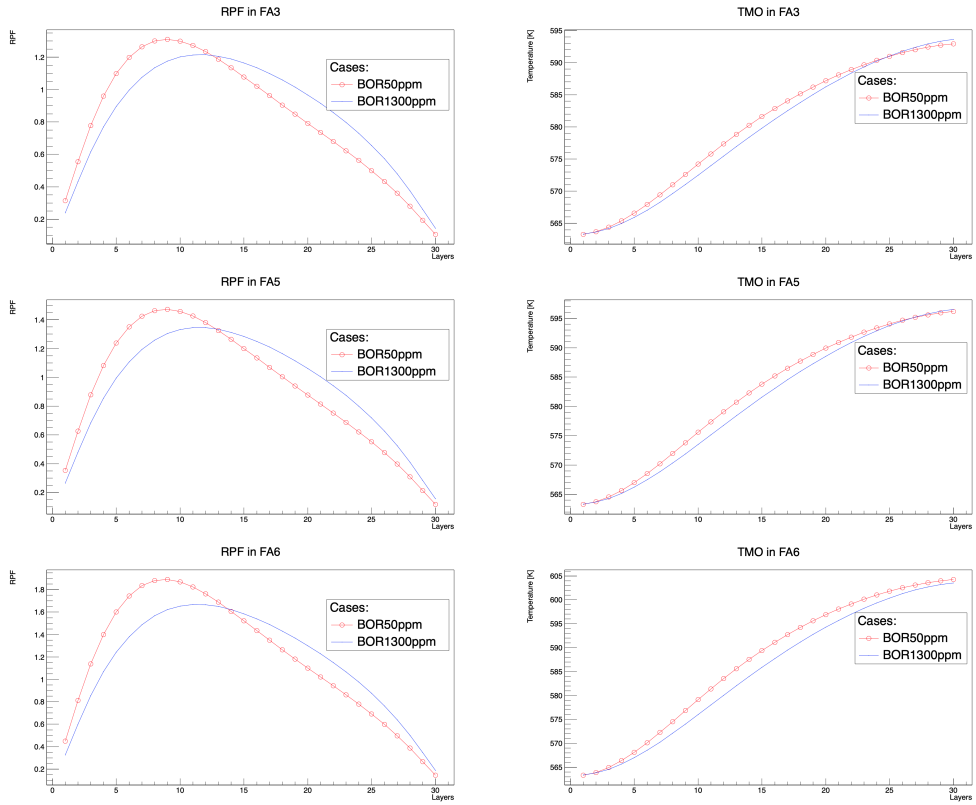

Figure 6.40: The axial RPF and TMO distribution in the steady state calculation with the 3x3 fuel assembly model (CASMO XS, U-MOX-FA, BU: 10-30 MWd/kgHM).

6.2.3.2.2 Transient cases

6.2.3.2.2.1 Tin cases

In Fig. 6.41 the TMO is shown for FA5 and FA6 with respect to different axial planes. In all cases, the TMO oscillation amplitude decreases with an increasing axial height. Depending on the cases, with an inlet temperature oscillation of 5K the outlet temperature oscillation can range from 1.5-2.5K while with an inlet temperature oscillation of 3K the temperature oscillation at the outlet is reduced to 0.8-1.5K. It is also seen in the BOR50 cases, the TMO oscillation is smaller in the "ALL FA" cases than in the "FA5" cases, which is not observed in the BOR1300 cases. This behavior is similar to the U-MOX-FA Tin cases.

The neutronics response (RPF) also shows a oscillating behavior (shown in Fig. 6.42). Similar to other cases, the neutronics oscillation has a higher amplitude in the BOR50 cases than in the BOR1300 cases given the same inlet oscillation boundary condition.

In Fig. 6.43 the RPF oscillation amplitude of each plane is normalized to its initial value. Compared to the previous investigation with U-MOX-FA 0-10 MWd/kgHM case the relative power oscillation behavior is quite similar. The maximum value can be found at top and bottom of the fuel assembly with a maximal value of around 13.5% (in the -5K ALL FA BOR50 case) which is slightly higher than the maximal power oscillation amplitude in the U-MOX-FA 0-10 MWd/kgHM cases (around 12% in sec. 6.2.3.1.2.1).

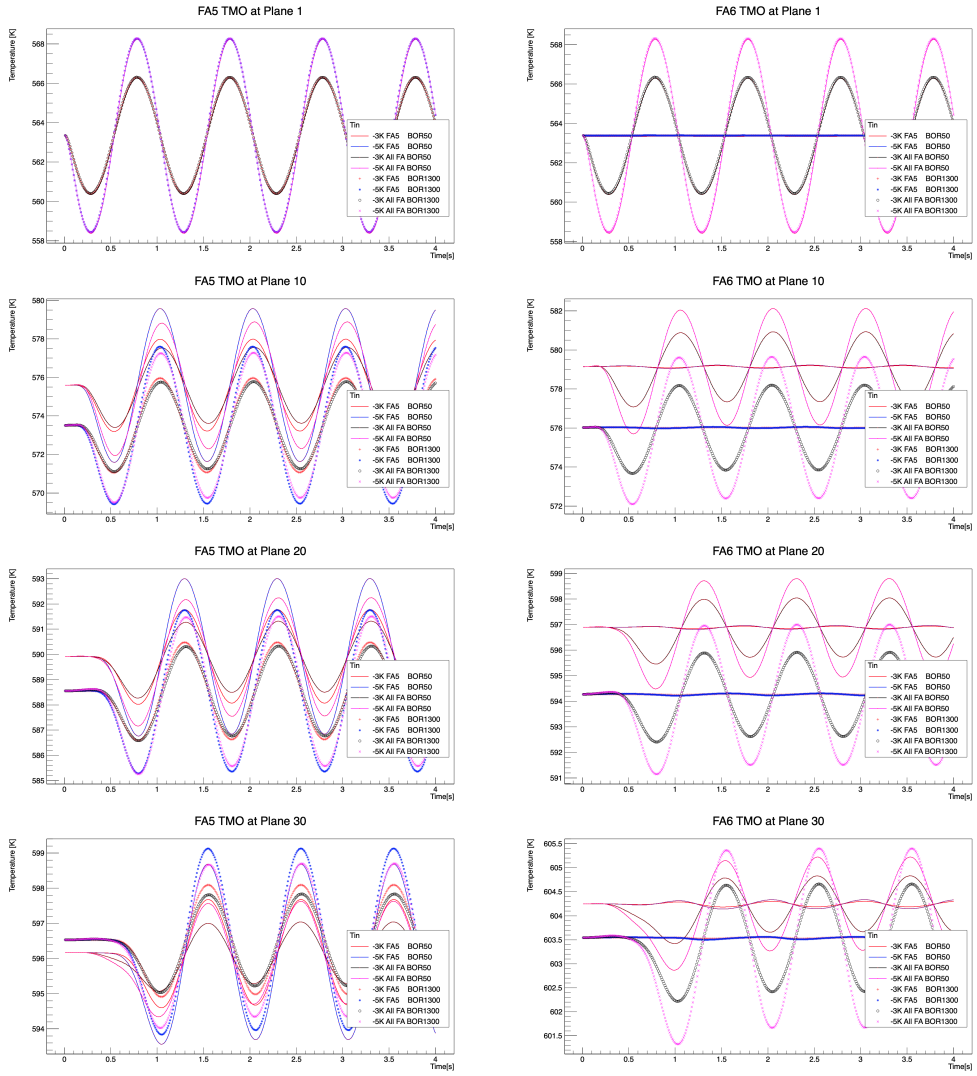

(a) (b)

Figure 6.41: TMO oscillation due to Tin ocillation with 3x3 FA model (CASMO XS, U-MOX-FA, BU: 10-30 MWd/kgHM).

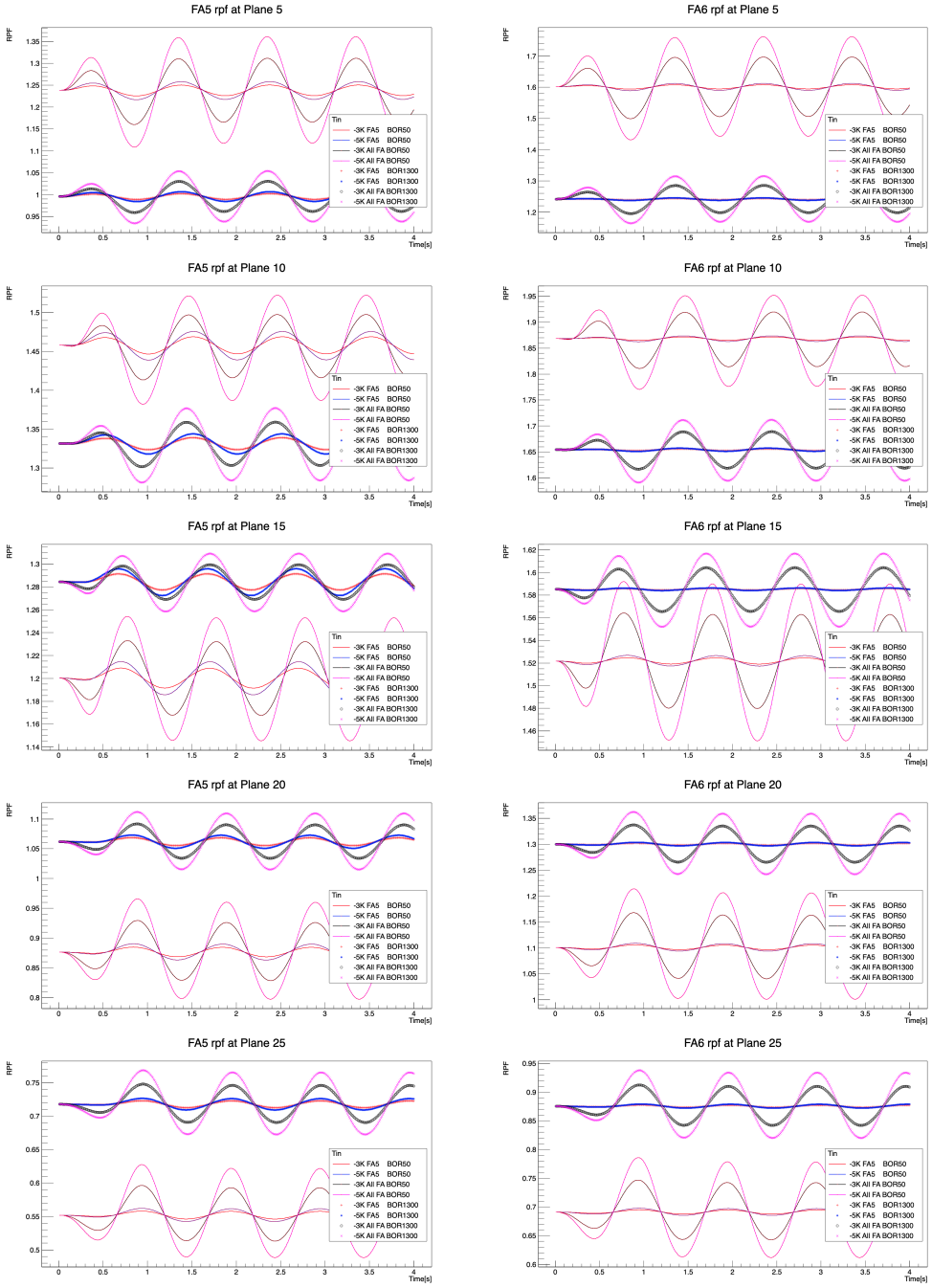

(a) (b)

Figure 6.42: RPF oscillation due to Tin oscillation with 3x3 FA model (CASMO XS, U-MOX-FA, BU: 10-30 MWd/kgHM).

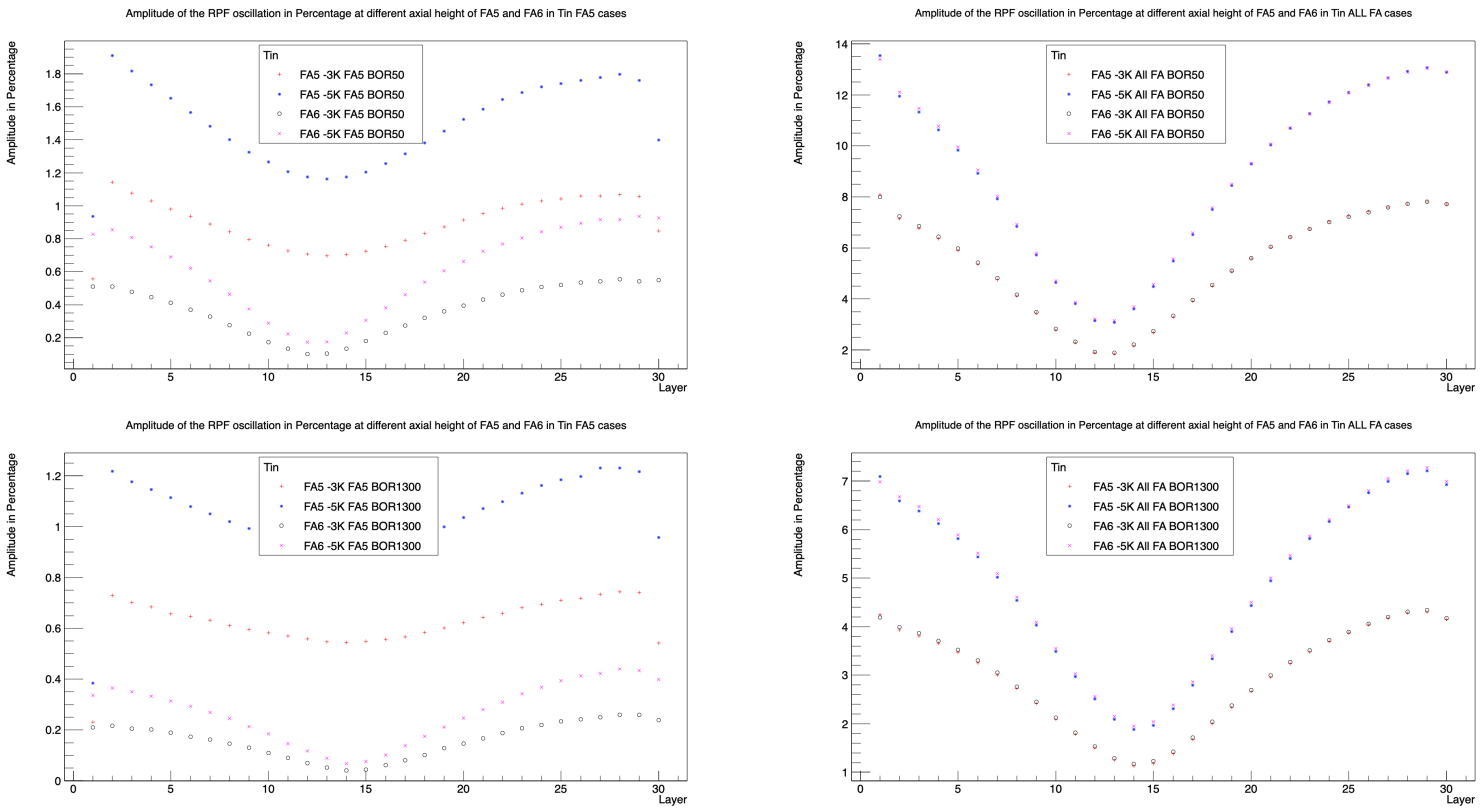

Figure 6.43: Percentage-wise amplitude of RPF oscillation with respect to its reference value at different axial height of FA5 and FA6 in Tin (left: FA5, right: ALL FA) cases (CASMO XS, U-MOX-FA, BU: 10-30 MWd/kgHM).

6.2.3.2.2.2 Vin cases

In Fig. 6.44 the TMO is shown for FA5 and FA6 with respect to different axial planes. The oscillation behavior is quite similar to what we have observed in U-MOX-FA 0-10 MWd/kgHM cases (s. sec. 6.2.3.1.2.2).

The neutronics response (RPF) is shown in Fig. 6.45. The oscillation behavior is quite similar to the U-MOX-FA 0-10 MWd/kgHM (s. sec. 6.2.3.1.2.2) featuring a higher oscillation amplitude in the 50ppm cases. The reason has already been explained in sec. 6.2.2.1.2.2.

In Fig. 6.46 the RPF oscillation amplitude of each plane is normalized to its initial value. The distributions of the oscillation amplitude shown in these cases are also similar to the previous U/MOX-FA 0-10MWd/kgHM cases (s. sec. 6.2.3.1.2.2).

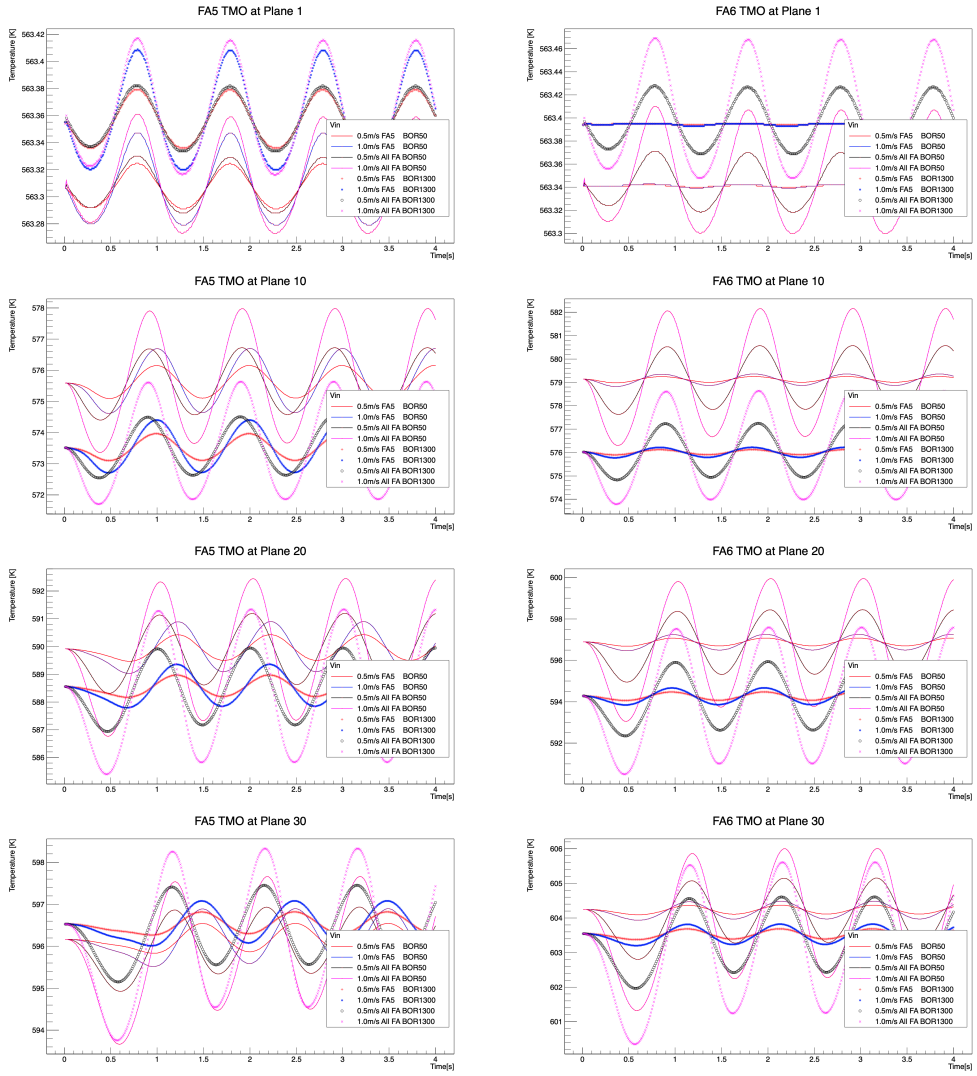

(a) (b)

Figure 6.44: TMO oscillation due to Vin ocillation with 3x3 FA model (CASMO XS, U-MOX-FA, BU: 10-30 MWd/kgHM).

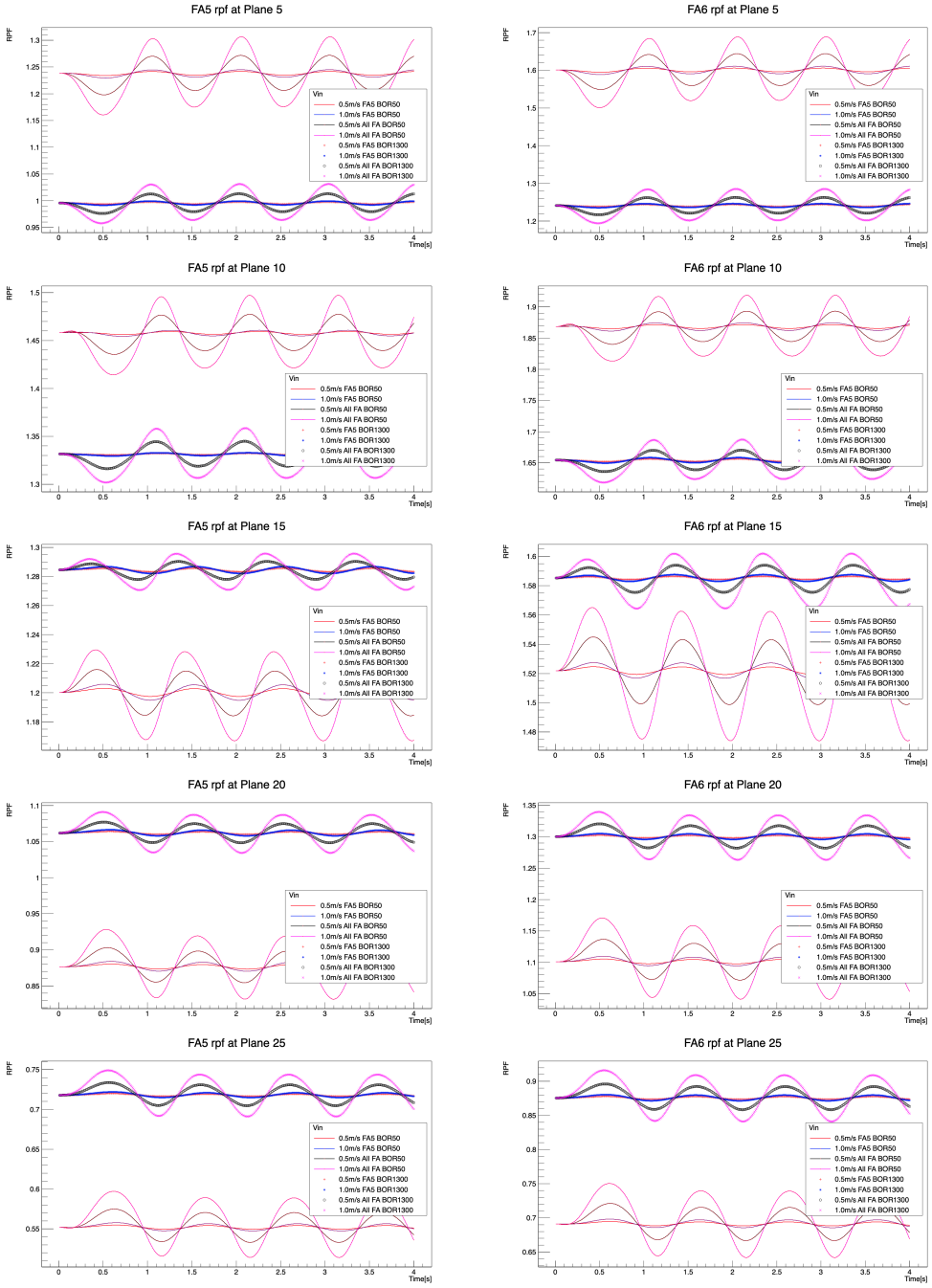

(a) (b)

Figure 6.45: RPF oscillation due to Vin oscillation with 3x3 FA model (CASMO XS, U-MOX-FA, BU: 10-30 MWd/kgHM).

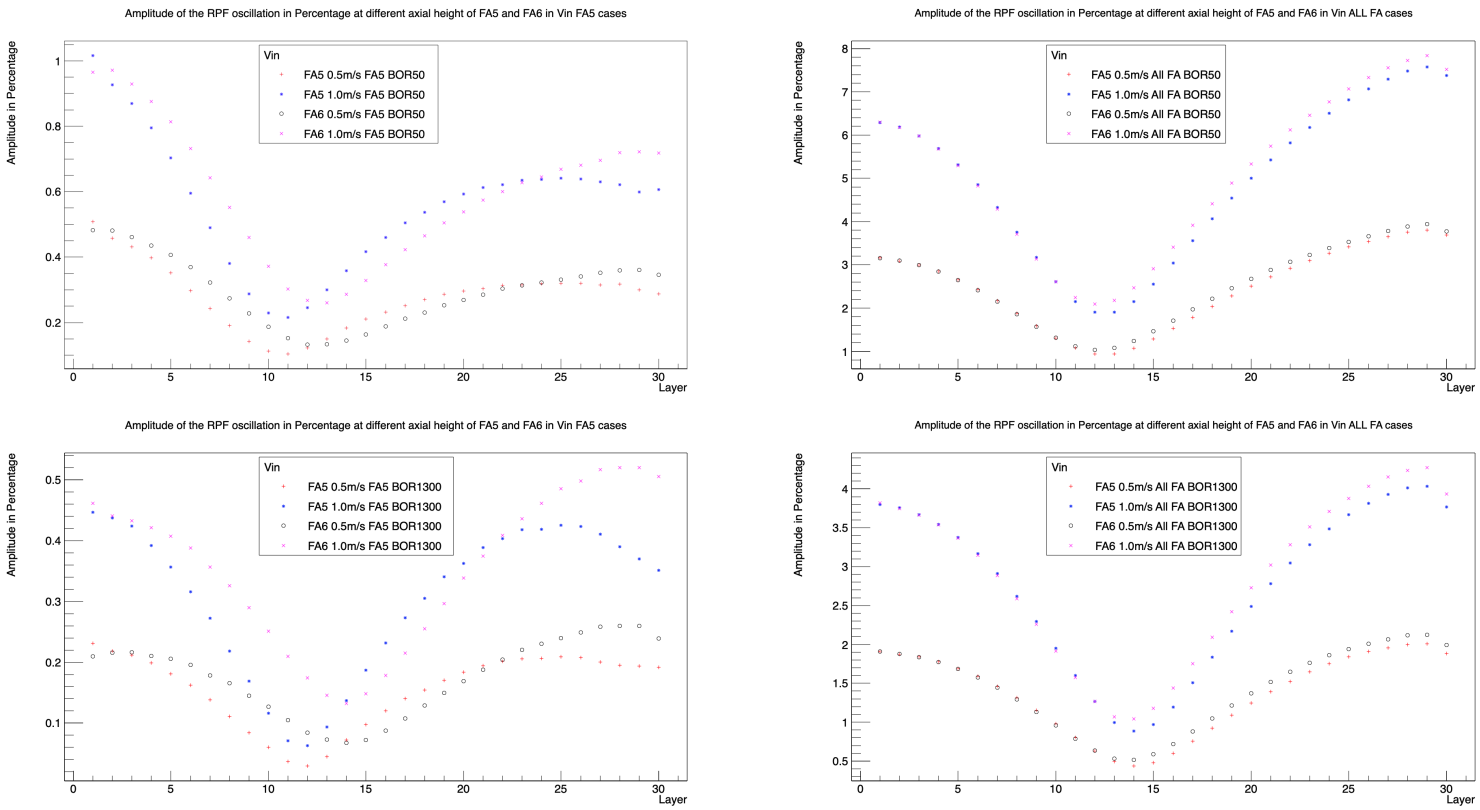

Figure 6.46: Percentage-wise amplitude of RPF oscillation with respect to its reference value at different axial height of FA5 and FA6 in Vin (left: FA5, right: ALL FA) cases (CASMO XS, U-MOX-FA, BU: 10-30 MWd/kgHM).

6.2.4 Additional Cases

In the previous sections, the oscillating boundary conditions were applied either on the central fuel assembly or on all fuel assemblies which reflected more or less a symmetric distribution of the boundary condition. On the other hand, based on the example of the APSD diagram (see Fig. 1.3) it was decided to set the frequency of the oscillation to be 1 Hz. In sec. 5 cases applying 1Hz and 5Hz of oscillation have been investigated giving a general comparison of the axial power distribution. In the first part of this section, the oscillating boundary condition is applied on the two opposite corner fuel assemblies (FA1 and FA9) simulating an asymmetric temperature change. In the second part, a wider range of the oscillation frequencies (or periods) is investigated. In both part, the same fuel composition as in section 6.2.2.1.1 (CASMO XS libraries, U-FA, burnup 0-10 MWd/kgHM, boron concentration 50ppm) is used.

6.2.4.1 Case 1

The general idea of this investigation is to apply an opposite temperature oscillation on the opposite corner fuel assemblies with each corner fuel assembly trying to represent one quadrant of the reactor. In Fig. 6.47 the location and the magnitude of the temperature oscillation are depicted. The equation used to calculate the oscillation can be found in Eq. 6.1.

In Fig. 6.48 the coolant temperature and the axial power fraction are shown for different axial planes in different fuel assemblies. Noticeably, the neutronic oscillation mainly locates in the corner FAs (FA1 and FA9) whereas it is barely seen in the other fuel assemblies. In this case, the neutronic behavior in the upper par and the lower part of the fuel assembly doesn't have a 180° of phase change.

Fig. 6.49 depicts the percentage oscillation magnitude of the relative power fraction with respect to its initial value. In this case, the percentage-wise oscillation in the corner fuel assemblies (FA1 and FA9) has a relatively uniform

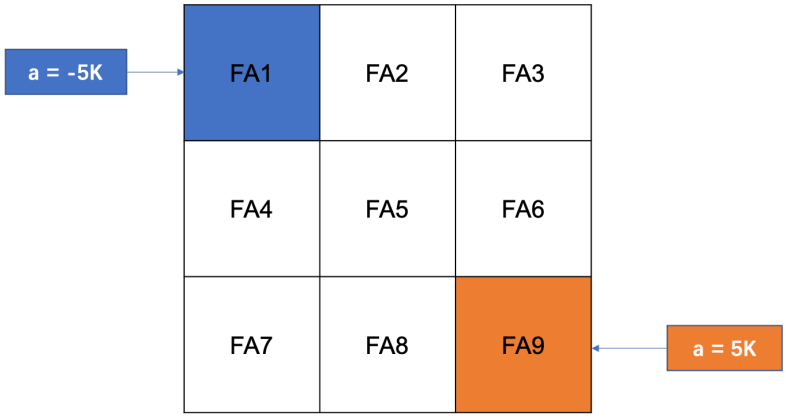

Figure 6.47: Illustration of the asymmetric distribution of the disturbances.

distribution at around 1.5% while it can be barely seen in FA5 and FA3.

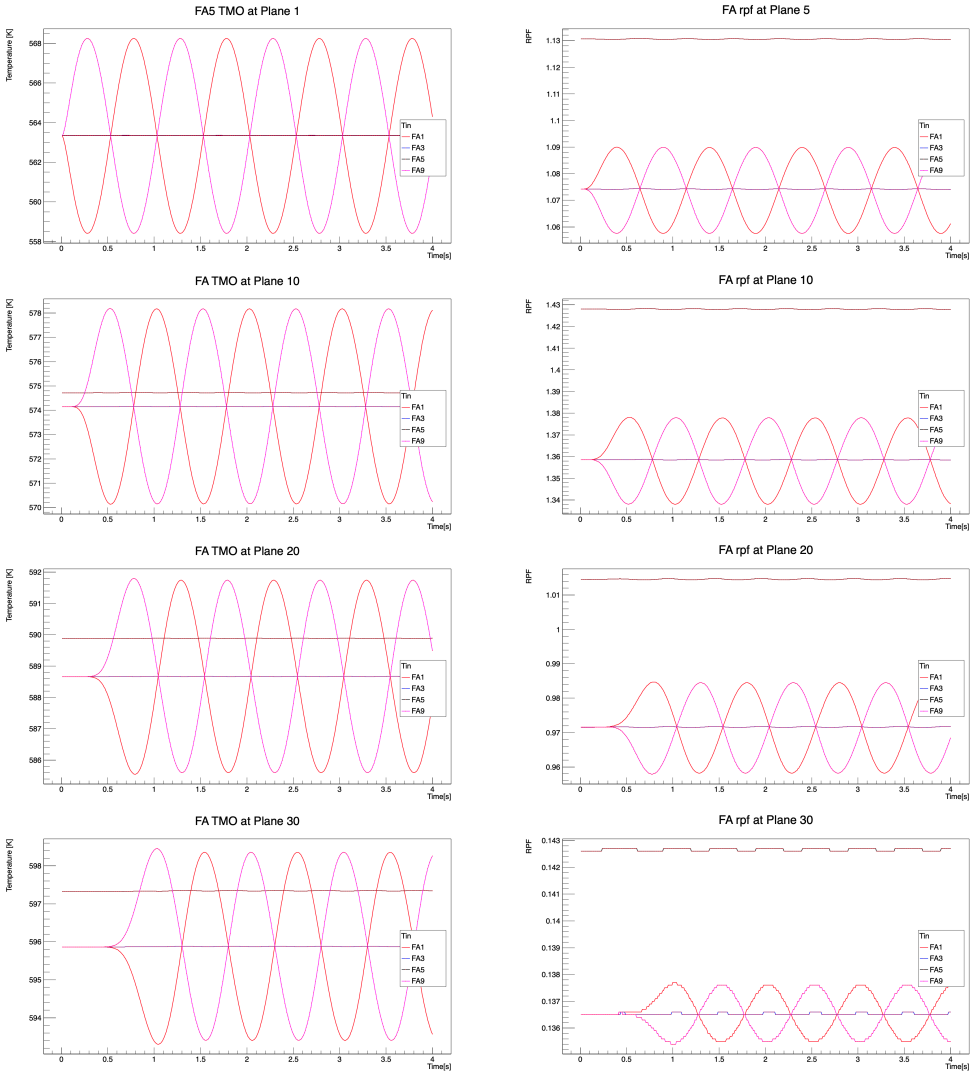

(a) (b)

Figure 6.48: TMO and neutronic behavior at different axial planes due to Tin oscillation (asymmetric inlet boundary condition).

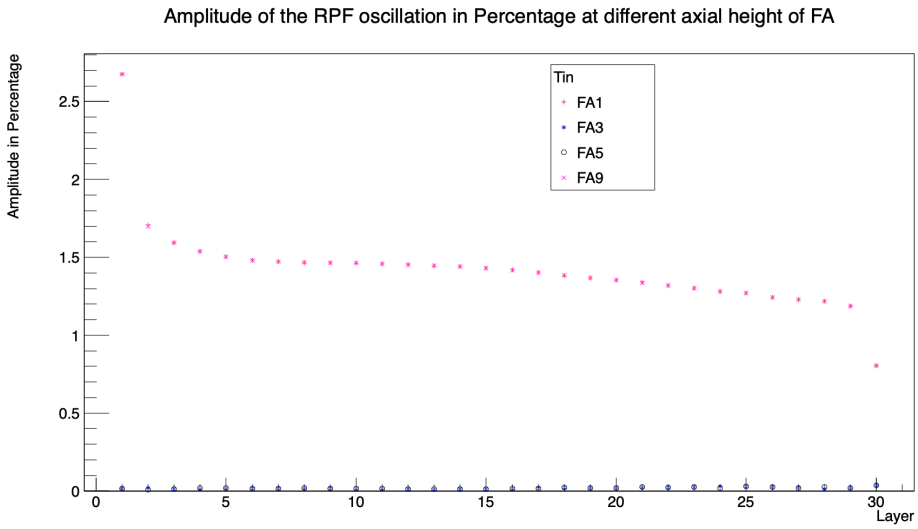

Figure 6.49: Percentage-wise amplitude of RPF oscillation with respect to its reference value at different axial planes (asymmetric inlet boundary condition).

6.2.4.2 Case 2

In this section, different inlet oscillation frequencies (or periods) will be applied as the boundary condition to furtherly illustrate the impact of the oscillation frequency on neutronic field. The reference case is the CASMO case, U-FA with a burnup composition of 0-10 MWd/kgHM, boron concentration of 50ppm, inlet temperature oscillation of -5K on all FA (see sec. 6.2.2.1.2.1). A list of the boundary conditions in other cases is shown in Tab. 6.3. Noted that the frequency f boundary condition is converted to period T. The equation 6.1 can be rewritten as:

$$\delta = a \cdot sin(\frac{t}{T} \cdot 2\pi) \tag{6.2}$$

	Reference	New cases
Period (T) [s]	1	0.4, 0.6, 0.7, 0.8, 1.2, 1.5, 2.1

Table 6.3: Cases of the investigations on oscillation frequency (or period T).

In the following figure 6.50 the coolant temperature of FA5 and FA6 on different axial planes are shown. It can be seen that with a higher period (or a lower frequency) the coolant temperature oscillation shows a more consistent behavior as the inlet temperature oscillation with respect to the amplitude (5K). On the other hand, when taking a look at the axial relative power fraction (in Fig. 6.51), the same tendency of the RPF oscillation with the period increment can not be concluded. For example, on plane 10 the oscillation amplitude increases with a period from 0.4s to 1.0s and then decreases from 1.2s to 2.1s whereas on plane 15 the oscillation amplitude increases with a period from 0.4s to 0.7s and then decreases from 0.8s to 2.1s. In Fig. 6.52 the information of the neutronic oscillation amplitude is put into two more informative graphs. In the upper graph the percentage-wise RPF oscillation amplitude is plotted for each axial plane of FA5 and in the lower graph this information is plotted with colored bins. In this series of investigation it can

be concluded that when the inlet oscillation period is higher (or frequency is lower), the neutronic oscillation is more suppressed in the middle height. The maximum oscillation amplitude is around 11% at the top and bottom node when the inlet oscillation period is around 1.2s.

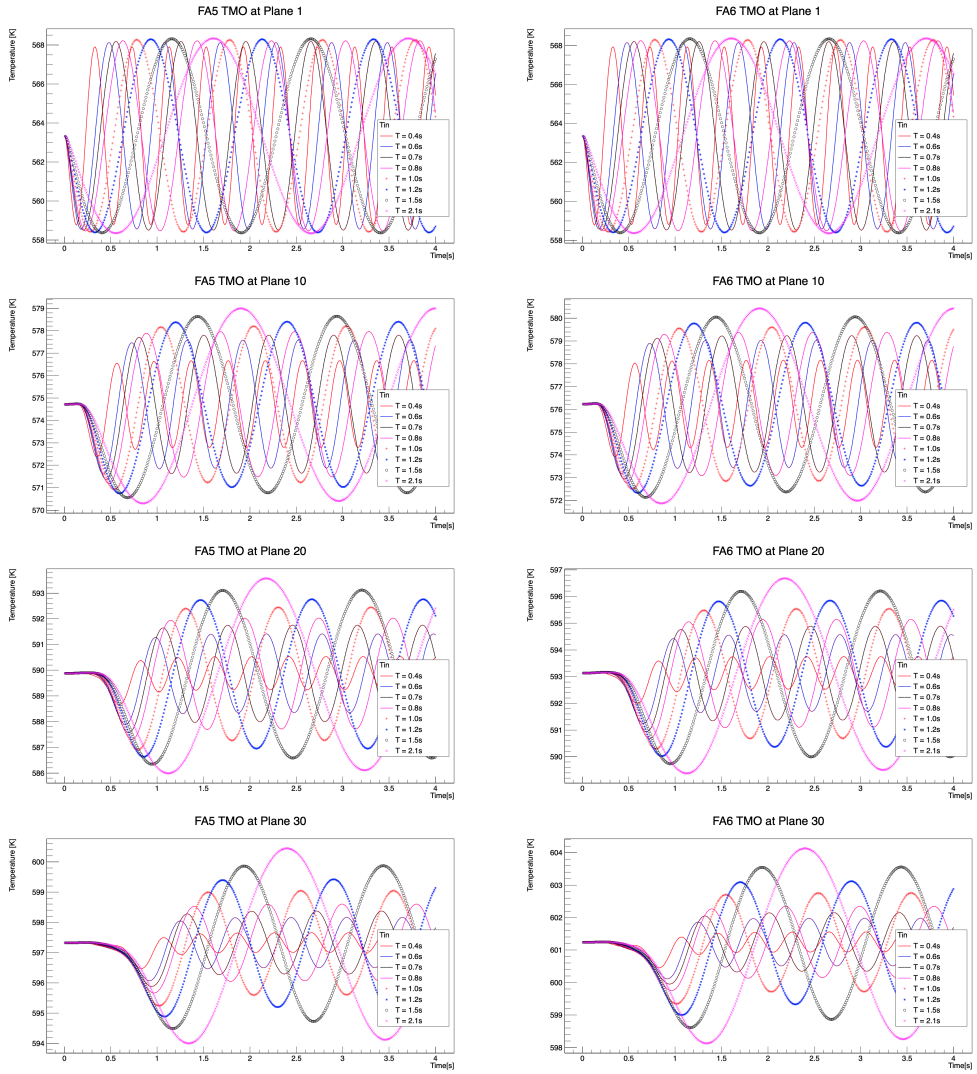

(a) (b)

Figure 6.50: TMO oscillation due to Tin oscillation with 3x3 FA model.

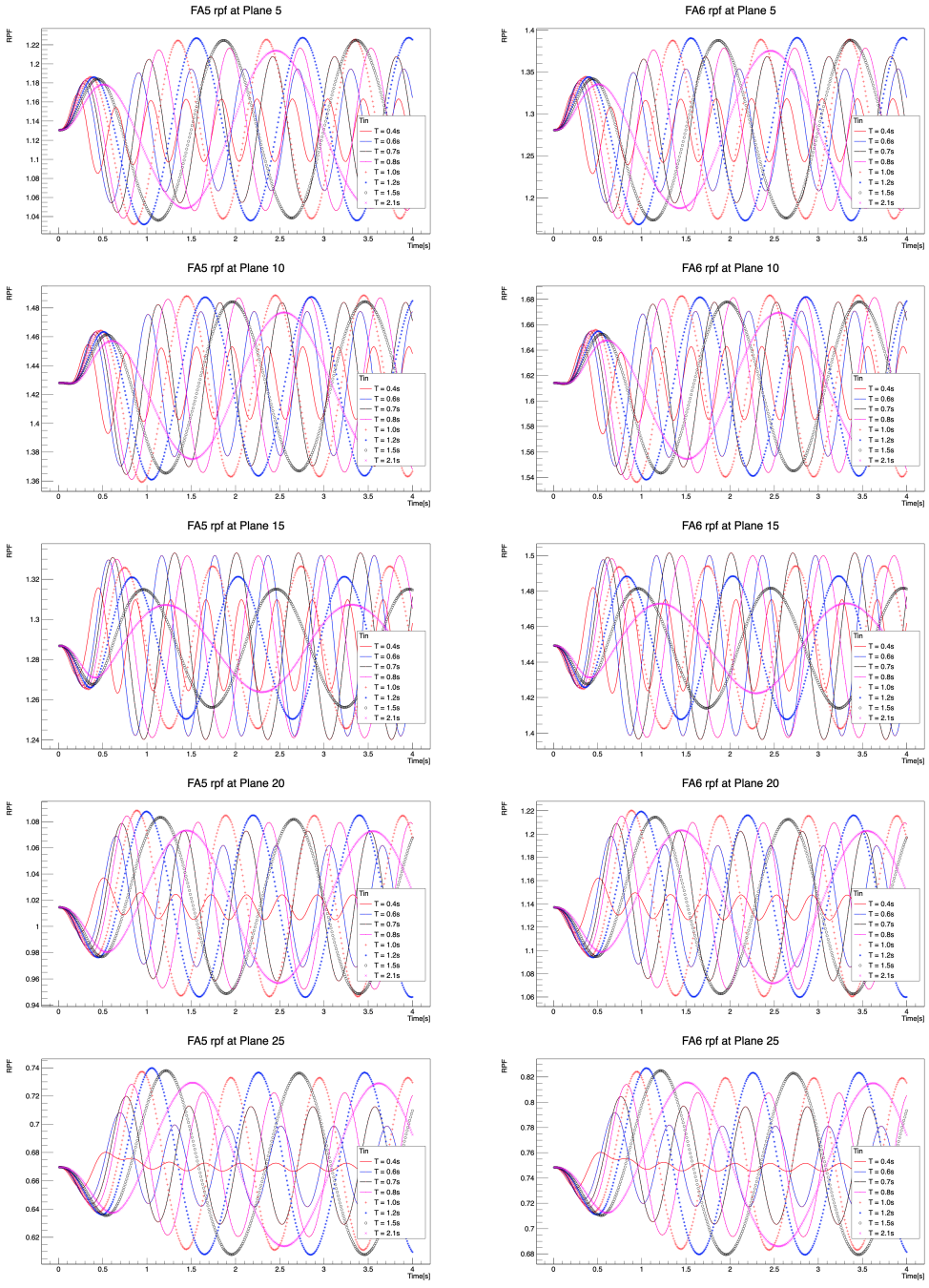

(a) (b)

Figure 6.51: RPF oscillation due to Tin oscillation with 3x3 FA model.

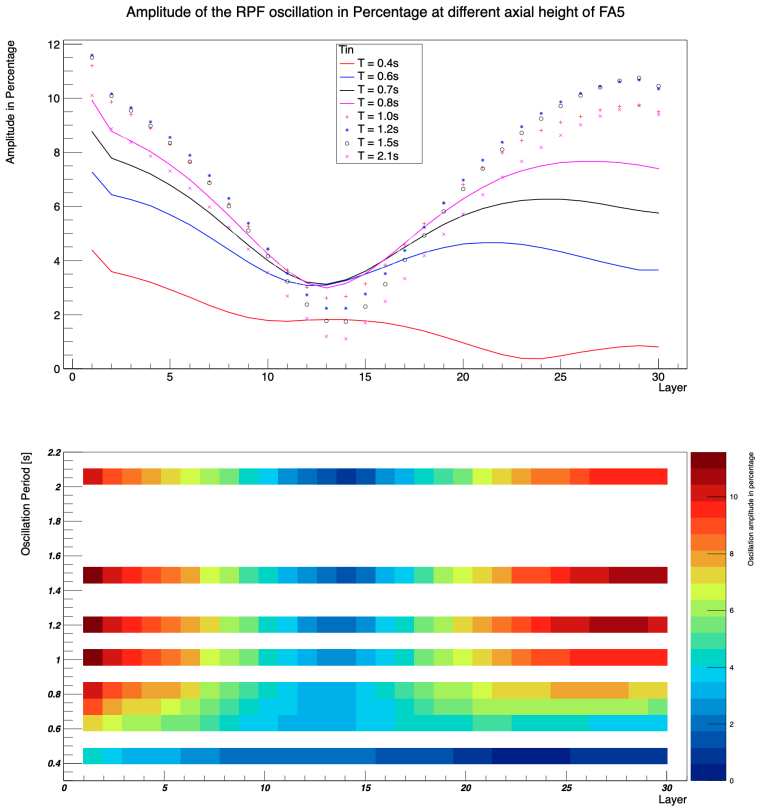

Figure 6.52: Percentage-wise amplitude of RPF oscillation with respect to its reference value at different axial height of FA5.

6.3 Summary

In this chapter, the coupled model was tested with the 3x3 fuel assembly model. The tested transients were focused on investigating the thermodydraulic & neutronic behavior with different core configurations while changing the inlet boundary condition.

Cases simulated with the SERPENT cross sections illustrate a basis simulation of the 3x3 fuel assembly model behavior under the transient cases: the neutronic behavior in the upper part and lower part of the fuel assembly has a phase shift of almost 180°, the amplitude of the neutronic oscillation has the maximum at the top and bottom and the minimum at the middle of the fuel assembly. Utilizing the pin power distribution under a fuel assembly bow case from the SERPENT calculation, this model also tested the system behavior due to oscillating fuel rods. Under the 3x3 fuel assembly model, the maximum rod displacement was restricted under 1.5mm avoiding fuel rod touch between two neighboring fuel assemblies. No obvious neutronic oscillation induced by oscillation fuel rods can be observed.

Cases simulated with the CASMO cross sections investigate the 3x3 fuel assembly model behavior implementing different burnups which can have influences on the moderator temperature coefficient and fuel temperature coefficient. In general, the neutronic behavior is quite similar to the SERPENT cases. The difference is that in the CASMO cases the boron concentration is set to be 50ppm or 1300ppm while in the SERPENT cases 500ppm or 2200ppm. By comparing these two test sets it is also shown that the neutronic field is more sensitive to the TH parameter oscillation with a relative low boron concentration (50ppm, close to the EOC condition) than with a higher boron concentration (1300ppm, close to BOC condition). This is also in accordance with the observation shown in Fig. 1.6.

In the last part of the investigation, a phase difference of 180° can be observed in the neutronic signal in the two opposite corner fuel assemblies if

an opposite oscillating boundary condition is applied on both fuel assembly inlets. Besides, the investigation of the oscillation period shows that the axial coolant temperature distribution as well as the neutronic oscillation amplitude distribution can be influenced by inserting different oscillation period.

Chapter 7

Conclusion and outlook

In this work, a thermohydraulic-neutronics coupled model has been established for a 3x3 fuel assembly matrix to conduct multi-physics simulations. The commercial software ANSYS CFX was chosen for the thermohydraulic simulation and the master process due to its high fidelity, solver robustness and the in-code embedded user define routine function. On the other side, a highly discretized multilayer neutronics model was built for the 3x3 fuel assembly model using NRC developed solver PARCS. For the generation of group constants and the pin power fraction calculation the Monte Carlo code SERPENT was used.

The TH model was developed and validated with a best-estimate subchannel model using TRACE. Due to the limitation of the accessible computation power, the TH model was simplified to some extent. But the results have shown that the difference can be maintained in an acceptable range thanks to the integrated wall function in CFX. The coupling model was developed based on the UDF module in CFX so that the data transfer between different models could be performed in each calculation step, which accelerated the convergence. Three additional modules have been developed to obtain essential data for the coupling and to offer different modes for the simulation. Two group constant sets were generated with SERPENT for U-FA and

Gd-FA. These group constants were implemented in PARCS and the results showed good agreement with the simulation with CASMO cross-section library. Furthermore, pin power fraction calculations were performed in order to investigate the FA bow cases in which local power change could play a role. Furthermore, some CASMO generated cross section libraries were converted for simulations with different burnup compositions.

Both in the single FA simulations and in the 3x3 FA simulations one can see that the Tin and Vin oscillations mostly influence the neutronic field of the top and bottom of the fuel assembly and a clear almost 180°phase difference can be seen in the neutronic signals between the top and bottom half of the fuel assembly. The observed neutron oscillation shows a regional increase or decrease in power rather than at a specific FA. It is seen that in the 3x3 FA simulations, even when the oscillation is locally applied (the FA5 cases), the neutronic feedback shows a global effect which means the trend of the neutron signal is the same for all FAs at the same height. The size of the 3x3 FA model may still be too small to observe any regional increase or decrease in power. Another effect which needs to be considered in the future modeling and simulation is the transversal flow between different FAs. From this model it can be seen the cross-flow is induced by the pressure difference of the neighboring FAs which happens mostly at the bottom of the FA and smooths out the effect of local mass flow rate oscillations. But yet still a question remains, the mass flow rate inside a reactor is quadrant related to one of the four pumps in the Vor-Konvoi and Konvoi design. The rehomogenization of the mass flow rate must be considered and simulated in a bigger scope which leads to full core simulations. It is also seen that the boron concentration plays an important role here. The results have shown that the neutronic oscillation is constantly higher in the low boron concentration cases (50ppm) than in the high boron concentration cases (1300ppm) which is in accordance with the observation in the nuclear power plant (the comparison between EOC and BOC).

On the other hand, the FA bow simulation doesn't show a noticeable moderator or neutron oscillation due to the flow area change or redirection of the flow direction. Due to the size of the model, the fuel assembly can bow up to about 3.5mm otherwise the fuel rods between different FAs can get contacted. From the pin by pin calculation it is seen that the pin power fraction change is mainly located on the peripheral row which means the neutron flux inside the detector channel (the guide tube) is less influenced. A possible cause for a noticeable power change could be due to the temperature change induced by cross-flow between two FAs with large temperature gradient and this FA bow induced cross-flow demands a relative large magnitude of displacement. Besides, the conventional diffusion solver is designed for the normal fuel assembly without any displacement. For cases in which part of the fuel assembly enters another fuel assembly's location, new simulation method and experiment data are needed. And the model established by this work can be deployed for validation.

Apart from all the above mentioned restrictions of the 3x3 FA model, one of the phenomena which can be observed in this model is the 180°phase difference of the neutronic signals in the two opposite located corner fuel assemblies when inserting opposite boundary conditions on them. Yet the model only represents a 3x3 FA matrix model. To verify this phenomena a full core simulation is needed.

In the future, the CFD-neutronic coupled model can still play an important role for estimating possible effects which can cause neutron oscillation. One can add the FSI into the coupling model. But the structure vibration induced TMO change needs to be examined at a bigger scale, a full scale core simulation for example. Given the current computation capability, a full scale core simulation is hardly achievable at the level of fuel rods. On the other hand, one can use porous medium to build a reactor core to conduct Tin and Vin simulations. The advantage of using porous medium is that the mesh can be much coarser than the model in this work and the calculation speed is

much faster. The fuel temperature cannot be calculated backwards from the cladding temperature but from a correlation with TMO and power density. Besides, the CFD & 3D neutronics coupled model can also be used for code validation offering high fidelity and robust results.

Appendix A

Material compostion for the reference state point

Nuclide	Number density [10^{24} cm^{-3}]
U-235	9.10243E-04
U-234	8.59221E-06
U-238	2.18459E-02
O-16	4.5524E-02

Table A.1: Fuel pellet (U-rod) at 873.15K

Nuclide	Number density [10^{24} cm^{-3}]
U-235	4.7417E-04
Gd-154	4.40236E-05
Gd-155	2.98876E-04
Gd-156	4.13377E-04
Gd-157	3.16041E-04
Gd-158	5.01629E-04
Gd-152	4.03890E-06
Gd-160	4.41449E-04
U-234	4.34435E-06
U-238	1.75346E-02
O-16	3.90560E-02

Table A.2: Fuel pellet (Gd-rod) at 873.15K

Nuclide	Number density [10^{24} cm^{-3}]
H-1	4.71482E-02
O-16	2.35765E-02
B-10	3.88173E-06
B-11	1.57545E-05

Table A.3: Moderator (fluid inside the guide tube) at 583.15K with BOR 500ppm

Nuclide	Number density [10^{24} cm^{-3}]
H-1	4.65115E-02
O-16	2.32622E-02
B-10	3.82931E-06
B-11	1.55417E-05
Natural Sn	6.47695E-06
Natural Fe	1.99401E-06
Natural Cr	1.01981E-06
Nb-93	5.70768E-06
Zr-90	2.90439E-04
Zr-91	6.33377E-05
Zr-92	9.68129E-05
Zr-94	9.81112E-05
Zr-96	1.58062E-05
Co-59	8.99767E-09
Ni-58	9.15259E-09
Ni-62	8.56255E-09
Fe-54	9.83069E-09

Table A.4: Moderator (fluid outside the guide tube) at 583.15K with BOR 500ppm

Nuclide	Number density [10^{24} cm^{-3}]
Natural Sn	4.78906E-04
Natural Fe	9.47811E-05
Natural Cr	7.54052E-05
Natural Ni	3.67402E-05
Zr-90	2.17006E-02
Zr-91	4.73238E-03
Zr-92	7.23354E-03
Zr-94	7.33055E-03
Zr-96	1.18099E-03
O-16	3.06399E-04

Table A.5: Cladding material (fuel rod) at 617.95K

Nuclide	Number density [10^{24} cm^{-3}]
Natural Sn	4.79215E-04
Natural Fe	9.48424E-05
Natural Cr	7.54539E-05
Natural Ni	3.67640E-05
Zr-90	2.17146E-02
Zr-91	4.73544E-03
Zr-92	7.23821E-03
Zr-94	7.33528E-03
Zr-96	1.18175E-03
O-16	3.06597E-04

Table A.6: Cladding material (guide tube) at 617.95K

Bibliography

[ANS19] ANSYS. *CFX-Solver modeling guide*. ANSYS, 2019.

[AP18] A. Abed and N. Poursalehi. Neutron noise simulation in the nuclear reactor core based on the average current nodal expansion method. *Annals of Nuclear Energy*, 114:482–494, apr 2018.

[Ber16] Berkcan Kapusuzoglu. Modeling of turbulent two-phase stratifed flow, 2016.

[BFF14] Ulrich Bieder, François Falk, and Gauthier Fauchet. LES analysis of the flow in a simplified PWR assembly with mixing grid. *Progress in Nuclear Energy*, 75:15–24, aug 2014.

[BHD+13] S. Bogetic, M. Hursin, A. Dokhane, H. Ferroukhi, S. Canepa, and A. Pautz. Comparison of U.S. NRC PARCS against Studsvik SIMULATE-3 core simulator for modeling and analysis of swiss PWRs. In *American Nulcear Society 2013 Student Conference - Massachusetts Institute of Technology, Boston, massachusetts, USA, April 4-6*, 2013.

[BHK16] Christoph Bläsius, Joachim Herb, and Matthias Küntzel. Untersuchung der Ursachen für Neutronenfluss-Schwankungen. Technical report, GRS, 2016.

[BITB00] T. Beam, Kostadin N. Ivanov, B. Taylor, and A. Baretta.

Pressurised water reactor main steam line break (MSLB) benchmark volume II: Summary results of phase i (point kinetics). Technical report, US Nuclear Regulatory Commision, OECD Nuclear Energy Agency, 2000.

[BKK77] K. Behringer, G. Kosály, and Lj. Kostić. Theoretical investigation of the local and global components of the neutron-noise field in a boiling water reactor. *Nuclear Science and Engineering*, 63(3):306–318, jul 1977.

[BMO17] J.A. Bermejo, C. Montalvo, and A. Ortego. On the possible effects contributing to neutron noise variations in KWU-PWR reactor: Modelling with s3k. *Progress in Nuclear Energy*, 95:1–7, mar 2017.

[CDB+17] D. Chionis, A. Dokhane, L. Belblidia, M. Pecchia, G. Girardin, H. Ferroukhi, and A. Pautz. SIMULATE-3K analyses of neutron noise response to fuel assembly vibrations and thermal-hydraulics parameters fluctuations. In *M&C 2017 - International Conference on Mathematics & Computational Methods Applied to Nuclear Science & Engineering, Jeju, Korea, April 16-20*, Jeju, Korea, April 16-20, 2017.

[DK90] B. Damiano and R. C. Kryter. Current applications of vibration monitoring and neutron noise analysis. Technical report, Oak Ridge National Laboratory, 1990.

[DPA+03] C. Demazière, I. Pázsit, T. Andersson, B. Severinsson, and T. Ranman. Analysis of an MTC noise measurement performed in ringhals-2 using gamma-thermometers and in-core neutron detectors. *Progress in Nuclear Energy*, 43(1-4):57–66, 2003.

[DSMJ17] Zhuoqi Du, Marcus Seidl, and Rafael Macián-Juan. Devel-

opment of a multiphysics approach with ANSYS CFX and PARCS for local analysis of neutron oscillation. jul 2017.

[DSMJ19] Zhuoqi Du, Marcus Seidl, and Rafael Macian-Juan. IMPLEMENTATION OF PIN POWER FACTORS IN THE ANSYS CFX/PARCS COULPLING SYSTEM FOR LOCAL ANALYSIS OF NEUTRON OSCILLATION. *The Proceedings of the International Conference on Nuclear Engineering (ICONE)*, 2019.27(0):1800, 2019.

[DSSMJ19] Zhuoqi Du, Dong-Yuan Sheng, Marcus Seidl, and Rafael Macian-Juan. Investigations of neutron noise induced by transient cross flow in a PWR reactor core. *The Proceedings of the 18th International Topical Meeting on Nuclear Reactor Thermal Hydraulics (NURETH)*, 2019.

[DXS12] T. Downar, Y. Xu, and V. Seker. *PARCS v.3.0 U.S. NRC core neutronics simulator theory manual*, 2012.

[DXS17] T. Downar, Y. Xu, and V. Seker. *PARCS v3.2 U.S. NRC Core Neutronics Simulator USER MANUAL*. School of Nuclear Engineering, Purdue University, W. Lafayette, Indiana 47907, November 2017.

[EH15] Mohamed A. Elsawi and Amal S. Bin Hraiz. Benchmarking of the WIMS9/PARCS/TRACE code system for neutronic calculations of the westinghouse AP1000™ reactor. *Nuclear Engineering and Design*, 293:249–257, nov 2015.

[FL11] E. Fridman and J. Leppänen. On the use of the serpent monte carlo code for few-group cross section generation. *Annals of Nuclear Energy*, 38(6):1399–1405, jun 2011.

[FL12] Emil Fridman and Jaakko Leppänen. Revised methods for few-group cross sections generation in the serpent monte carlo

code. In *PHYSOR 2012 - Advances in Reactor Physics, Knoxville, Tennessee, USA, April 15-20*, 2012.

[GJP12] Davor Grgić, Radomir Ječmenica, and Dubravko Pevec. Lattice codes pin power prediction comparison. *Nuclear Engineering and Design*, 246:27–40, may 2012.

[GL15] K. J. Geelhood and W. G. Luscher. FRAPCON-4.0 : Integral assessment. Technical report, Pacific Northwest National Laboratory, 2015.

[GL16] K. J. Geelhood and W. G. Luscher. FRAPTRAN-2.0: Integral assessment. Technical report, Pacific Northwest National Laboratory, 2016.

[GLCP16] K. J. Geelhood, W. G. Luscher, J. M. Cuta, and I. A. Porter. FRAPTRAN-2.0: A computer code for the transient analysis of oxide fuel rods. Technical report, Pacific Northwest National Laboratory, 2016.

[GLRP15a] K. J. Geelhood, W. G. Luscher, P. A. Raynaud, and I. E. Porter. FRAPCON-4.0 : A computer code for the calculation of steady-state, thermal-mechanical behavior of oxide fuel rods for high burnup. Technical report, Pacific Northwest National Laboratory, 2015.

[GLRP15b] K.J. Geelhood, W.G. Luscher, P.A. Raynaud, and I.E. Porter. *FRAPCON-4.0: A Computer Code for the Calculation of Steady-state, Thermal-mechanical Behavior of Oxide Fuel Rods for High Burnup*, September 2015.

[Glü07] M. Glück. Sub-channel analysis with f-COBRA-TF–code validation and approaches to CHF prediction. *Nuclear Engineering and Design*, 237(6):655–667, mar 2007.

[GRS90] GRS. Deutsche Risikostudie Kernkraftwerke Phase B. Technical report, Verlag TÜV Rheinland, 1990.

[HBD+17] M. Hursin, S. Bogetic, A. Dohkane, S. Canepa, O. Zerkak, H. Ferroukhi, and A. Pautz. Development and validation of a TRACE/PARCS core model of Leibstadt Kernkraftwerk cycle 19. *Annals of Nuclear Energy*, 101:559–575, mar 2017.

[HDYJ16] Mathieu Hursin, Thomas J. Downar, Joo Il Yoon, and Han Gyu Joo. Assessment of assembly homogenized two-steps core dynamic calculations using direct whole core transport solutions. *Annals of Nuclear Energy*, 87:356–365, jan 2016.

[He16] Xun He. *Validation of the TRACE code for the system dynamic simulations of the molten salt reactor experiment and the preliminary study on the dual fluid molten salt reactor*. PhD thesis, Technical University of Munich, 2016.

[HRFP15] M. Hursin, L. Rossinelli, H. Ferroukhi, and A. Pautz. Bwr full core analysis with Serpent/SIMULATE-3 hybrid stochastic/determinstic code sequence. In *ANS MC2015 - Joint International Conference Mathematics and Computation (M&C), Nashville, TN, April 19-23*, 2015.

[HVFP13] M. Hursin, A. Vasiliev, H. Ferroukhi, and A. Pautz. Comparison of Serpent and CASMO-5M for pressurized water reactors models. In *International Conference on Mathematics and Computational Methods Applied to Nuclear Science & Engineering (M&C 2013), Sun Valley, Idaho, USA, May 5-9, 2013*, 2013.

[IBB+99] Kostadin N. Ivanov, Tara M. Beam, Anthony J. Baratta, Adi Irani, and Nick Trikouros. Pressurised water reactor main

steam line break (MSLB) benchmark volume I: Final specifications. Technical report, US Nuclear Regulatory Commision, OECD Nuclear Energy Agency, 1999.

[Iko13] Timo Ikonen. FINIX - Fuel behavior model and interface for multiphysics applications - Code documentation for version 0.13.9. Technical report, VTT, 2013.

[iYJA12] Joo il Yoon, Han Gyu Joo, and Seung Hoon Ahn. Implementation of advanced multigroup nodal and pin power reconstruction methods into PARCS 3.1. Technical report, U. S. Nuclear Regulatory Commission, 2012.

[KTA17] KTA. Reaktordruckbehälter-Einbauten. Technical report, KTA-3204, 2017.

[LAC+16] G. Lerchl, H. Austregesilo, S. Ceuca, H. Glaeser, W. Luther, and P. Schöffel. ATHLET 3.1A Validation. Technical report, GRS, 2016.

[LAF+14] Jaakko Leppänen, Manuele Aufiero, Emil Fridman, Reuven Rachamin, and Steven van der Marck. Calculation of effective point kinetics parameters in the serpent 2 monte carlo code. *Annals of Nuclear Energy*, 65:272–279, mar 2014.

[Lep09] Jaakko Leppänen. On the use of the continuous-energy monte carlo method for lattice physics applications. In *2009 International Nuclear Atlantic Conference - INAC 2009, Rio de Janeiro, RJ, Brazil, Sept. 27 - Oct. 2, 2009*, 2009.

[LGP15] W. G. Luscher, K. J. Geelhood, and I. E. Porter. Material property correlations: comparisons between FRAPCON-4.0, FRAPTRAN-2.0, and MATPRO. Technical report, Pacific northwest national laboratory, 2015.

[LKD15] Deokjung Lee, Tomasz Kozlowski, and Thomas J. Downar. Multi-group SP 3 approximation for simulation of a three-dimensional PWR rod ejection accident. *Annals of Nuclear Energy*, 77:94–100, mar 2015.

[Lou13] Henri Loukusa. Validation of the FINIX fuel behavior code version 0.13.9. Technical report, VTT, 2013.

[LR99] E. Laggiard and J. Runkel. Noise analysis estimation of the moderator temperature coefficient for a PWR fuel cycle. *Annals of Nuclear Energy*, 26(2):149–156, jan 1999.

[MCD+07] J. Mahaffy, B. Chung, F. Dubois, F. Ducros, E. Graffard, M. Heitsch, M. Henriksson, E. Komen, F. Moretti, T. Morii, P. Mühlbauer, U. Rohde, M. Scheuerer, B. L. Smith, C. Song, T. Watanable, and G. Zigh. Best practice guidelines for the use of CFD in nulcear reactor safety applications. techreport, OECD Nuclear Energy Agency(NEA), 2007.

[MCFS17] Roman Mukin, Ivor Clifford, Hakim Ferroukhi, and Marcus Seidl. Thermal hydraulic analysis of PWR assembly bowing using subchannel code COBRA-TF. In *17th International Topical Meeting on Nuclear Reactor Thermal Hydraulics (NURETH-17), September 2017, Xi'an, China*, 2017.

[MECS14] Jorge Pérez Mañes, Victor Hugo Sánchez Espinoza, Sergio Chiva, and Robert Stieglitz. A new coupled CFD/neutron kinetics system for high fidelity simulations of LWR core phenomena: Proof of concept. *Science and Technology of Nuclear Installations*, 2014:1–13, 2014.

[MMNM+11] J. C. Martinez-Murillo, M. Novo, R. Miró, T. Barrachina, and G. Verdù. Coupled RELAP/PARCS full plant model - assessment of a cooling transient in Trillo nuclear power plant. Technical report, U.S. Nuclear Regulatory Commission, 2011.

[MPC+11] C. Peña Monferrer, F. Pellacani, S. Chiva, T.Barrachina, R. Miró, and R. Macián-Juan. CFD-Neutronic coupled caluclation of a quarer of a simplified PWR fuel assembly including spacer pressure drop and turbulence enhancement. In *2011 International Nulcear Atlantic Conference - INAC 2011, Belo Horizonte, MG, Brazil, October 24-28*, 2011.

[PD10a] I. Pázsit and V. Dykin. Investigation of the space-dependent noise induced by propagating perturbations. *Annals of Nuclear Energy*, 37(10):1329–1340, oct 2010.

[PD10b] Imre Pázsit and Christophe Demazière. Noise techniques in nuclear systems. In *Handbook of Nuclear Engineering*, pages 1629–1737. Springer US, 2010.

[PMMHSC10] I. Pázsit, C. Montalvo-Martín, A. Hernandez-Solís, and P. Bernitt Cartemo. Diagnostics of the core barrel and fuel assembly vibrations in the swedish ringhals PWRs. In *NPIC&HMIT 2010,*, 2010.

[PT80] I. Pázsit and G. Th.Analytis. Theoretical investigation of the neutron noise diagnostics of two-dimensional control rod vibrations in a PWR. *Annals of Nuclear Energy*, 7(3):171–183, jan 1980.

[Rob67] J. C. Robinson. Analysis of neutron fluctuation spectra in the Oak Ridge research reactor and the high flux isotope reactor. Technical report, Oak Ridge National Laboratory, 1967.

[RSG+14] A. Rais, D. Siefman, G. Girardin, M. Hursin, and A. Pautz. Parcs few-group homogenized parameters generation using Serpent Monte Carlo code at the CROCUS reator. In *IGORR Conference*, 2014.

[RSG+15] A. Rais, D. Siefman, G. Girardin, M. Hursin, and A. Pautz. Methods and models for the coupled neutronics and thermal-hydraulics analysis of the CROCUS reactor at EFPL. *Science and Technology of Nuclear Installations*, 2015:1–9, 2015.

[RSH+17] Adolfo Rais, Daniel Siefman, Mathieu Hursin, Andrew Ward, and Andreas Pautz. Neutronics modeling of the CROCUS reactor with Serpent and PARCS codes. In *M&C 2017 - International Conference on Mathematics & Compuational Methods Applied to Nuclear Science & Engineering, Jeju, Korea, April 16-20*, 2017.

[RSK15] RSK. Verformungen von brennelementen in deutschen druckwasserreaktoren (DWR). Technical report, Reaktor-Sicherheitskommision (RSK), 2015.

[RSKB18] Ulrich Rohde, Marcus Seidl, Sören Kliem, and Yurii Bilodid. Neutron noise observations in german KWU built PWRs and analyses with the reactor dynamics code DYN3d. *Annals of Nuclear Energy*, 112:715–734, feb 2018.

[RSL06] Joel Rhodes, Kord Smith, and Deokjung Lee. CASMO-5 development and applications. In *PHYSOR-2006, ANS Topical Meeting on Reactor Physics, Vancouver, BC, Canada, September 10-14*, 2006.

[RSZ17] Amélie Rouchon, Richard Sanchez, and Igor Zmijarevic. The new 3-D multigroup diffusion neutron solver of APOLLO3 and a theoretical discussion of fission-modes noise. In *M&C 2017 - International Conference on Mathematics & Computational Methods Applied to Nuclear Science & Engineering, Jeju, Korea, April 16-20*, 2017.

[SA83] R.J.J. Stammler and M.J. Abbate. *Methods of Steady-State*

Reactor Physics in Nuclear Design. Academic Press INC. (London) LTD, 1983.

[San15] Richard Sanchez. Some comments in neutron noise theory. *Annals of Nuclear Energy*, 86:88–98, dec 2015.

[SBML10] M. Schikorr, E. Bubelis, L. Mansani, and K. Litfin. Proposal for pressure drop prediction for a fuel bundle with grid spacers using rehme pressure drop correlations. *Nuclear Engineering and Design*, 240(7):1830–1842, jul 2010.

[SC09] S. M. Salim and S. C. Cheah. Wall y^+ strategy for dealing with wall-bounded turbulent flows. In *Proceedings of the International MultiConference fo Engineers and Computer Scientists (IMECS 2009), March 18-20, 2009, Hong Kong*, March 2009.

[SGR+15] Daniel J. Siefman, Gaetan Girardin, Adolfo Rais, Andreas Pautz, and Mathieu Hursin. Full core modeling techniques for research reactors with irregular geometries using serpent and PARCS applied to the CROCUS reactor. *Annals of Nuclear Energy*, 85:434–443, nov 2015.

[SKS96] Michio Sadatomi, Akimaro Kawahara, and Yoshifusa Sato. Prediction of the single-phase turbulent mixing rate between two parallel subchannels using a subchannel geometry factor. *Nuclear Engineering and Design*, 162:245–256, 1996.

[SKSB15] Marcus Seidl, Kai Kosowski, Uwe Schüler, and Lotfi Belblidia. Review of the historic neutron noise behavior in german KWU built PWRs. *Progress in Nuclear Energy*, 85:668–675, nov 2015.

[SMLS85] F. J. Sweeney, J. March-Leuba, and C. M. Smith. Contribution of fuel vibrations to ex-core neutron noise during the

first and second fuel cycles of the Sequoyah-1 pressurized water reactor. *Progress in Nuclear Energy*, 15:289–290, 1985.

[SS15] Dong-Yuan Sheng and Marcus Seidl. Determination of the pressure loss coefficient at control-rod guide tube flow-hole for a PWR nuclear fuel assembly by using CFD and bernoulli solutions. In *NURETH-16, Chicago, IL, August 30-September 4, 2015*, 2015.

[SSD19] Dong-Yuan Sheng, Marcus Seidl, and Zhuoqi Du. CFD analysis of the fluid flow, heat transfer and cladding oxidation in a PWR fuel bundle. *The Proceedings of the 18th International Topical Meeting on Nuclear Reactor Thermal Hydraulics (NURETH)*, 2019.

[Stu11] Studsvik. *CASMO5 A fuel assembly burnup program User's Manual*. Studsvik, 2011.

[TCM+19] L.A. Torres, D. Chionis, Cristina Montalvo, A. Dokhane, and A. García-Berrocal. Neutron noise analysis of simulated mechanical and thermal-hydraulic perturbations in a PWR core. *Annals of Nuclear Energy*, 126:242–252, apr 2019.

[TEIJ11] Armando Gómez Torres, Victor Sánchez Espinoza, Uwe Imke, and Rafael Macián Juan. Pin level neutronic - thermalhydraulic two-way-coupling using DYN3D-SP3 and Subchanflow. In *M&C 2011 - International Conference on Mathematics & Compuational Methods Applied to Nuclear Science & Engineering, Rio de janeiro, RJ, Brazil, May 8-12, 2011*, 2011.

[THW91] J. R. Thomas, J. D. Herr, and D. S. Wood. Noise analysis method for monitoring the moderator temperature coefficient of pressurized water reactors: I. theory. *Nuclear Science and Engineering*, 108(4):331–340, aug 1991.

[TIT03] N. Todorova, K. Ivanov, and B. Taylor. Pressurised water reactor main steam line break (MSLB) benchmark volume iv: Results of phase III on coupled core-plant transient modelling. Technical report, US Nuclear Regulatory Commision, OECD Nuclear Energy Agency, 2003.

[TTI02] N. Todorova, B. Taylor, and K. Ivanov. Pressurised water reactor main steam line break (MSLB) benchmark volume iii: Results of phase 2 on 3-D core boundary conditions model. Technical report, US Nuclear Regulatory Commision, OECD Nuclear Energy Agency, 2002.

[WS48] A. M. Weinberg and H. C. Schweinler. Theory of oscillating absorber in a chain reactor. *Physical Review*, 74(8):851–863, oct 1948.

[WSMJ18] Andreas Wanninger, Marcus Seidl, and Rafael Macián-Juan. Mechanical analysis of the bow deformation of a row of fuel assemblies in a PWR core. *Nuclear Engineering and Technology*, 50(2):297–305, mar 2018.

[WZH+19] Xiang WANG, Qian ZHANG, Xun HE, Zhuoqi DU, Marcus SEIDL, Rafael MACIAN-JUAN, Konrad CZERSKI, and Mariusz DABROWSKI. NEUTRON PHYSICAL FEASIBILITY OF SMALL MODULAR DESIGN OF DUAL FLUID REACTOR. *The Proceedings of the International Conference on Nuclear Engineering (ICONE)*, 2019.27(0):1229, 2019.

[XDW+09] Yunlin Xu, Thomas Downar, R. Walls, K. Ivanov, J. Staudenmeier, and J. March-Lueba. Application of TRACE/PARCS to BWR stability analysis. *Annals of Nuclear Energy*, 36(3):317–323, apr 2009.

[YKY08] Akio YAMAMOTO, Yasunori KITAMURA, and Yoshihiro YAMANE. Simplified treatments of anisotropic scattering

in LWR core calculations. *Journal of Nuclear Science and Technology*, 45(3):217–229, mar 2008.